



# TOI 560: Two Transiting Planets Orbiting a K Dwarf Validated with iSHELL, PFS, and HIRES RVs

Mohammed El Mufti<sup>1,2</sup> , Peter P. Plavchan<sup>1</sup> , Howard Isaacson<sup>3,4</sup> , Bryson L. Cale<sup>5,6</sup> , Dax L. Feliz<sup>7</sup> , Michael A. Reefer<sup>1</sup> , Coel Hellier<sup>8</sup> , Keivan Stassun<sup>7</sup> , Jason Eastman<sup>9</sup> , Alex Polanski<sup>10</sup> , Ian J. M. Crossfield<sup>11</sup> , Eric Gaidos<sup>12</sup> , Veselin Kostov<sup>13</sup> , Justin M. Wittrock<sup>1</sup> , Joel Villaseñor<sup>14</sup> , Joshua E. Schlieder<sup>13</sup> , Luke G. Bouma<sup>15</sup> , Kevin I. Collins<sup>1</sup> , Farzaneh Zohrabi<sup>16</sup> , Rena A. Lee<sup>12</sup> , Ahmad Sohani<sup>17</sup> , John Berberian<sup>1</sup> , David Vermilion<sup>1,13</sup> , Patrick Newman<sup>1</sup> , Claire Geneser<sup>17</sup> , Angelle Tanner<sup>17</sup> , Natalie M. Batalha<sup>19</sup> , Courtney Dressing<sup>20</sup> , Benjamin Fulton<sup>21</sup> , Andrew W. Howard<sup>22</sup> , Daniel Huber<sup>23</sup> , Stephen R. Kane<sup>24</sup> , Erik A. Petigura<sup>25</sup> , Paul Robertson<sup>26</sup> , Arpita Roy<sup>27,28</sup> , Lauren M. Weiss<sup>29</sup> , Aida Behmard<sup>30,66</sup> , Corey Beard<sup>26</sup> , Ashley Chontos<sup>23,66</sup> , Fei Dai<sup>31</sup> , Paul A. Dalba<sup>24,32,67</sup> , Tara Fetherolf<sup>24,68</sup> , Steven Giacalone<sup>33</sup> , Michelle L. Hill<sup>24</sup> , Lea A. Hirsch<sup>34</sup> , Rae Holcomb<sup>26</sup> , Jack Lubin<sup>26</sup> , Andrew Mayo<sup>33</sup> , Teo Močnik<sup>35</sup> , Joseph M. Akana Murphy<sup>32,66</sup> , Lee J. Rosenthal<sup>22</sup> , Ryan A. Rubenzahl<sup>22,66</sup> , Nicholas Scarsdale<sup>19</sup> , Christopher Stockdale<sup>36</sup> , Karen Collins<sup>37</sup> , Ryan Cloutier<sup>37,69</sup> , Howard Relles<sup>37</sup> , Thiam-Guan Tan<sup>38,39</sup> , Nicholas J Scott<sup>40</sup> , Zach Hartman<sup>41</sup> , Elisabeth Matthews<sup>42</sup> , David R. Ciardi<sup>43</sup> , Erica Gonzales<sup>32</sup> , Rachel A. Matson<sup>44</sup> , Charles Beichman<sup>6,45</sup> , Allyson Bieryla<sup>37</sup> , E. Furlan<sup>46</sup> , Crystal L. Gnlika<sup>40</sup> , Steve B. Howell<sup>40</sup> , Carl Ziegler<sup>47</sup> , César Briceño<sup>48</sup> , Nicholas Law<sup>49</sup> , Andrew W. Mann<sup>49</sup> , Markus Rabus<sup>50</sup> , Marshall C. Johnson<sup>51</sup> , Jessie Christiansen<sup>52</sup> , Laura Kreidberg<sup>53</sup> , David Anthony Berardo<sup>54</sup> , Drake Deming<sup>55</sup> , Varoujan Gorjian<sup>56</sup> , Farisa Y. Morales<sup>6</sup> , Björn Benneke<sup>57</sup> , Diana Dragomir<sup>58</sup> , Robert A. Wittenmyer<sup>59</sup> , Sarah Ballard<sup>60</sup> , Brendan P. Bowler<sup>61</sup> , Jonathan Horner<sup>59</sup> , John Kielkopf<sup>62</sup> , Huigen Liu<sup>63</sup> , Avi Shporer<sup>14</sup> , C. G. Tinney<sup>64</sup> , Hui Zhang<sup>65</sup> , Duncan J. Wright<sup>59</sup> , Brett C. Addison<sup>59</sup> , Matthew W. Mengel<sup>59</sup> , and Jack Okumura<sup>59,70</sup> 

<sup>1</sup> Department of Physics and Astronomy, George Mason University, 4400 University Drive, Fairfax, VA 22030, USA; [mabdall@gmu.edu](mailto:mabdall@gmu.edu)

<sup>2</sup> University of Khartoum, Faculty of Science, Department of Physics, P.O.BOX 321, Khartoum 11111, Sudan

<sup>3</sup> Department of Astronomy, University of California Berkeley, Berkeley, CA 94720, USA

<sup>4</sup> Centre for Astrophysics, University of Southern Queensland, Toowoomba, QLD, Australia

<sup>5</sup> IPAC, 770 S Wilson Avenue, Pasadena, CA 91106, USA

<sup>6</sup> Jet Propulsion Laboratory, California Institute of Technology, 4800 Oak Grove Drive, Pasadena, CA 91109, USA

<sup>7</sup> Department of Physics and Astronomy, Vanderbilt University, 2201 West End Avenue, Nashville, TN 37235, USA

<sup>8</sup> Astrophysics Group, Keele University, Staffordshire, ST5 5BG, UK

<sup>9</sup> Center for Astrophysics, Harvard University, 60 Garden Street, Cambridge, MA 02138, USA

<sup>10</sup> Department of Physics & Astronomy, The University of Kansas, 1251 Wescoe Hall Drive, Lawrence, KS 66045, USA

<sup>11</sup> Department of Physics & Astronomy, University of Kansas, 1082 Malott, 1251 Wescoe Hall Drive, Lawrence, KS 66045, USA

<sup>12</sup> Department of Earth Sciences, University of Hawaii at Mānoa, Honolulu, HI 96822, USA

<sup>13</sup> NASA Goddard Space Flight Center, 8800 Greenbelt Road, Greenbelt, MD 20771, USA

<sup>14</sup> Department of Physics and Kavli Institute for Astrophysics and Space Research, Massachusetts Institute of Technology, Cambridge, MA 02139, USA

<sup>15</sup> Department of Astrophysical Sciences, Princeton University, 4 Ivy Lane, Princeton, NJ 08544, USA

<sup>16</sup> Department of Physics and Astronomy, Louisiana State University, 202 Nicholson Hall, Baton Rouge, LA 70803, USA

<sup>17</sup> Mississippi State University, Department of Physics and Astronomy, 355 Lee Boulevard, Mississippi State, MS 39762, USA

<sup>18</sup> Woodson High School, 9525 Main Street, Fairfax, VA 22031, USA

<sup>19</sup> Department of Astronomy and Astrophysics, University of California, Santa Cruz, CA 95060, USA

<sup>20</sup> 501 Campbell Hall, University of California at Berkeley, Berkeley, CA 94720, USA

<sup>21</sup> NASA Exoplanet Science Institute/Caltech-IPAC, MC 314-6, 1200 E. California Boulevard, Pasadena, CA 91125, USA

<sup>22</sup> Department of Astronomy, California Institute of Technology, Pasadena, CA 91125, USA

<sup>23</sup> Institute for Astronomy, University of Hawaii, 2680 Woodlawn Drive, Honolulu, HI 96822, USA

<sup>24</sup> Department of Earth and Planetary Sciences, University of California, Riverside, CA 92521, USA

<sup>25</sup> Department of Physics & Astronomy, University of California Los Angeles, Los Angeles, CA 90095, USA

<sup>26</sup> Department of Physics & Astronomy, University of California Irvine, Irvine, CA 92697, USA

<sup>27</sup> Space Telescope Science Institute, 3700 San Martin Drive, Baltimore, MD 21218, USA

<sup>28</sup> Department of Physics and Astronomy, Johns Hopkins University, 3400 N Charles Street, Baltimore, MD 21218, USA

<sup>29</sup> University of Notre Dame, Notre Dame, IN 46556 USA

<sup>30</sup> Division of Geological and Planetary Science, California Institute of Technology, Pasadena, CA 91125, USA

<sup>31</sup> California Institute of Technology, Division of Geological and Planetary Sciences, 1200 E California Boulevard, Pasadena, CA 91125, USA

<sup>32</sup> Department of Astronomy and Astrophysics, University of California, Santa Cruz, CA 95064, USA

<sup>33</sup> Department of Astronomy, University of California Berkeley, Berkeley, CA 94720, USA

<sup>34</sup> Kavli Institute for Particle Astrophysics and Cosmology, Stanford University, Stanford, CA 94305, USA

<sup>35</sup> Gemini Observatory/NSF's NOIRLab, 670 N. A'ohoku Place, Hilo, HI 96720, USA

<sup>36</sup> Hazelwood Observatory, Australia

<sup>37</sup> Center for Astrophysics | Harvard & Smithsonian, 60 Garden Street, Cambridge, MA 02138, USA

<sup>38</sup> Perth Exoplanet Survey Telescope, Perth, Western Australia, Australia

<sup>39</sup> Curtin Institute of Radio Astronomy, Curtin University, Bentley, Western Australia 6102, Australia

<sup>40</sup> NASA Ames Research Center, Moffett Field, CA 94035, USA

<sup>41</sup> Gemini observatory, Maunakea Access Road, Hilo, HI 96720, USA

<sup>42</sup> Observatoire de l'Université de Genève, Chemin Pegasi 51, 1290 Versoix, Switzerland

<sup>43</sup> Caltech/IPAC-NASA Exoplanet Science Institute, 770 S. Wilson Avenue, Pasadena, CA 91106, USA

<sup>44</sup> U.S. Naval Observatory, Washington, D.C. 20392, USA

<sup>45</sup> Caltech/IPAC-NASA Exoplanet Science Institute, 770 S. Wilson Avenue, Pasadena, CA 91106, USA

<sup>46</sup> NASA Exoplanet Science Institute, Caltech/IPAC, Mail Code 100-22, 1200 E. California Boulevard, Pasadena, CA 91125, USA

- <sup>47</sup> Department of Physics, Engineering and Astronomy, Stephen F. Austin State University, 1936 North Street, Nacogdoches, TX 75962, USA
- <sup>48</sup> Cerro Tololo Inter-American Observatory, Casilla 603, La Serena, Chile
- <sup>49</sup> Department of Physics and Astronomy, The University of North Carolina at Chapel Hill, Chapel Hill, NC 27599-3255, USA
- <sup>50</sup> Departamento de Matemática y Física Aplicadas, Facultad de Ingeniería, Universidad Católica de la Santísima Concepción, Alonso de Rivera 2850, Concepción, Chile
- <sup>51</sup> Department of Astronomy, The Ohio State University, 4055 McPherson Laboratory, 140 West 18<sup>th</sup> Avenue, Columbus, OH 43210 USA
- <sup>52</sup> Infrared Processing and Analysis Center, Caltech, Pasadena CA 91125, USA
- <sup>53</sup> Max-Planck-Institut für Astronomie, Königstuhl 17, D-69117 Heidelberg, Germany
- <sup>54</sup> MIT Kavli Institute for Astrophysics and Space Research, 77 Massachusetts Avenue, Cambridge, MA 02139, USA
- <sup>55</sup> Department of Astronomy, University of Maryland, College Park, MD 20742-2421 USA
- <sup>56</sup> Jet Propulsion Laboratory, California Institute of Technology, 4800 Oak Grove Drive, MS 306-392, Pasadena, CA 91109, USA
- <sup>57</sup> Department of Physics and Institute for Research on Exoplanets, Université de Montréal, Montreal, QC, Canada
- <sup>58</sup> Department of Physics and Astronomy, University of New Mexico, 210 Yale Boulevard NE, Albuquerque, NM 87106, USA
- <sup>59</sup> University of Southern Queensland, Centre for Astrophysics, West Street, Toowoomba, QLD 4350 Australia
- <sup>60</sup> Department of Astronomy, University of Florida, 211 Bryant Space Science Center, Gainesville, FL 32611, USA
- <sup>61</sup> Department of Astronomy, The University of Texas at Austin, Austin, TX 78712, USA
- <sup>62</sup> Department of Physics and Astronomy, University of Louisville, Louisville, KY 40292, USA
- <sup>63</sup> School of Astronomy and Space Science, Key Laboratory of Modern Astronomy and Astrophysics in Ministry of Education, Nanjing University, Nanjing 210046, Jiangsu, People's Republic of China
- <sup>64</sup> Exoplanetary Science at UNSW, School of Physics, UNSW Sydney, NSW 2052, Australia
- <sup>65</sup> Shanghai Astronomical Observatory, Chinese Academy of Sciences, Shanghai 200030, People's Republic of China
- Received 2021 December 25; revised 2022 September 29; accepted 2022 October 5; published 2022 December 7

## Abstract

We validate the presence of a two-planet system orbiting the 0.15–1.4 Gyr K4 dwarf TOI 560 (HD 73583). The system consists of an inner moderately eccentric transiting mini-Neptune (TOI 560 b,  $P = 6.3980661^{+0.0000095}_{-0.0000097}$  days,  $e = 0.294^{+0.13}_{-0.062}$ ,  $M = 0.94^{+0.31}_{-0.23} M_{\text{Nep}}$ ) initially discovered in the Sector 8 Transiting Exoplanet Survey Satellite (TESS) mission observations, and a transiting mini-Neptune (TOI 560 c,  $P = 18.8805^{+0.0024}_{-0.0011}$  days,  $M = 1.32^{+0.29}_{-0.32} M_{\text{Nep}}$ ) discovered in the Sector 34 observations, in a rare near-1:3 orbital resonance. We utilize photometric data from TESS Spitzer, and ground-based follow-up observations to confirm the ephemerides and period of the transiting planets, vet false-positive scenarios, and detect the photoeccentric effect for TOI 560 b. We obtain follow-up spectroscopy and corresponding precise radial velocities (RVs) with the iSHELL spectrograph at the NASA Infrared Telescope Facility and the HIRES Spectrograph at Keck Observatory to validate the planetary nature of these signals, which we combine with published Planet Finder Spectrograph RVs from the Magellan Observatory. We detect the masses of both planets at  $>3\sigma$  significance. We apply a Gaussian process (GP) model to the TESS light curves to place priors on a chromatic RV GP model to constrain the stellar activity of the TOI 560 host star, and confirm a strong wavelength dependence for the stellar activity demonstrating the ability of near-IR RVs to mitigate stellar activity for young K dwarfs. TOI 560 is a nearby moderately young multiplanet system with two planets suitable for atmospheric characterization with the James Webb Space Telescope and other upcoming missions. In particular, it will undergo six transit pairs separated by  $<6$  hr before 2027 June.

*Unified Astronomy Thesaurus concepts:* [Radial velocity \(1332\)](#)

## 1. Introduction

The Kepler mission, after its launch in 2009, discovered over 4000 transiting exoplanet candidates (Borucki et al. 2011; Howard et al. 2012; Bryson et al. 2021). However, many of these planets orbited relatively faint 14th–16th visual magnitude stars that were difficult to follow up, validate, and confirm (Weiss & Marcy 2014; Marcy et al. 2014; Plavchan et al. 2015; Rogers 2015; Wolfgang et al. 2016). The NASA Transiting Exoplanet Survey Satellite (TESS) mission launched in 2018 to detect and identify relatively nearby and brighter transiting

exoplanets, particularly those orbiting smaller and cooler M dwarf stars, which are the most abundant spectral type, and are known to host compact multiplanet systems (Howard et al. 2012; Dressing & Charbonneau 2015; Ricker et al. 2015). To date, the TESS mission has expanded the pool of nearby, bright transiting exoplanet candidates considerably, with over 4000 candidates identified. Many are amenable to ground-based follow-up and characterization (Ricker et al. 2015).

Kepler has shown that compact multiplanet Neptune and terrestrial planets are more commonly found to orbit M dwarf stars (Howard et al. 2012; Dressing & Charbonneau 2015). Additionally, the relatively small size of M dwarfs in comparison to transiting exoplanets leads to larger, easier-to-detect transit depths, and M dwarfs are the most common spectral types in the Milky Way (Chabrier 2003; Henry et al. 2006). The relatively nearby M dwarf exoplanet discoveries from TESS are therefore some of the most suitable targets for exoplanet atmospheric characterization with ground-based and future space-based facilities such as James Webb Space Telescope (JWST; Kempton et al. 2018). Before jumping to atmospheric characterization, however, the TESS candidates need further supporting observations to validate and confirm

<sup>66</sup> NSF Graduate Research Fellow.

<sup>67</sup> NSF Astronomy and Astrophysics Postdoctoral Fellow.

<sup>68</sup> UC Chancellor's Fellow.

<sup>69</sup> Banting Fellow.

<sup>70</sup> University of Southern Queensland, Centre for Astrophysics, West Street, Toowoomba, QLD 4350 Australia.



that they are not false positives. TESS pixels are  $21''$  in size on the sky, a relatively large value compared to typical ground-based seeing-limited angular resolution of  $\sim 1''$ , a design choice for the TESS mission to optimize its cameras' fields of view (Ricker et al. 2015). As a result, the light from nearby main-sequence stars can be blended with fainter visual eclipsing binaries, and produce false positives, especially when only a singly transiting planet is identified in a 27 day TESS sector of observations at lower ecliptic latitudes away from the ecliptic poles (Ricker et al. 2015; Vanderburg et al. 2019; Bluhm et al. 2020; Brahm et al. 2020; Dreizler et al. 2020; Nowak et al. 2020; Martinez et al. 2020; Teske et al. 2021; Addison et al. 2021a; Cale et al. 2021; Gan et al. 2021; Hobson et al. 2021; Osborn et al. 2021; Sha et al. 2021).

Ground-based panchromatic light curves, high-resolution imaging with high contrasts, and spectroscopic follow-up can search for close visual companions to the candidate host star to validate that the target is not a false positive from a nearby, background, blended, or grazing eclipsing binary, and to ensure that the planetary radius is unbiased by additional flux sources within the TESS aperture. Additional light-curve analyses such as EDI-Vetter Unplugged (Zink et al. 2020) can check for neighboring flux contamination from nearby stars in the sky, examine the abundance of outliers from the transit model, and consider any signal variations between even and odd transits and the presence of any secondary eclipses. The Discovery and Vetting of Exoplanets (DAVE; Kostov et al. 2019) tool evaluates TESS light-curve-based diagnostics such as photocenter motion, odd-even transit-depth consistency, searches for secondary eclipses, and other sources of likely false-positive scenarios.

Constraining and/or measuring the masses of transiting planets with precise radial velocities (RVs) derived from high-resolution spectroscopy further enables validation and confirmation of exoplanet candidates, while also providing constraints on the planet bulk densities (Seager et al. 2007; Rogers & Seager 2010; Zeng et al. 2019). However, RV analysis can be complicated from stellar photospheric activity from young and/or active host stars that can produce RV signals comparable in amplitude to the Keplerian signals of interest. Stellar surface inhomogeneities (e.g., cool spots, and hot plages) driven by the dynamic stellar magnetic field rotate in and out of view, leading to photometric variations over time. The presence of such active regions breaks the symmetry between the approaching and receding limbs of the star, introducing apparent RV variations over time as well (Desort et al. 2007). These active regions further affect the integrated convective blueshift over the stellar disk, and will therefore manifest as an additional net red- or blueshift (Meunier & Lagrange 2013; Dumusque et al. 2014). Various techniques have been introduced to lift the degeneracy between activity- and planetary-induced signals in RV data sets such as line-by-line analyses (Dumusque 2018; Wise et al. 2018; Cretignier et al. 2020) and Gaussian process (GP) modeling (e.g., Haywood et al. 2014; Grunblatt et al. 2015), but such measurements remain challenging due to the sparse cadence of typical RV data sets compared to the activity timescales.

This validation and confirmation process can be greatly aided when multiple transiting planets orbiting the same star are detected, as it is much more difficult to contrive a false-positive scenario that mimics two or more transiting planets at different orbital periods (Lissauer et al. 2012; Rowe et al. 2014). The probability of randomly finding two background eclipsing

binaries in the same TESS pixel is vanishingly small ( $\ll 1\%$ ). However, Kepler did find one single example—KOI-284—out of  $\sim 190,000$  target stars, consisting of two stars in a binary, one hosting a single transiting planet and the other hosting two transiting planets in the same Kepler postage stamp. This “false-positive” scenario was uncovered with dynamical stability analysis due to the very similar orbital periods for two of the planets (Lissauer et al. 2012). Furthermore, multiplanet systems can potentially have “double transits,” making possible the optimal use of limited telescope resources for atmospheric characterization such as JWST (e.g., Lissauer et al. 2011; Bean et al. 2018), and also permitting differential exoplanet characterization (e.g., Ciardi et al. 2013; Weiss et al. 2018; Weiss & Petigura 2020). Multiplanet systems are also of interest for studying dynamical interactions between planets, and inferring population-level information on their formation and evolution (e.g., Lissauer 2007; Zhu et al. 2012; Anglada-Escudé et al. 2013; Mills & Mazeh 2017; Morales et al. 2019).

The discovery of a young multiplanet system can be especially valuable for improving our understanding of exoplanet formation and evolution, both the demographics of the exoplanet architectures, and the atmospheric evolution as a function of stellar age, orbital period, and host star spectral type (Marchwinski et al. 2015; Fulton et al. 2017; Newton et al. 2019; Hirano et al. 2020; Carolan et al. 2020; Benatti et al. 2021; Alvarado-Gomez et al. 2022; Cohen et al. 2022; Feinstein et al. 2022a; Flagg et al. 2022; Ilin & Poppenhaeger 2022; Klein et al. 2022). We know that the orbital properties of planets change over time as shown by the existence of hot Jupiters; we also see evidence for orbital distance dependent mass loss via photo-evaporation, which may be responsible for producing the planet-radius gap and may impact our understanding of the occurrence rate of terrestrial planets at larger orbital separations (Pascucci et al. 2019; Mann et al. 2020; Plavchan et al. 2020; Klein et al. 2021). Therefore, we would benefit from examining the orbital architecture and atmospheric properties of multiplanetary systems over a wide range of evolutionary phases. Multiplanet systems in particular enable a differential comparison within the system between their atmospheric properties, and/or escape from, because any differences will be isolated to differences in the planet mass and orbital separation/irradiation at a common age and spectral type for the host star. For example, the Kepler-51 system ( $\sim 530$  Myr) of three planets contains not only the least dense planets ever discovered but they also lie in a close resonant chain of 1:2:3 (Nava et al. 2020). The existence of this system as well as others around more mature, compact multitransiting systems such as Kepler-89 (Zechmeister et al. 2020) hints at a formation mechanism that includes convergent disk migration and resonance capture (Walkowicz & Basri 2013; David et al. 2019b). An even younger multiplanet system, V1298 Tau, also hints at being a 1:2:3 resonant chain based on transit data (Dreizler et al. 2020). TTV observations of AU Mic have led to the tentative hypothesis of a third candidate planet, d, which may complete a resonant chain this time with a 4:6:9 configuration (Wittrock et al. 2022). Both the v1298 and AU Mic planetary systems show unexpectedly higher densities for some of the planets in the system at very young ages, in contrast to the Kepler-51 system (Cale et al. 2021; Maggio et al. 2022; Tejada Arevalo et al. 2022; Zicher et al. 2022). Already, there are complexities in the architecture of systems over time.

In this work, we identify a two-planet transiting system orbiting the  $\sim 0.5$  Gyr host star TOI 560 (HD 73583 & GAIA

**Table 1**  
Stellar Parameters of TOI 560

Parameter	Value	Reference
Identifiers:		
TIC	101011575	S19
TOI	560	G21
HIP	42401	S07
2MASS	J08384526-1315240	S06
Gaia DR2 & EDR3	5746824674801810816	Gaia
Coordinates and Distance:		
$\alpha$	08:38:45.260	S19
$\delta$	-13:15:24.09	S19
Distance (pc)	$31.5666 \pm 0.03205$	S19
Parallax (mas)	$31.657 \pm 0.0152$	Gaia
$\mu_{\alpha} \cos \delta$ (mas yr <sup>-1</sup> )	$-63.8583 \pm 0.0505$	Gaia
$\mu_{\sigma}$ (mas yr <sup>-1</sup> )	$38.3741 \pm 0.0406$	Gaia
Absolute RV (km s <sup>-1</sup> )	21.52	this work <sup>a</sup>
Physical Properties:		
Age (Gyr)	0.15–1.4	this work <sup>b</sup>
$M_*$ ( $M_{\odot}$ )	$0.702^{+0.026}_{-0.025}$	this work <sup>c</sup>
$R_*$ ( $M_{\odot}$ )	$0.677 \pm 0.017$	this work <sup>c</sup>
$T_{\text{eff}}$ (K)	$4582^{+64}_{-62}$	this work <sup>c</sup>
log $g$ (cgs)	$4.623^{+0.025}_{-0.024}$	this work <sup>c</sup>
Spectral Type	K4	S05
$v \sin i$ (km s <sup>-1</sup> )	<3	this work <sup>d</sup>
$P_{\text{rot}}$ (days)	$12 \pm 0.1$	this work <sup>c</sup>
$\rho$ (g cm <sup>-3</sup> )	$3.17 \pm 0.23$	S19
Luminosity ( $L_{\odot}$ )	$0.1802 \pm 0.0058$	S19
Magnitudes:		
TESS (mag)	$8.59 \pm 0.01$	S19
$B$ (mag)	$10.74 \pm 0.07$	S19
$V$ (mag)	$9.67 \pm 0.03$	S19
Gaia $G$ (mag)	$9.270 \pm 0.005$	G18
Gaia BP (mag)	$9.905 \pm 0.001$	G18
Gaia RP (mag)	$8.546 \pm 0.002$	G18
$J$ (mag)	$7.65 \pm 0.03$	S06
$H$ (mag)	$7.09 \pm 0.05$	S06
$K$ (mag)	$6.95 \pm 0.02$	S06
WISE 1 (mag)	$6.850 \pm 0.037$	W10
WISE 2 (mag)	$6.963 \pm 0.021$	W10
WISE 3 (mag)	$6.921 \pm 0.017$	W10
WISE 4 (mag)	$6.723 \pm 0.084$	W10

#### Notes.

<sup>a</sup> The average of the two observations in Table 12.

<sup>b</sup> Estimated in Section 3.1.3.

<sup>c</sup> From our ExoFASTv2 isochrone-based jointed transit light-curve analysis in Table 3; consistent results are obtained in our reconnaissance spectroscopy and broadband spectral energy distribution (SED) modeling.

<sup>d</sup> Calculated from the rotation period and stellar radius, assuming the stellar-rotation axis is rotating in or near the plane of the sky.

<sup>e</sup> Section 3.1.3 and Figure 3.

**References:** G18: (Gaia Collaboration et al. 2018), G21: (Guerrero et al. 2021), S19: (Stassun et al. 2019), S07: (van Leeuwen 2007), S06: (Skrutskie et al. 2006), S05: (Scholz et al. 2005), W10: (Wright et al. 2010).

EDR3 5746824674801810816; Table 1), which we validate with ground-based photometry, high-resolution imaging, and optical and near-IR (NIR) RVs. The first planet candidate was identified in Sector 8 observations of the TESS mission, and we identify in this work the second candidate with the release of the Sector 34 TESS light curve. The host star TOI 560 is active, and we present a chromatic RV analysis to characterize the

stellar activity jointly with  $>3\sigma$  detections of the exoplanet dynamical masses.

This paper is organized as follows: In Section 2 we present an overview of our observations. In Section 3 we present our analysis of the TESS light curve, one ground-based transit, high-contrast imaging, and RVs from the iSHELL, Planet Finder Spectrograph (PFS), and HIRES spectrometers to validate the planetary nature of the transit signals. In Section 4 we present the results of our analysis of the TESS light curve and RVs. In Section 5 we consider and simulate the dynamical stability of the TOI 560 system, discuss the chromatic RV analysis of the stellar activity, and perform a search for additional RV companions. In Section 6 we present our conclusions and future work.

## 2. Observations

In this Section, we present an overview of all observational data used throughout this analysis. TESS photometric light-curve data and ground-based photometry are presented in Section 2.1, a brief description of reconnaissance spectroscopy is summarized in Section 2.2, high-resolution imaging observations are presented in Section 2.3, and RV observations are detailed in Section 2.4.

### 2.1. Photometric Light Curves

Herein, we present space- and ground-based light curves of the TOI 560 system, respectively, in the following two subsections, the latter of which are summarized in Table 2.

#### 2.1.1. TESS Observations

TOI 560 (TIC 101011575; HD 75383; GAIA EDR3 5746824674801810816) was observed first in TESS Sector 8 from UT 2019 February 2 to UT 2019 February 28, then again in Sector 34 during the TESS extended mission from UT 2021 January 13 to UT 2019 February 9. Stellar properties are listed in Table 1. TOI 560 is in the Hydra constellation and is relatively nearby (31.6 pc) and bright ( $V = 9.67$  mag) making it an ideal candidate for study by TESS. The data collection pipeline was developed by the TESS Science Processing Operations Center (SPOC; Jenkins et al. 2016) and uses a wavelet-based matched filter (Jenkins 2002; Jenkins et al. 2010, 2020). One transit signal was detected during the Sector 8 observations, and fitted with a limb-darkened transit model (Li et al. 2019) with various vetting and diagnostic tests (Twicken et al. 2018) and labeled TOI 560 b (Guerrero et al. 2021), which we hereafter refer to as TOI 560 b. This prompted us to explore the target further with RV measurements (Section 2.4) to verify the TESS candidate and perhaps uncover additional companions in the system. With the release of the Sector 34 light curve, we independently identified by eye a second transiting candidate in the TOI 560 system, which was vetted and adopted as a TOI by the TESS mission as TOI 560 c, which hereafter we refer to as TOI 560 c.

In this work, we specifically analyze the detrended Presearch Data Conditioning Simple Aperture Photometry (PDC-SAP) light curves for Sectors 8 and 34 (Smith et al. 2012; Stumpe et al. 2012, 2014) obtained from the Mikulski Archive for Space Telescopes (MAST).<sup>71</sup> After gathering this data, we normalize the detrended flux in electrons per second so that the

<sup>71</sup> <https://mast.stsci.edu/portal/Mashup/Clients/Mast/Portal.html>

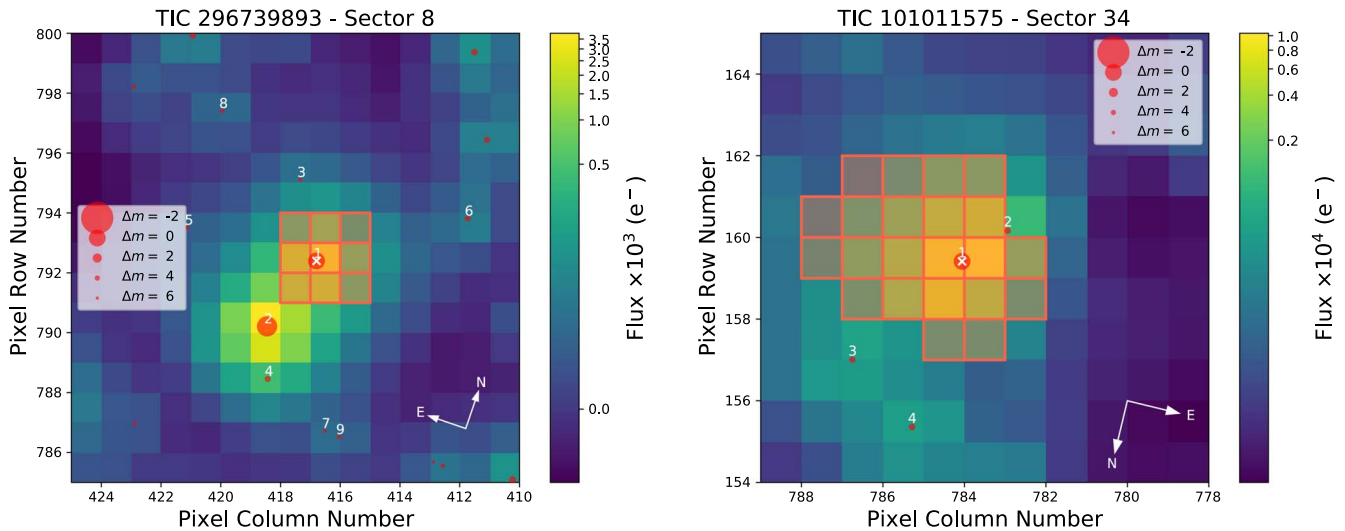


**Figure 1.** TESS target pixel file (TPF) data from Sector 8 (left) and Sector 34 (right) for TOI 560, created with `tpfplotter` (Aller et al. 2020). The pixels shown outlined in orange were the ones used to extract the light curve, while point sources from the Gaia DR2 catalog are labeled in red, with sizes in accordance to their relative magnitude from the target star.

**Table 2**  
Summary of Available Information from ExoFOP-TESS for the Ground-based Light-curve Observations of TOI 560 b

UT Date (YYYYMMDD)	Site	Aperture (m)	Filter	$N_{\text{exp}}$	$t_{\text{exp}}$ (s)	Duration (min)	Pixel Scale ("/px)	FWHM (")	Aperture (")	Transit Coverage
20190427	LCO-SSO	1	B	213	30	151	0.389	5.16	7.4,12.4	Egress
20190427	LCO-SSO	1	zs	84	30	79	0.389	4.19	7.4,12.4	Egress
20190503	LCO-SSO	1	zs	59	30	55	0.389	2.42	6.6,10.9	Ingress
20191207	NGST	4x0.2	NGTS	4840	12	260	4.97	20	40	full
20191207	LCO-CTIO	1	B	211	15	120	0.389	1.93	7.4,12.4	Ingress
20191213	LCO-SSO	1	B	342	15	256	0.389	3.56	6.24	Full
20200114	PEST	0.3	Rc	482	30	357	1.23	4.93	7.4	Full
20200127	LCO-HAL	0.4	zs	363	30	319	0.57	10.7	11.4	Full
20200127	LCO-SSO	0.4	zs	288	30	247	0.57	13.3	12.5	Full
20200202	LCO-SAAO	1	zs	295	30	308	0.389	8.8	10	Full
20200331	LCO-SSO	1	B	281	30	297	0.389	5.25	6.6	Full

**Note.** Site Abbreviations: LCO-CTIO (Cerro Tololo, Chile), LCO-SAAO (South Africa), LCO-SSO (Siding Springs, Australia), LCO-HAL (Haleakala, Hawaii, USA), and NGST (Paranal, Chile)

median for each sector is unity. In Figure 1, we show the TESS target pixel files (TPF) around the target star in Sectors 8 and 34, where orange outlines show the pixels used to create the TESS light curve. There are other point sources (notated by circular red points) that are located within the TESS apertures, so these needed to be subtracted from the SAP flux when creating the PDC-SAP flux.

### 2.1.2. Spitzer Light Curve

TOI 560 b was observed with Spitzer on 2019 August 20, using Director’s Discretionary Time (Crossfield et al. 2018). A single transit was observed using the  $4.5 \mu\text{m}$  channel (IRAC2; Fazio et al. 2004) in subarray mode with an integration time of 0.36 s. The transit observation spanned 6 hr 15 min totaling 823 frames with short observations taken before and after transit to check for bad pixels. Peak-up mode was used to place the star as close as possible to the well-characterized “sweet spot” of the detector.

To extract photometry from the Spitzer observations, we use the Photometry for Orbits Eclipses and Transits (POET<sup>72</sup>) package (Cubillos et al. 2013; May & Stevenson 2020). In summary, POET creates a bad pixel mask and discards bad pixels based on the Spitzer Basic Calibrated Data. Outlier pixels are also discarded using sigma-rejection. Then, the center of the point-spread function (PSF) is determined using a 2D Gaussian fitting technique. After the center of the PSF is found, the light curve is extracted using aperture photometry in combination with a BiLinearly Interpolated Subpixel Sensitivity (BLISS) map described in Stevenson et al. (2012). The resulting data are then simultaneously fit with a model that accounts for both the light curve itself and a temporal ramp-like trend attributed to “charge trapping.” The posterior distribution is sampled using a Markov Chain Monte Carlo (MCMC) algorithm with chains initialized at the best-fit values.

Aperture photometry was performed with various aperture sizes (ranging from 2–6 pixels in increments of 1 pixel). Visual

<sup>72</sup> <https://github.com/kevin218/POET>

inspection of the raw data indicated the temporal ramp model was likely either linear or constant. The optimal aperture size was found to be 3 pixels as this size returned the lowest standard deviation of the normalized residuals (SDNRs) for both ramp models. We then tested bin sizes of 0.1, 0.03, 0.01, and 0.003 pixels square for the BLISS map, finding that a bin size of 0.01 minimized the SDNR. Both the linear ramp and constant models gave similar SDNRs for these tests, so we chose the constant model, the simplest of the two.

### 2.1.3. Las Cumbres Observatory Global Network of Telescopes (LCOGT)

In 2019 and 2020, seven partial or full transit observations of TOI 560 b were collected with five observatory sites from the Las Cumbres Observatory Global network of Telescopes (LCOGT; Brown et al. 2013). These observations are summarized in Table 2. Data were collected in either the B or Sloan  $z'$  filters with exposure times of 15 or 30 s to check for transit-depth chromaticity such as would be produced by a false-positive eclipsing binary scenario. For one transit (UT 2019/04/27), data were collected simultaneously in both filters. For a second transit (UT 2020/01/27), data was collected simultaneously in the same filter from two sites. The other five transits were observed in a single band at a single telescope/site. Data were analyzed using AstroImageJ, and the data reduction was done using the BANZAI LCOGT facility pipeline (McCully et al. 2018).

### 2.1.4. The Perth Exoplanet Survey Telescope (PEST)

The Perth Exoplanet Survey Telescope (PEST) near Perth, Australia is a 0.3 m telescope equipped with a  $1530 \times 1020$  SBIG ST-8XME camera with an image scale of  $1''2/\text{pixel}$ , resulting in a  $31'' \times 21''$  field of view. Observations of a transit of TOI 560 b were obtained on UT 2020 January 14 in the Rc filter with an exposure time of 30 s. A custom pipeline based on C-Munipack was used to calibrate the images and extract differential photometry.

### 2.1.5. NGTS/Paranal

On UT 2019 December 7, the TOI 560 system was observed by the Next Generation Transit Survey (NGTS; Wheatley et al. 2018) using four telescopes (see Bryant et al. 2020), consisting of 0.2 m diameter robotic telescopes, located at ESO's Paranal Observatory, Chile. A custom NGTS filter in the wavelength range 520–890 nm was used. A transit was detected and confirmed for planet b. The NGTS data were reduced using a custom aperture photometry pipeline version 2, which performs source extraction and photometry using the SEP Python library (Bertin & Arnouts 1996; Barbary 2016) and is detailed in Bryant et al. (2020). The pipeline uses Gaia DR2 (Barbary 2016; Gaia Collaboration et al. 2018) to automatically identify comparison stars that are similar in brightness, color, and CCD position to TOI 560.

### 2.1.6. WASP Light Curves

The SuperWASP team monitored TOI 560 for four seasons from 2009–2012 included as part of a larger all-sky survey (Pollacco et al. 2006). Data were reduced and light curves were generated using the standard SuperWASP analyses (Maxted et al. 2011).

## 2.2. Recon Spectroscopy

The purpose of reconnaissance spectroscopy is to provide spectroscopic parameters that will more precisely constrain the properties of planet host stars, to detect false positives caused by spectroscopic binaries as manifested by large (e.g.,  $>1 \text{ km s}^{-1}$ ) RV changes and/or line-doubling in multiepoch spectroscopy, and to identify stars unsuitable for precise RV measurements, such as rapid rotators.

### 2.2.1. NRES

Reconnaissance spectroscopy for TOI 560 was obtained with the Las Cumbres Observatory (LCOGT) Network of Robotic Echelle Spectrographs (NRES). NRES is a fiber-fed echelle spectrograph at several sites mounted on the respective LCOGT 1 m telescopes with wavelength range 380–860 nm and spectral resolution  $R \sim 53,000$ . Observations were executed at the Sutherland Observatory, South Africa, and the McDonald Observatory, USA, on the nights 2019 November 4, 2019 October 29, and 2019 May 12. We took dark, bias, flat, and arc lamp calibration images at the beginning of each night. The target was centered on one fiber, and the second fiber was used to observe a Th-Ar calibration lamp simultaneously. On each night, we took three consecutive exposures with 480 s on each individual spectrum. The S/Ns for each night were 33, 30, and 33, respectively. We obtained the wavelength-calibrated spectra using the NRES commissioning IDL pipeline and obtained improved and stacked spectra for each night using the Stage2 IDL pipeline with a total integration time of 1440 s and a resulting S/N of  $\sim 35$ .

### 2.2.2. TRES

The Tillinghast Reflector Echelle Spectrograph (TRES; Fűrész 2008) team obtained two reconnaissance (median S/N = 33.25) spectra of TOI 560 near opposite quadratures of TOI 560 b (phases 0.25 and 0.72 on the initial Sector 8 released ephemeris) at 2019 April 16 04:37 and 2019 April 19 03:49 UT. TRES has a resolving power  $R \sim 44,000$ , and the wavelength range of the spectrograph is 390–910 nm. The Stellar Parameter Classification (SPC) tool specifically uses a  $\sim 310 \text{ \AA}$  region of the spectrum ( $\sim 5050\text{--}5360 \text{ \AA}$ ) to derive stellar parameters (Section 3.1.1). Spectra are processed following methods described in Buchhave et al. (2010).

## 2.3. High-resolution Imaging

High-resolution imaging is used to obtain images of faint companions located near bright target stars. Typical targets are stars with companions including exoplanets and circumstellar structures and disks of gas and dust. In seeing-limited imaging, a faint companion could be swamped and lost in the noise of scattered light in the PSF wings of the target star. High-contrast imaging methods—speckle imaging and adaptive optics—were designed to mitigate the impact of target star scattered light at the position of the companion, in order to make the companion detectable against the residual PSF noise (e.g., Guyon 2005; Marois et al. 2006; Lafreniere et al. 2007; Mawet et al. 2014).

High-contrast imaging of TESS candidates is crucial to ensure that the target is not a false positive from a background eclipsing binary, and to ensure that the planetary radius is unbiased by additional, unidentified, flux sources within the aperture. Spatially close stellar companions can create a

false-positive transit signal if, for example, the fainter star is an eclipsing binary. However, even more troublesome is “third-light” flux contamination from a close companion (bound or line of sight), which can lead to underestimated derived planetary radii if not accounted for in the transit model (e.g., Ciardi et al. 2015) and even cause total nondetection of small planets residing within the same exoplanetary system (Lester et al. 2021). Given that close bound companion stars exist in nearly one-half of FGK type stars (Matson et al. 2018), high-resolution imaging provides crucial information toward our understanding of exoplanetary formation, dynamics, and evolution (Howell et al. 2021). Herein we present high-contrast imaging of TOI 560 obtained with Gemini with NIRI and Zorro and the SOAR telescope, respectively.

### 2.3.1. Gemini North/NIRI

We searched for close visual companions to the target using high-resolution imaging with both AO and speckle imaging at Gemini. The AO and speckle images are highly complementary: the speckle images reach higher resolutions in the optical, while the AO images reach deeper sensitivities beyond a few hundred milliarcseconds in the NIR, and are therefore more sensitive to more widely separated low-mass stars. We collected high-resolution AO images of TOI 560 with Gemini/NIRI (Hodapp et al. 2003) on 2019 May 26. Given that the star is bright in the K band, we collected images with individual exposure time 0.9 s with the Br $\gamma$  filter (2.166  $\mu$ m), to avoid saturating the detector. Our sequence consisted of nine such images, with the telescope dithered in a grid pattern between each frame, and we also collected daytime flats. The science images themselves can be used to construct a sky background frame, by median combining the dithered images.

### 2.3.2. Gemini South/Zorro

TOI 560 was observed twice on 2020 March 16 and 2019 May 22 UT using the Zorro speckle instrument on the Gemini South 8 m telescope.<sup>73</sup> Six sets of 1000 by 0.06 s exposures were collected for TOI 560 and processed with Fourier analysis in our standard reduction pipeline (see Howell et al. 2011).

### 2.3.3. SOAR telescope

We searched for stellar companions to TOI 560 with speckle imaging on the 4.1 m Southern Astrophysical Research (SOAR) telescope (Tokovinin 2018) on 18 May 2019 UT, observing in the Cousins *I* band a similar visible bandpass as TESS. This observation was sensitive to a 7.5 mag fainter star at an angular separation of 1'' from the target. More details of the observation, data reduction, and analysis are available in Ziegler et al. (2020).

## 2.4. Radial Velocities

Herein we present ground-based precise RV observations collected with high-resolution echelle spectrographs PFS, HIRES, and MINERVA-Australis at visible wavelengths, and iSHELL in the NIR in the following subsections.

### 2.4.1. iSHELL RVs

We have gathered a total of 204 observations of TOI 560 over 30 nights using the iSHELL instrument at NASA InfraRed Telescope Facility (IRTF) atop Maunakea, Hawaii, USA from UT 2020 January 26 to UT 2021 May 29. We observe with iSHELL in KGAS mode covering the wavelengths of 2.18–2.47  $\mu$ m. Our exposure times were always set at 300 s, and were repeated anywhere from 6–14 times consecutively per night to attempt obtaining a signal-to-noise ratio (S/N) per spectral pixel of  $\sim$ 120, though our actual results varied from 46–152 due to variable seeing and atmospheric transparency conditions. A methane isotopologue (<sup>13</sup>CH<sub>4</sub>) gas cell is used in the instrument (Plavchan et al. 2013; Cale et al. 2019) to constrain the line-spread function (LSF) and provide a common reference for the optical path wavelength. Along with each set of exposures within a night, we also collect a set of 5  $\times$  15 s flat-field images with the gas cell removed for data reduction purposes, and particularly to mitigate flexure-dependent and time-variable fringing present in the spectra. In Cale et al. (2019), the RV pipeline is adapted from the CSHELL RV code described in Gao et al. (2016), and the CSHELL code was rewritten in a Python script `pychell`<sup>74</sup> to adapt to iSHELL’s larger spectral grasp with multiple orders.

When the light passes through a gas cell and an echelle spectrograph, the spectrum consists of multiorder spectra of the target with the gas spectrum superimposed, which can be used to subtract off instrument systematic shifts in the wavelength solution and changes in the LSF (Butler et al. 1996). We extract our spectra following the general procedures outlined in Cale et al. (2019). For each of the 29 orders in the regime that we observe between 2.18 and 2.47  $\mu$ m, we do optimal spectral extraction (weighted summation) so that in each column eventually we get a single value, which gives us a 1D spectrum for each order.

The extracted spectra from `pychell` were forward-modeled and analyzed using the methods outlined in Cale et al. (2019), and the updated methods described in Reefe et al. (2021, submitted) briefly described herein. We forward model the extracted spectra independently for each order to account for the stellar spectrum, gas cell, telluric absorption, the LSF, and the spectral continuum to construct a complete spectral model. We find that `pychell` performs better when providing a synthetic stellar template for the stellar model to start from, which is based on properties of the host star.

We assume a solar metallicity and gravity, and we explore synthetic models  $\pm$ 500 K from an initial temperature of 4700 K, based upon the EXO-FOP-TESS values, in increments of 100 K to identify the optimal synthetic stellar template that produces the lowest rms flux residuals in forward modeling our extracted spectra. We use the Spanish Virtual Observatory’s BT-Settl models accessible from their web server,<sup>75</sup> which we further refine by Doppler broadening the spectrum to the rotational velocity of the star (3.1 km s<sup>-1</sup>), as found by TRES extracted spectra (Section 3.1.1). We find that the  $T_{\text{eff}} = 4900\text{K}$  synthetic model minimizes the flux residuals of our observed iSHELL spectra, even though they’re hotter than our adopted stellar temperature, and we use this stellar template as our initial stellar spectrum model guess. Barycenter velocities are also generated as an input via the `barycorrpy` library

<sup>73</sup> <https://www.gemini.edu/sciops/instruments/alopeke-zorro/>

<sup>74</sup> Documentation: <https://pychell.readthedocs.io/en/latest/>.

<sup>75</sup> <https://svo2.cab.inta-csic.es/theory/newov2/index.php?models=bt-settl>

(Kanodia & Wright 2018). After each order is forward-modeled, we generate one RV measurement per order and per exposure. We optimally coadd RVs across orders and exposures within a night using the same procedures as in Cale et al. (2019).

We have filtered out three individual spectra from UT 2020 March 7 and three more individual spectra from UT 8 March 2020, due to modeled RVs that were in disagreement with other spectra from the same night by  $>1 \text{ km s}^{-1}$ . We suspect this is due to an initially poor seeing on the nights of observation of  $1''.3$  that was later improved to  $1''.0$ , giving us overall S/Ns of only 54 and 46, respectively, for the nights. Finally, we discard nights with RV uncertainties  $>20 \text{ m s}^{-1}$ .

#### 2.4.2. PFS RVs

We obtained 14 RVs of TOI 560 from PFS on the 6.5 m Magellan II Telescope at Las Campanas Observatory in Chile. These spectra were reduced, and RVs were extracted and published in the Magellan-TESS Survey I paper (Teske et al. 2021). The PFS Spectrograph has a resolution of  $R = 120,000$  and wavelength range of 391–734 nm. The observations were carried out between UT 2019 April 18 and May 24.

#### 2.4.3. HIRES RVs

We include 14 Keck-HIRES (Vogt et al. 1994) observations of TOI 560 in our analyses. Keck-HIRES is located atop Maunakea, Hawaii, USA with spectral resolution  $R = 67,000$ . The majority of these observations took place between UT 2019 October 20 and 2020 January 21, with the final night contemporaneous with the start of iSHELL RVs. Exposure times range from 204–500 s, yielding a median S/N  $\approx 234$  at 550 nm per spectral pixel. HIRES spectra are processed and RVs computed via methods described in Howard et al. (2010).

#### 2.4.4. MINERVA-Australis RVs

MINERVA-Australis collected two nights of observations of TOI 560 (Addison et al. 2019, 2021a). MINERVA-Australis consists of an array of four independently operated 0.7 m CDK700 telescopes situated at the Mount Kent Observatory in Queensland, Australia (Addison et al. 2019). Each telescope simultaneously feeds stellar light via fiber optic cables to a single KiwiSpec R4–100 high-resolution ( $R = 80,000$ ) spectrograph (Barnes et al. 2012) with wavelength coverage from 480–620 nm. We obtained a total of 10 individual spectra of TOI 560 on UT 2019 May 23 and UT 2019 May 29 using three and two of the four MINERVA-Australis telescopes, respectively—twice per night per telescope—and exposure times of 30–60 minutes. Wavelength calibration is achieved using a simultaneous Th-Ar calibration fiber. RVs were derived by cross-correlation, where the template being matched is the mean spectrum. Given that only two nightly RV data points were obtained, we do not include the MINERVA-Australis RVs in the remainder of the analysis presented herein.

### 3. Analysis

In this Section, we present our analysis of the TOI 560 system. In Section 3.1 we present the stellar host characterization. In Section 3.2 we present the light-curve analysis, including the discovery of the transits of TOI 506 c, false-positive vetting metrics, and characterization of the

out-of-transit stellar activity in both the TESS and SuperWASP light curves. Finally, in Section 3.3 we present the analysis of the TOI 560 RV data aided with a stellar activity model constrained by the light-curve analysis.

#### 3.1. Stellar Host Characterization

Our analysis and understanding of exoplanets is directly dependent on our understanding of their host stars (e.g., Ballard et al. 2014). We measure planetary masses and radii in terms of their host stars’ masses and radii, we derive elemental abundance ratios from those in the atmosphere of their host star, and we infer surface temperatures and conditions informed by their host stars’ luminosities, ages, and levels of activity. Host star properties are precisely determined through spectroscopic analysis; therefore, herein we analyze in turn the reconnaissance spectra of TOI 560, fitting bulk stellar properties from the broadband spectral energy distribution (SED), and we solidify our analysis with high-contrast imaging to exclude faint flux-contaminating companions.

##### 3.1.1. Reconnaissance Spectroscopy

The reconnaissance spectroscopy observations reveal a typical late K dwarf. Stellar parameters from the NRES spectra were obtained using SpecMatch (Vanderburg et al. 2019), and summarized in Table 11. For the TRES spectra, there is a small velocity difference that is consistent with the photometric ephemeris, given that the data were collected approximately at opposite quadratures. In Table 12, the results for the stellar parameters for the two TRES observations are presented, as well as values from the SPC tool (Buchhave et al. 2012, 2014). Given the absence of any large bulk RV changes or spectroscopic binarity, we do not coadd the multiepoch spectroscopy to improve the cumulative S/N (and consequently reduce the stellar parameter uncertainties), due to current systematic limitations in these approaches (e.g., Duck et al. 2022). We adopt floor errors of 50 K in  $T_{\text{eff}}$ , 0.10 in  $\log(g)$ , 0.08 in  $[\text{m}/\text{H}]$ , and  $0.5 \text{ km s}^{-1}$  in  $V_{\text{rot}}$ . Note that  $V_{\text{rot}}$  does not include a correction for the contribution of macroturbulence, and the velocities in Table 12 are on the TRES native system and do not correct for the gravitational redshift. The TRES and NRES analyses yield consistent stellar characterization, with the SPC analysis favoring a slightly higher but not statistically significant rotational velocity and metallicity.

##### 3.1.2. Bulk Stellar Properties

We undertake two independent analyses of the broadband SED of the star, and we describe each in turn. The first approach is particularly useful for assessing the evidence for any near-UV (NUV) excess from consideration of the broadband photometry alone. Our second approach is used for our adopted final stellar parameters and is based upon holistic modeling of the SED jointly with the transit light curves and model isochrones.

First, we performed a single-parameter fit of the SED of the star together with the Gaia EDR3 parallax (with no systematic offset applied; see, e.g., Stassun & Torres 2021), in order to determine an empirical measurement of the stellar radius and following the procedures described in Stassun & Torres (2016), Stassun et al. (2017), and Stassun et al. (2018). We use the  $UBV$  magnitudes from the compilation of Mermilliod (2006), the  $JHK_S$  magnitudes from the Two Micron All Sky Survey (2MASS),

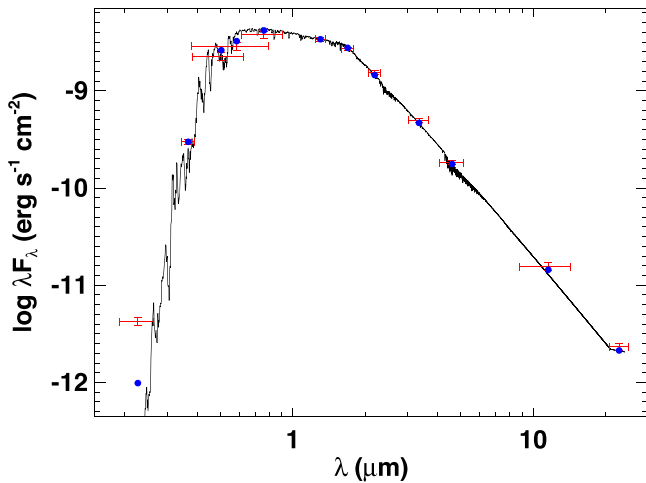


**Figure 2.** SED of TOI 560 from the first of our two independent SED analyses; this analysis is particularly suited for the identification of the NUV excess. Red symbols represent the observed photometric measurements, where the horizontal bars represent the effective width of the passband. Blue symbols are the model fluxes from the best-fit NextGen atmosphere model (black).

the W1–W4 magnitudes from the Wide-field Infrared Survey Explorer (WISE; Wright et al. 2010), the  $G_{BP}G_{RP}$  magnitudes from Gaia, and the NUV magnitude from GALEX. Together, the available photometry spans the full stellar SED over the wavelength range 0.2–22  $\mu\text{m}$  (see Figure 2). We used a NextGen stellar atmosphere model, fixing the model effective temperature ( $T_{\text{eff}}$ ), metallicity ( $[\text{Fe}/\text{H}]$ ), and surface gravity ( $\log g$ ) to the values derived from the TRES SPC analysis in Section 3.1.1 and Table 12. The remaining free parameter is the extinction  $A_V$ , which we fixed at zero given the proximity of the TOI 560 system to Earth. The resulting fit (Figure 2) has a reduced  $\chi^2$  of 1.7, excluding the GALEX NUV flux, which indicates a moderate level of activity (see below). Integrating the (unreddened) model SED gives the bolometric flux at Earth,  $F_{\text{bol}} = 6.01 \pm 0.14 \times 10^{-9} \text{ erg s}^{-1} \text{ cm}^{-2}$ . Taking the  $F_{\text{bol}}$  and  $T_{\text{eff}}$  together with the Gaia parallax gives the stellar radius  $R_* = 0.656 \pm 0.016 R_\odot$  (consistent with the NRES analysis). In addition, we can estimate the stellar mass from the empirical relations of Torres et al. (2010), giving  $M_* = 0.69 \pm 0.04 M_\odot$ , which is consistent with the less precise but empirical estimate of  $M_* = 0.75 \pm 0.08 M_\odot$  obtained directly from  $R_*$  together with the spectroscopic  $\log g$ .

Second, we determine characteristics of the host star, such as effective temperature, gravity, and metallicity, by performing a joint ameba fit followed by MCMC posterior sampling of both stellar properties and planet properties of TOI 560 b and c assuming a two-planet, single-star scenario (from the TESS transit data) simultaneously with EXOFASTv2. EXOFASTv2 is an (IDL) framework for MCMC simulations of exoplanet transits and RVs created by Eastman et al. (2013). Details on the planet transit analysis are given in Section 3.2, but here we present the stellar modeling analysis steps. We start the MCMC with as few assumptions as possible—namely, we place no priors on the spectral type. To ensure we cover an adequate portion of parameter space to find a believable result, we employ parallel tempering with eight parallel threads, following Eastman et al. (2019). We place priors on V-band extinction, parallax, and metallicity summarized in Table 5 along with the priors used in the transit analysis. We simultaneously fit with Mesa Isochrones and Stellar Tracks

(MIST) and an SED function. We then use the posteriors of this run as priors for a second iteration MCMC analysis to examine the stability of the solution and adopt our final stellar parameters.

The results of our EXOFASTv2 stellar characterization are shown in and Table 3. The analysis yields a typical K dwarf consistent with the reconnaissance spectroscopy and SED analysis presented in Section 3.1. We provide two separate estimates for  $R_*$  and  $T_{\text{eff}}$  corresponding to the MIST results and the SED results, respectively. SED results are marked with the subscript SED, while MIST results have no subscript. We adopt the MIST values for the remainder of the analysis, but both sets of values are consistent with one another and with the analysis carried out with the SED and reconnaissance spectroscopy. Finally, we note that the age estimate from EXOFASTv2 shown in Table 3 is drawn from a very flat posterior distribution and is not a reliable estimate; e.g., the stellar age is unconstrained from this particular analysis. Instead, we adopt the final rotation period of  $12.2 \pm 0.1$  days as described in Section 3.1.3.

Finally, TOI 560 has a GAIA RUWE value of 1.030, which is consistent with a single star (Stassun & Torres 2021). The RUWE statistic is an indication of the goodness of fit of the astrometric solution, and values  $>1.4$  have been shown to be associated with unresolved binaries. A search of EDR3 also shows no stars with similar parallaxes within  $75'$ , so TOI 560 likely does not possess any distant, resolved binary companions either.

### 3.1.3. Age Metrics—Is TOI 560 a Young System?

Lomb-Scargle periodograms of the SuperWASP seasonal light curves show a clear and consistent rotation period in each season for TOI 560 of 12 days, with evolution of the light-curve features between seasons (Figure 3). The periodogram peak is statistically significant in all seasons (p-value  $< 1\%$ ) and the average periodogram peak period from all four seasons yields a rotation period of  $12.2 \pm 0.1$  days. We next use the star’s NUV excess (Figure 2) to estimate the star’s rotation and age via empirical rotation–activity–age relations. The observed NUV excess implies a chromospheric activity of  $\log R'_{\text{HK}} = -4.5 \pm 0.1$  via the empirical relations of Findeisen et al. (2011), which is fully consistent with the measured value of  $-4.45 \pm 0.05$  from Gomes da Silva et al. (2021) and  $-4.60$  from our HIRES spectra. The HIRES and TRES spectra show core Ca II HK flux in emission, consistent with this moderate level of activity. This value of  $\log R'_{\text{HK}}$  in turn implies a stellar-rotation period of  $P_{\text{rot}} = 14 \pm 4$  d via the empirical relations of Mamajek & Hillenbrand (2008). This rotation period estimate is also consistent with that estimated from the spectroscopic  $v \sin i$  and  $R_*$ , which gives  $P_{\text{rot}}/\sin i = 11 \pm 3$  day. Thus, the observed photometric modulation, NUV excess, and the observed rotational velocity all yield consistent rotation periods. This establishes the rotation period of the TOI 560 host star.

However, this 12 day rotation period is roughly a factor of 2 slower than that reported by Canto Martins et al. (2020), who reported a “dubious” rotation period 7.17 days from their independent TESS light-curve analysis. We can also estimate rotation periods for TOI 560 by performing Lomb-Scargle periodograms (Lomb 1976; Scargle 1982) of the TESS Sector 8 and 34 light curves of TOI 560. In Figure 4, the TESS light curves contain significant peaks at 12.7 days for PDCSAP and 14.1 days for SAP, both for the Sector 8, respectively, that are

**Table 3**  
Median Values and 68% Confidence Interval for the Stellar Host, TOI 560, from Our EXOFASTV2 Analysis

Stellar Parameters	Units	Values			
$M_*$	Mass ( $M_\odot$ )	$0.702^{+0.026}_{-0.025}$			
$R_*$	Radius ( $R_\odot$ )	$0.677 \pm 0.017$			
$R_{*,SED}$	Radius <sup>a</sup> ( $R_\odot$ )	$0.6819^{+0.0099}_{-0.0094}$			
$L_*$	Luminosity ( $L_\odot$ )	$0.1823^{+0.0062}_{-0.0060}$			
$F_{Bol}$	Bolometric Flux ( $(\text{erg s}^{-1}) \text{cm}^{-2}$ )	$5.85 \times 10^{-9} \pm 2 \times 10^{-10}$			
$\rho_*$	Density ( $\text{g cm}^{-3}$ )	$3.19^{+0.26}_{-0.24}$			
$\log g$	Surface gravity ( $\text{cm s}^{-2}$ )	$4.623^{+0.025}_{-0.024}$			
$T_{eff}$	Effective Temperature (K)	$4582^{+64}_{-62}$			
$T_{eff,SED}$	Effective Temperature <sup>b</sup> (K)	$4568 \pm 45$			
[Fe/H]	Metallicity (dex)	$-0.055^{+0.044}_{-0.052}$			
[Fe/H <sub>0</sub> ]	Initial Metallicity <sup>c</sup>	$-0.051^{+0.057}_{-0.062}$			
Age	Age <sup>d</sup> (Gyr)	$6.7^{+4.7}_{-4.5}$			
EEP	Equal Evolutionary Phase <sup>e</sup>	$329^{+13}_{-30}$			
$A_v$	V-band extinction (mag)	$0.076^{+0.046}_{-0.051}$			
$\sigma_{SED}$	SED photometry error scaling	$1.68^{+0.77}_{-0.44}$			
$\bar{\omega}$	Parallax (mas)	$31.683 \pm 0.032$			
d	Distance (pc)	$31.562 \pm 0.032$			
Wavelength Parameters	Units	B	R	$z'$	
$u_1$	linear limb-darkening coeff	$0.50^{+0.037}_{-0.32}$	$0.68^{+0.037}_{-0.38}$	$0.58^{+0.44}_{-0.38}$	
$u_2$	quadratic limb-darkening coeff	$0.27^{+0.038}_{-0.044}$	$0.02^{+0.045}_{-0.038}$	$0.18^{+0.043}_{-0.046}$	
$A_D$	Dilution from neighboring stars	...	...	...	
Telescope Parameters	Units	HIRES	PFS		
$\gamma_{rel}$	Relative RV Offset ( $\text{m s}^{-1}$ )	$0.1^{+3.5}_{-3.6}$	$-10.8^{+2.2}_{-2.3}$	$0.5 \pm 3.1$	
$\sigma_J$	RV Jitter ( $\text{m s}^{-1}$ )	$12.7^{+3.4}_{-2.4}$	$8.0^{+2.5}_{-1.7}$	$10.9^{+3.1}_{-2.5}$	
$\sigma_J^2$	RV Jitter Variance	$160^{+97}_{-55}$	$64^{+47}_{-24}$	$119^{+79}_{-48}$	

**Notes.** See Table 3 in Eastman et al. (2019) for a detailed description of all parameters.

<sup>a</sup> This value ignores the systematic error and is for reference only.

<sup>b</sup> This value ignores the systematic error and is for reference only.

<sup>c</sup> The metallicity of the star at birth.

<sup>d</sup> This posterior is relatively flat and unconstrained, and does not take into account the stellar-rotation period analysis estimated in Section 3.1.3 and/or Figure 3.

<sup>e</sup> Corresponds to static points in a star's evolutionary history. See Section 2 in Dotter (2016).

not obvious integer fraction multiples of one another nor of 7.17 days; we do find a secondary peak at 7.29 days for the Sector 8 light curve, consistent with Canto Martins et al. (2020). However, the dominant period in the Sector 8 light curve at 12.7 days is reasonably consistent with the WASP, NUV, and rotational velocity inferred rotation periods. A more detailed FF<sup>7</sup> modeling of the TESS light curves in Section 3.2.3 with a GP and uniform rotation period prior from 2–20 days also favors a rotation period of  $7.13^{+0.31}_{-0.13}$  days, also consistent with Canto Martins et al. (2020). However, given that the time segments of the TESS light curve in-between data downlinks are themselves <12 days in time baseline, we find that the TESS light curves themselves are insensitive to a 12 day rotation period and are thus not reliable; the 7.1 and 5.6 day power in the TESS light curves may be from a combination of the first harmonic of the stellar-rotation period at  $P_{rot}/2$ , potentially the spot evolution timescale, and the presearch data conditioning (PDC) of the TESS PDC-SAP light curves. Thus, we adopt the rotation period of  $12.2 \pm 0.1$  days from the SuperWASP light curves in the remainder of our analysis.

For this rotation period, using the age–rotation relation from Mamajek & Hillenbrand (2008) based upon the power-law model of Barnes (2007), we derive a stellar age estimate of  $\tau_* = 591^{+130}_{-97}$  Myr. However, Curtis et al. (2020) recently

showed that for K dwarfs like TOI 560, there is an age–rotation “pile-up” at rotation periods of  $\sim 10$ –15 days where the spin-down of K dwarfs stalls between ages  $\sim 0.6$ –1.4 Gyr, before resuming for ages  $> 1.4$  Gyr. We also verified whether TOI 560 may be a plausible member of a nearby moving group or association with the BANYAN  $\Sigma$  (Gagné et al. 2018) tool, which compares the XYZ Galactic coordinates and UVW space velocities of known stellar associations and assigns a membership probability based on Bayes’ theorem with the option to marginalize over unknown quantities such as heliocentric RVs. We find a negligible membership probability to all 27 young associations included in BANYAN  $\Sigma$ . We also compared the XYZ and UVW of TOI 560 to those of 1000 moving groups and open clusters identified in the literature so far within 500 pc of the Sun, and we find no plausible association to which TOI 560 may belong to. Inspecting the position of TOI 560 in a Gaia eDR3 (Gaia Collaboration et al. 2018) color–magnitude diagram (Figure 5) reveals a picture consistent with an age of at least 100 Myr. TOI 560 has been detected in GALEX DR5 (Bianchi et al. 2011), and its position in a GALEX-Gaia color–color diagram (Figure 6) shows that it is located on the UV-bright end of field stars and on the UV-faint end of the Pleiades members with similar Gaia eDR3  $G - G_{RP}$  color (which tracks spectral types), thus indicating that TOI 560 is likely older than the Pleiades, but plausibly on the younger end of the age

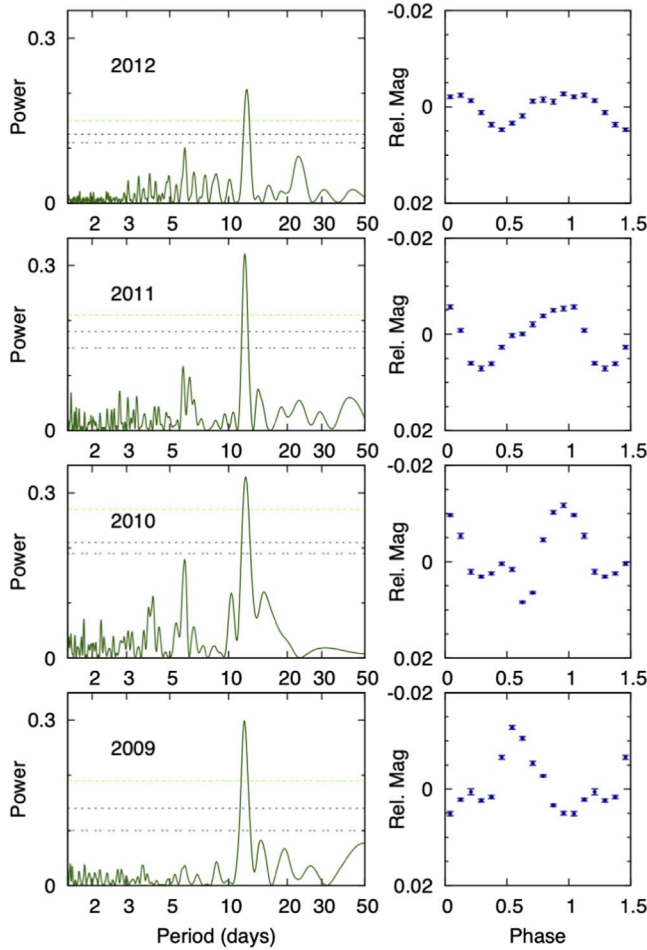


**Figure 3.** Left panels: Lomb-Scargle periodograms of the light curves of TOI 560 from the SuperWASP survey in 2009–2012 from bottom to top, plotted in green as a function of period on the horizontal axis and power on the vertical axis. Right panels: phased seasonal light curves of the SuperWASP TOI 560 seasonal light curves in the same reverse annual order. The light curves are binned in phase in 0.05 increments in blue with the coadded uncertainties shown, with rotational phase on the horizontal axis and relative and normalized apparent magnitude on the vertical axis. Spot evolution is readily apparent from year to year, including some double-humped features from spots on the northern and southern hemispheres of the star.

distribution of field stars, and consistent with the rotation-based age estimate. Additionally, there is no lithium detected, consistent with this star not being  $<100$  Myr (Delgado Mena et al. 2015). We thus conclude from the rotation period of TOI 560 and the K dwarf rotational evolution pile-up that the age of TOI 560 is between 150 Myr and 1.4 Gyr.

#### 3.1.4. High-contrast Imaging

For the Gemini/NIRI observations, we carried out the data reduction using a custom set of IDL codes, with which we removed bad pixels, sky-subtracted and flat-corrected the frames, and then aligned the stellar position between frames and coadded the images (Hodapp et al. 2003). For Gemini South, we utilize only the observations from 2019 May, as the March observations had poorer seeing and sky conditions, albeit giving similar results to those obtained about a year earlier. Zorro provides simultaneous speckle imaging in two bands (562 and 832 nm) with output data products including a reconstructed image in Figure 7 with robust contrast limits on companion detection (e.g., Howell et al. 2016).

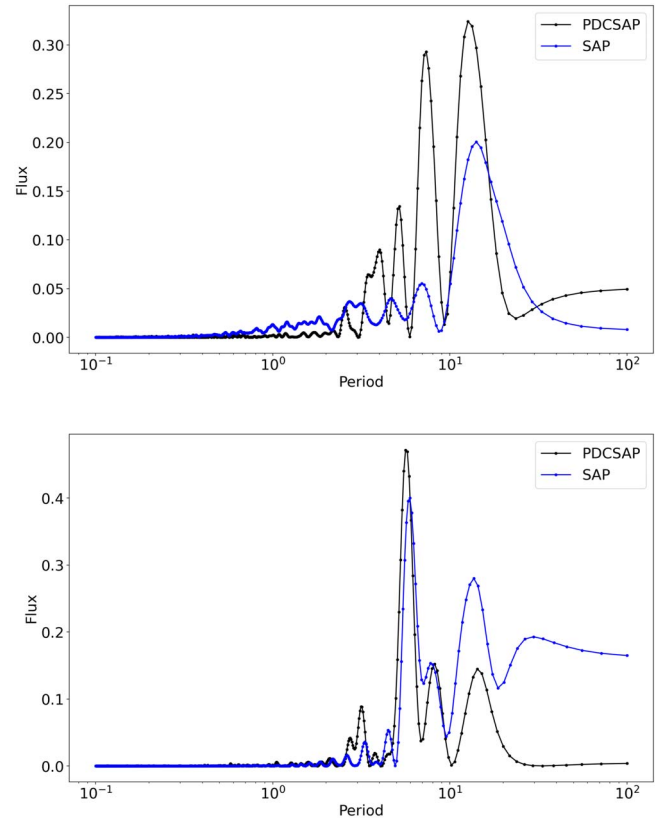


**Figure 4.** TESS PDC-SAP and SAP Sectors 8 (top) and 34 (bottom) rotation periods.

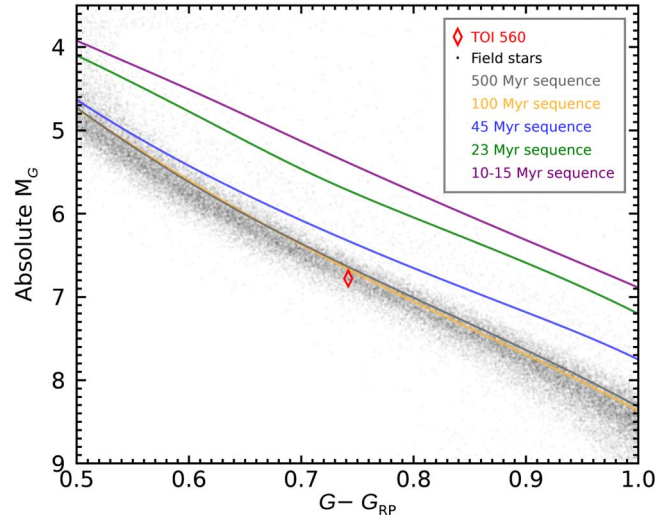


**Figure 5.** Gaia DR3 color-magnitude diagram for TOI 560 (red diamond) compared to nearby field stars (black dots) and empirical age-dated sequences built from the members of nearby coeval associations (thick colored lines; see Gagné et al. 2021). The position of TOI 560 is consistent with an age  $\approx 100$  Myr or older, and ages of 45 Myr and younger are clearly ruled out.

For our Gemini/NIRI observation, we did not identify visual companions anywhere in the field of view, which extends to at least  $7''$  in all directions from the target star, and TOI 560 appears single to the limit of the Gemini/NIRI resolution. The sensitivity as a function of separation is shown in Figure 7, along with an image of the target. The images are sensitive to companions 8 mag fainter than the host star in the background limited regime (beyond  $\sim 1''$ ). For our Gemini South

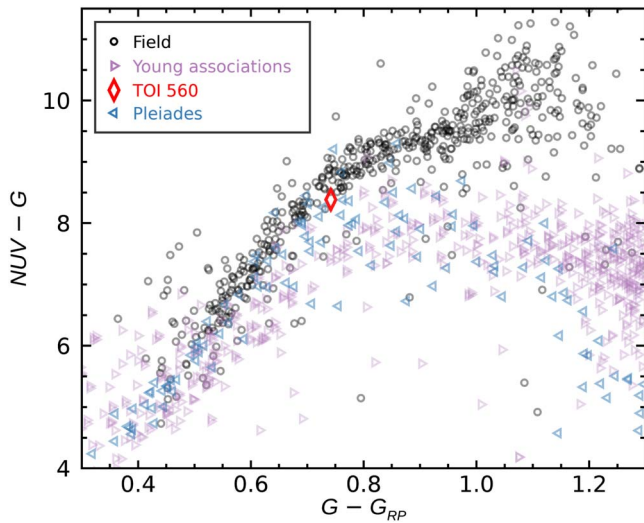


**Figure 6.** GALEX-Gaia color-color diagram for TOI 560 (red diamond) compared to nearby field stars detected in GALEX (black circles), members of various nearby, young associations with ages in the range 5–100 Myr (right-pointing purple triangles; see Gagné et al. 2018), and members of the Pleiades (left-pointing blue triangles;  $112 \pm 5$  Myr; Dahm 2015; Gagné et al. 2021). TOI 560 falls on the UV-bright end of the field distribution, but on the UV-faint end of the Pleiades distribution, compared to other stars of a similar Gaia  $G - G_{RP}$  color.

observations, Figure 7 shows our final  $5\sigma$  contrast curves and the reconstructed speckle images. We find that TOI 560 is single to within the contrast limits achieved by the observations. No companion is identified brighter than 5–8 mag below that of the target star from the diffraction limit (20 mas) out to  $1''$ . At the distance of TOI 560 ( $d = 31$  pc), these angular limits correspond to spatial limits of 0.6–37 au. Finally, for our SOAR observation, Figure 7 shows the  $5\sigma$  detection sensitivity and speckle autocorrelation functions from the observations. No nearby stars were detected within  $3''$  of TOI 560 in the SOAR observations.

### 3.2. Light-curve Analysis

In this section, we vet against false-positive scenarios using different tests in Section 3.2.1, and then we analyze the TESS Sector 34 light curve to discover TOI 560 c in Section 3.2.2. After that, we apply our GP analysis to the light curves in Section 3.2.3, and using EXOASTv2 in Section 3.2.4, we jointly analyze the Sector 8 and 34 TESS light curves as a two-planet system.

#### 3.2.1. Vetting against False Positive

Before investing detailed resources in the RV analysis of a TESS candidate planetary system, it is useful to rule out false-positive scenarios caused by eclipsing binaries and other systematics, and there are numerous diagnostics that we employ using the TESS light curves alone. We ran two separate vetting analyses on the TOI 560 data gathered by TESS.

The first of our vetting tests was performed with the EDI-Vetter Unplugged tool (Zink et al. 2020).<sup>76</sup> EDI-Vetter Unplugged checks for several diagnostics that could be indicative that the target is a false positive. First, EDI-Vetter checks for neighboring flux contamination from nearby stars in the sky, to make sure that the signal is indeed correlated with

the expected target; this is necessary due to the large angular size of TESS pixels. Second, it examines the abundance of outliers from the transit model, as well as the validity of each individual transit—e.g., odd/even test, if transits fall into masked data gaps. Third, it also searches for the statistically significant presence of any secondary eclipses, which could indicate an eclipsing binary. Other measures that are considered are the similarities between transit signals, the phase coverage of transit signals, and the relative length of transit duration in comparison to period. The results of our EDI-Vetter analysis are presented in Table 4.

Second, we also scrutinized the TESS light curves using the DAVE software (Kostov et al. 2019) developed at the NASA Goddard Space Flight Center. This tool evaluates similar criteria as the EDI-Vetter tool, such as odd/even transit differences and secondary eclipses, but also searches for any photocenter shift, or the difference between the TIC position and the measured photocenter of the transits during transit, which is often also a diagnostic of a blended eclipsing binary.

In our EDI-Vetter analysis, two of the criteria were flagged as a potential false positive: the uniqueness of the transit signal and the planet masks (Table 4). However, the latter is due to the system being a multiplanet system, with two different transiting planets, and the former a transit of TOI 560 c falling into the data download gap of Sector 8. In our DAVE analysis, we show full transit data and phased odd/even, secondary, tertiary, and positive transits for each sector in Figures 38 and 39. We see little to no variation between the primary odd and even transits, and we see no statistically significant drop in flux during the expected ephemerides for a secondary eclipse or tertiary transit. However, we note the appearance of an odd–even transit-depth difference for TOI 560 b. Due to the youth of the star, there is significant out-of-transit variability from the star that is not filtered out by the DAVE vetting tool. This in turn impacts its transit-depth determination, resulting in the even–odd discrepancy. Thus, we effectively ignore this metric present in the DAVE tool as a potential sign of a false positive, which is supported by the multiplanet nature of the system.

We also see no statistically significant positive flux variation that could be indicative of lensing between eclipsing binary stars. The evaluation of the photocenter shift during transit helps validate that the transit belongs to the target star, and not a faint companion. Photocenter difference plots for each sector are shown in Figure 40, and overall show no major variations between the expected and observed locations. Thus, this vetting analysis from DAVE and EDI-Vetter, combined with our high-contrast imaging, rules out a blended or background eclipsing binary companion, and confirms that the transit signals originate from TOI 560, and not another nearby point source. Further, when the increasingly low probability (e.g.,  $<1\%$ , Lissauer et al. 2012) that multiple blended or background eclipsing binaries would be spatially coincident with TOI 560 and produce two different eclipsing signals near a 3:1 orbital period coincidence are combined, we can conclude that TOI 560 is the host of the two eclipsing companions. We next turn to presenting our results on constraining the masses of TOI 560 b and c.

#### 3.2.2. The Discovery of TOI 560 c

With the release of the TESS Sector 34 light curve, we readily identified by eye two transits of a second planet candidate with an orbital period of  $\sim 18.9$  days. Several other teams independently identified this second transiting planet

<sup>76</sup> [https://github.com/jonzink/EDI\\_Vetter\\_unplugged](https://github.com/jonzink/EDI_Vetter_unplugged)

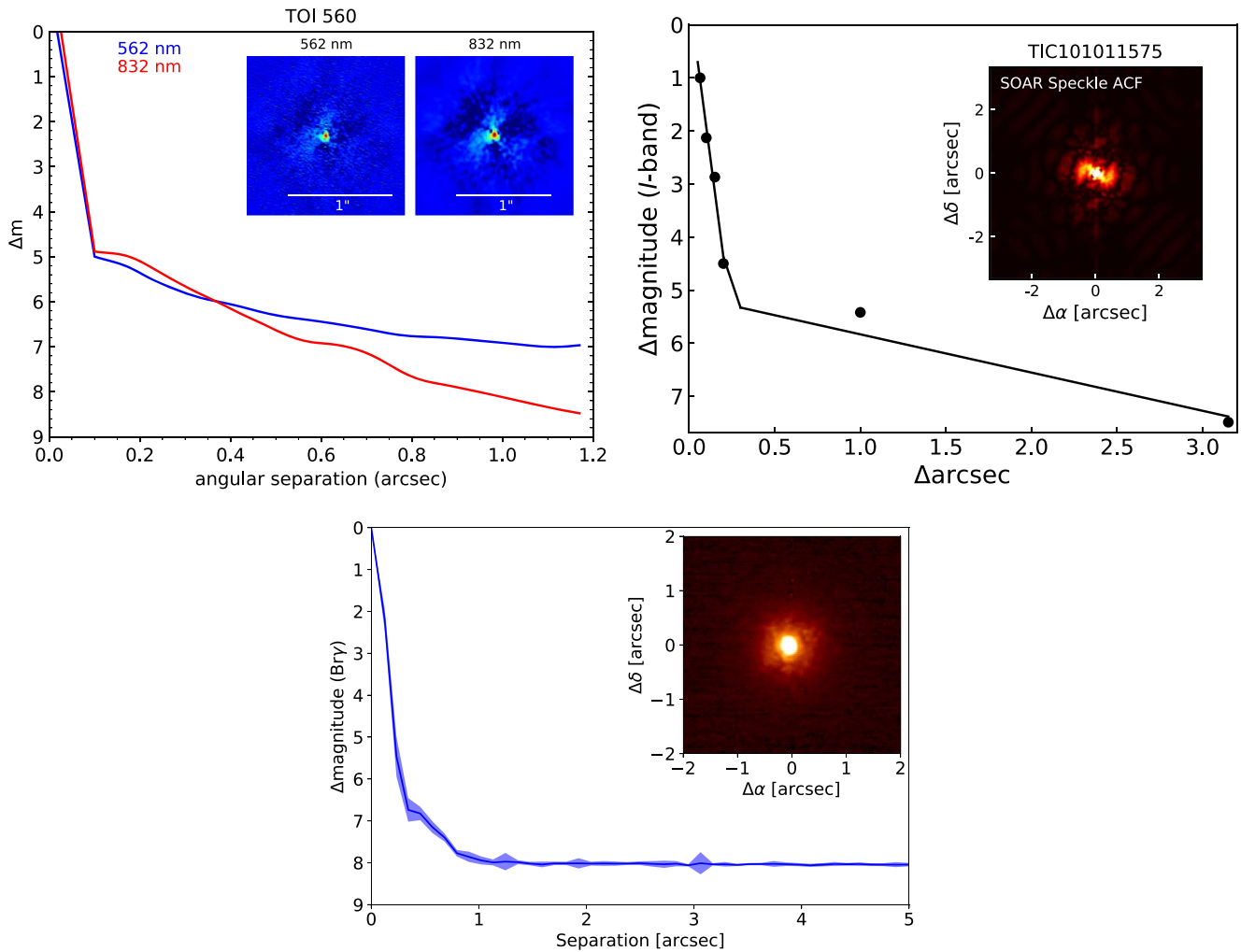


**Figure 7.** Top left: our  $5\sigma$  contrast curves and the reconstructed speckle images observed using the Zorro speckle instrument on the Gemini South 8 m telescope. Sensitivity is quoted on the vertical axis in magnitudes relative to the host star, as a function of angular separation on the horizontal axis. Inset: a cutout of our image, centered on the target star TOI 560. Top right: same as top-left, showing the  $5\sigma$  detection sensitivity and speckle autocorrelation functions from the SOAR observations. Bottom: same as the top two panels, showing our sensitivity of the Gemini/NIRI observations to companion stars, as a function of separation from the host star. No visual companions are seen anywhere in all of our high-contrast imaging data, and the star appears single.

**Table 4**

Sector 8 and 34 Results for False-positive Signals Analyzed by EDI-Vetter Unplugged

Vetting Report	Sector 8	Sector 34
Transit Count	6	6
Flux Contamination	False	False
Too Many Outliers	False	False
Too Many Transits Masked	False	True
Odd/Even Transit Variation	False	False
Signal Is Not Unique	True	True
Secondary Eclipse Found	False	False
Low Transit Phase Coverage	False	False
Transit Duration Too Long	False	False
Signal Is a False Positive	True	True

**Note.** The software found no evidence for false positives in this data. The software version used was 0.1.3.

during our analysis, which was identified by the TESS mission as TOI 560 c ( $P_c = 18.8805$  days). After masking the transits of TOI 560 b ( $P_b = 6.3980$  days), we computed BLS

(Kovacs et al. 2002) and TLS (Hippke & Heller 2019) periodograms and phased light curves (LCs) of the Sector 34 light curve in Figure 8. Due to unfortunate timing, TOI 560 c did not transit in the Sector 8 TESS light curve (Figure 8). We also excluded a period for TOI 560 c of one-half its value, as a third transit of TOI 560 c could have occurred during a downlink data gap in the TESS Sector 34 light curve. However, under that scenario, a transit of TOI 560 c would have occurred in the Sector 8 light curve, which is ruled out.

### 3.2.3. GP Analysis of the Light Curves

Stars are not uniform disks; they exhibit RV variations from rotationally modulated activity, e.g., star spots and plages on the surface of the star (Dumusque et al. 2011a, 2011b; Plavchan et al. 2015; Fischer et al. 2016, and references therein). Depending on the temperature contrast between magnetically active regions and the surrounding photosphere of the star, these active regions will induce an apparent RV shift that is quasiperiodic as the active regions evolve on timescales distinct from the rotation period of the star. GPs have been widely and successfully employed in modeling the apparent RVs due to stellar activity (Haywood 2015).

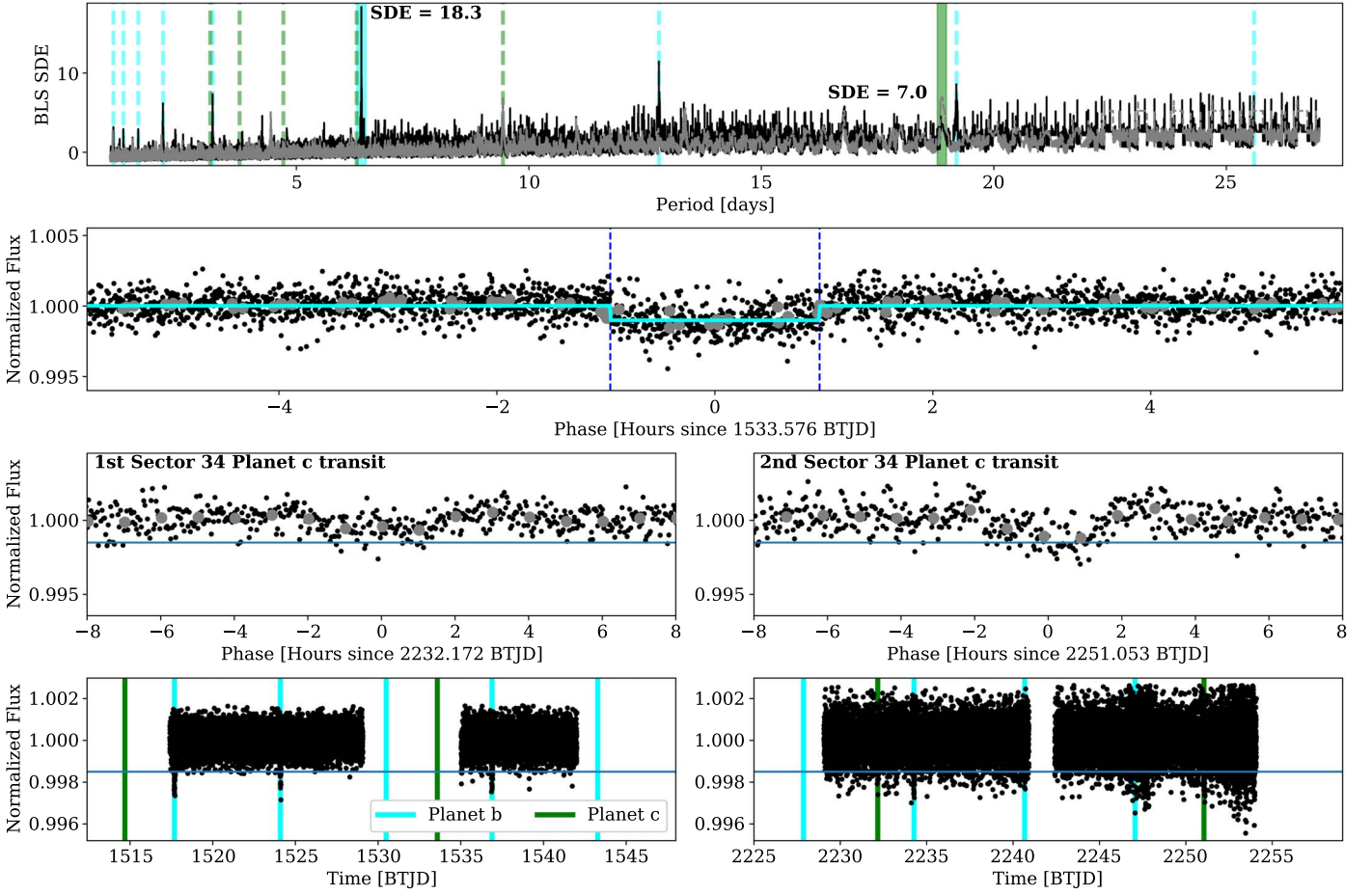


**Figure 8.** Top: joint BLS periodograms of the Sector 8 and 34 TESS light curves, before (black) after (gray) removing the transits of TOI 506 b, plotted as a function of period in days with the BLS standard deviation statistical significance power on the vertical axis (SDE). The periods of b and c are indicated as teal and green shaded regions, respectively. The vertical dashed lines correspond to integer ( $2x$ ,  $3x$ ,  $4x$ , etc.) and integer fraction ( $1/2$ ,  $1/3x$ ,  $1/4x$ , etc.) multiples of these periods in teal and green for b and c, respectively, as well. Note that the time units of BTJD are BJD-2457000.0 days. Second row: phased light curve for the two transits of TOI 560 c in the Sector 34 TESS light curve as unbinned black and binned (one hour) gray dots, plotted as a function of time in hours on the horizontal axis with respect to the transit conjunction time, and the normalized flux on the vertical axis. A teal transit model is overlaid. The blue dashed vertical lines correspond to the time of conjunction and transit ingress and egress. Third row: same as the second row, but the individual transits of TOI 560 c are plotted separately. Fourth row: the Sector 8 (left) and 34 (right) light curve of TOI 560, where the transit times of TOI 560 b and c are marked in teal and green, respectively, plotted as a function of time and normalized flux. This shows that TESS just missed observing TOI 560 c during this initial sector. The horizontal blue line is a line corresponding to 2 ppt, the approximate depth for TOI 560 c.

The same active regions also give rise to photometric variations from the hemisphere visible to the observer. Thus, we can model the light curves of TOI 560 out of transit with a GP, and use the light-curve hyperparameter posteriors to constrain the GP model hyperparameter priors for our subsequent analysis of the RVs, following the  $FF'$  technique (Aigrain et al. 2012). This method allows us to generate what a simulated RV curve would look like from the stellar activity:

$$\Delta \text{RV}_{\text{spots}}(t) = -F(t)F'(t)R_*/f. \quad (1)$$

Here,  $F$  is the photometric flux,  $F'$  is the derivative of  $F$  with respect to time,  $f$  represents the relative flux drop for a spot at the center of the stellar disk, and  $R_*$  is the stellar radius.

Our GP kernel describes the functional covariance between any two measurements separated in time. The kernel by definition must be a square, symmetric covariance matrix “ $K$ ” of length equal to the number of observations. We follow Haywood (2015) who introduced the quasiperiodic (QP)

Kernel composed of a decay and periodic term:

$$K_{QP}(t_i, t_j) = \eta_\sigma^2 \overbrace{\exp\left[-\frac{\Delta t^2}{2\eta_\tau^2}\right]}^{\text{Decay}} \overbrace{\exp\left[-\frac{1}{2\eta_l^2} \sin^2\left(\pi \frac{\Delta t}{\eta_p}\right)\right]}^{\text{Periodic}} \quad (2)$$

where  $\Delta t = |t_i - t_j|$ . Here,  $\eta_p$  typically represents the stellar-rotation period,  $\eta_\tau$  is the mean spot lifetime, and  $\eta_l$  is the relative contribution of the periodic term, which may be interpreted as a smoothing parameter (larger is smoother).  $\eta_\sigma$  is the amplitude of the autocorrelation of the activity signal. The set of  $\{\eta_\sigma, \eta_\tau, \eta_p, \eta_l\}$  constitutes the set of GP model hyperparameters that are constrained by the data. There exist families of stellar activity models that generate a particular covariance matrix given by a specific set of hyperparameters, and thus GPs are a flexible framework for characterizing the nondeterministic time evolution of stellar activity. The  $FF'$  analysis does enable us to estimate the expected amplitude of

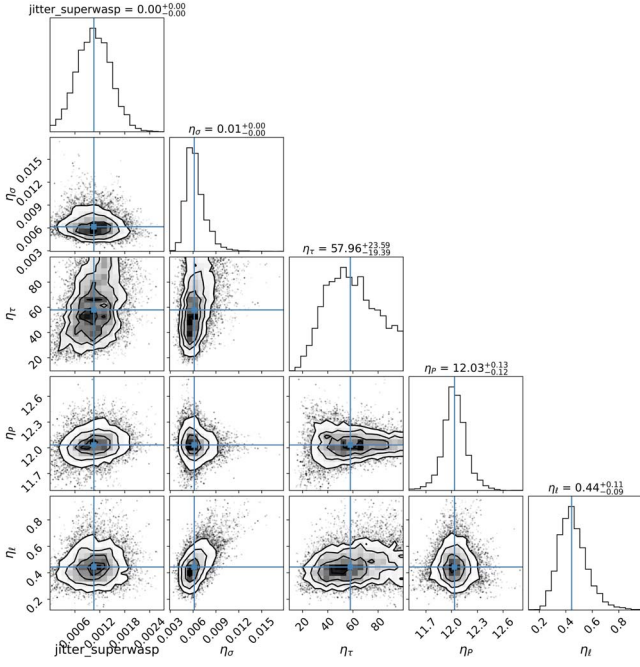


**Figure 9.** Posterior distributions (along diagonal) and two-parameter covariances (off-diagonal) for the quasiperiodic kernel GP model hyperparameters of the SuperWASP light curves. The five GP hyperparameters as described in the text are indicated and median and 68% confidence interval ranges are displayed at the top of each posterior distribution; median values are also indicated with horizontal and vertical blue lines for the covariance plots, and vertical lines for the posterior distribution. For the covariance plots,  $1\sigma$ ,  $2\sigma$ , and  $3\sigma$  contours are shown in place of the individual sample values  $<3\sigma$  from the medians.

the RV variations at wavelengths comparable to the light-curve observations,  $\eta_\sigma$ , but we end up not using that amplitude in our RV modeling. Instead, we do use the  $FF'$  analysis to get estimates of the remaining hyperparameters, particularly  $\eta_\tau$ ,  $\eta_p$ , and  $\eta_l$  for use in the RV analysis.

We first apply our GP model to the SuperWASP data for the four seasons together (Figure 3). We use wide uniform priors on hyperparameters  $\eta_\sigma \sim \mathcal{U}(0, 50)$ ,  $\eta_\tau \sim \mathcal{U}(1, 100)$ , and  $\eta_l \sim \mathcal{U}(0.02, 1)$ . Instead of accounting for intrinsic uncertainties in the light curve, we also fit a jitter term  $\eta_{LC}$ . For the hyperparameter  $\eta_p$ , we use a prior of  $\mathcal{U}(11.5, 13)$  based on periodogram analysis of the WASP light curves in Section 3.1.3. We recover from the MCMC of the WASP data a spot lifetime  $\eta_\tau$  of  $57.96^{+23.59}_{-19.39}$  days, a rotation period of  $\eta_p$  of  $12.03^{+0.13}_{-0.12}$  days, and a smoothing hyperparameter  $\eta_l = 0.44^{+0.11}_{-0.09}$ , which are all consistent with our young star; such long spot lifetimes are seen for other young systems (Figure 9; e.g., Cale et al. 2021). We adopt these three posteriors as priors in constraining the GP model for our RV stellar activity analysis.

We next analyze both sectors of TESS PDC-SAP and SAP separately in order to see if we can recover similar GP kernel hyperparameters  $\{\eta_\sigma, \eta_\tau, \eta_p, \eta_l\}$  to our SuperWASP analysis. We first median normalize the TESS SAP light curve, and mask out the transits and the edges of the light-curve data, particularly for Sector 8, where there exists a spacecraft systematic producing a “ramp-up” effect at the start of the sector and after the data downlink gap mid-sector. We then fit the remaining light curve via a cubic-spline regression (`scipy.interpolate.LSQUnivariateSpline`;

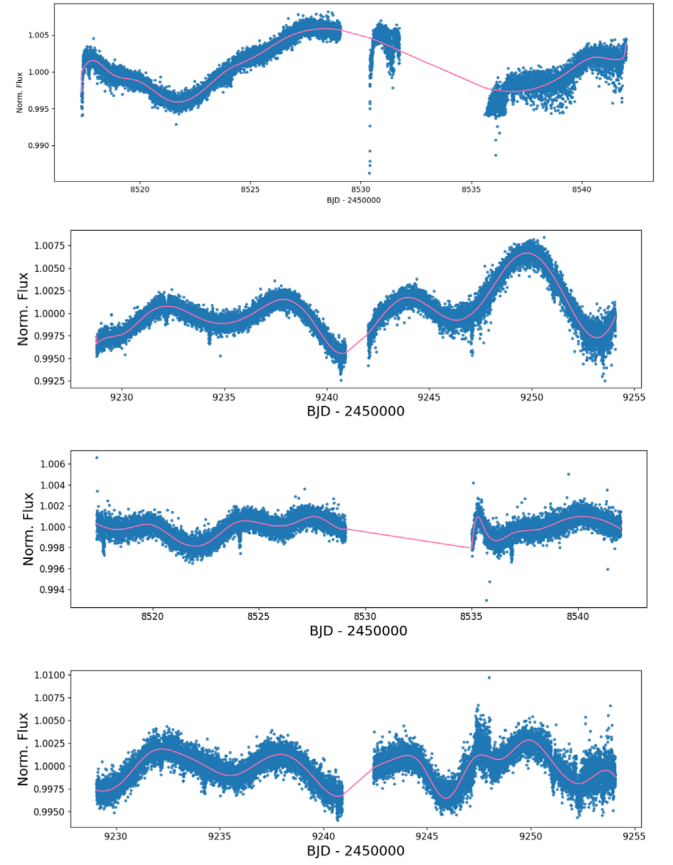


**Figure 10.** The TESS SAP (top two) and PDC-SAP (two bottom) light curves of TOI 560 from Sectors 8 and 34, plotting the normalized flux on the vertical axes as a function of time on the horizontal axes. The light curves are shown as blue data points, and the cubic-spline regression is shown as the pink line. The interpolation in the data gap downlink region in the middle of each sector is subsequently discarded in our analysis. Significant photometric modulation due to stellar activity is apparent in both sectors.

Virtanen et al. 2020) for each sector individually with knots sampled in units of 1.3 days (excluding any that happen to fall within the TESS data dump regions). The particular value of 1.3 is chosen to be small with respect to the stellar activity timescales, but long with respect to the cadence, so transits are “smoothed” over to produce a “noiseless” and smooth representation of the light curves. Then, in Figure 10 we apply the  $FF'$  technique (Aigrain et al. 2012) to the spline regression fits.

We used a uniform prior centered on 12.2 days for the stellar-rotation period hyperparameter. As expected due to the relatively short TESS time baselines of two  $\sim 13$  day observing sequences per sector, the TESS light curve does not constrain the stellar-rotation period further than the information inferred from the SuperWASP light-curve analysis.

For the TESS SAP Sector 8 (34; 8+34) light curve, we recover from the MCMC a spot lifetime  $\eta_\tau$  of  $12.94^{+23.55}_{-9.03}$  ( $10.10^{+23.49}_{-6.62}$  days;  $15.97^{+22.55}_{-11.74}$  days) (Figure 11). In other words, the TESS light-curve analysis leads to a significantly shorter spot lifetime analysis than inferred from the SuperWASP analysis as well, even for the SAP fluxes, but we discard these results as a consequence of the shorter TESS time baseline compared to the SuperWASP light curve, even though the former is at higher photometric precision. For the TESS SAP Sector 8 (34; 8+34) light curve, we recover from the MCMC a

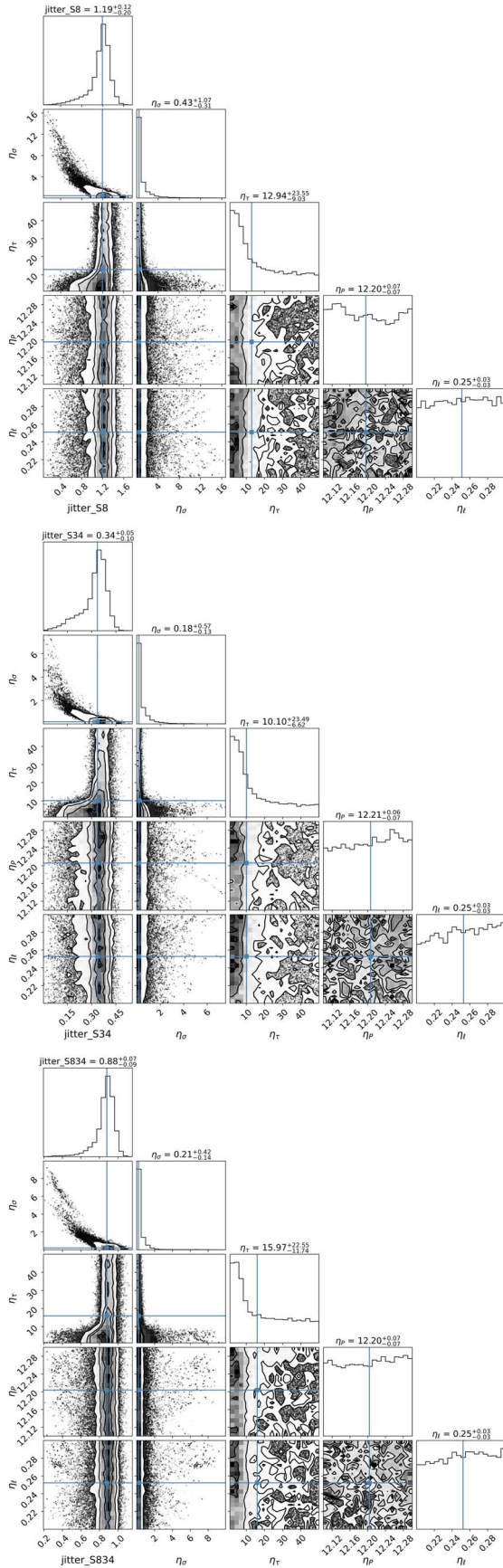


**Figure 11.** Posterior distributions (along diagonal) and two-parameter covariances (off-diagonal) for the quasiperiodic kernel GP model hyperparameters of the  $FF'$  analysis of the TESS SAP light curves.

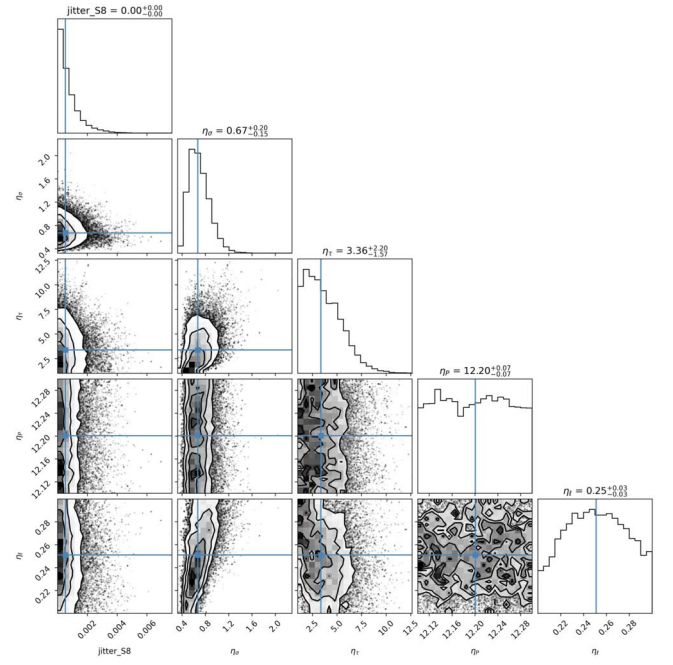


**Figure 12.** Posterior distributions (along diagonal) and two-parameter covariances (off-diagonal) for the quasiperiodic kernel GP model hyperparameters of the  $FF'$  analysis of the TESS PDC-SAP Sector 8 light curves.

smoothing hyperparameter  $\eta_l = 0.25 \pm 0.03$  ( $\eta_l = 0.25 \pm 0.03$ ;  $\eta_l = 0.25 \pm 0.03$ ), and these are all somewhat smaller than the value inferred from the SuperWASP analysis, and this could potentially be due to the higher precision of the TESS light curves and improved photometric sampling of the rotation period. Finally, from an MCMC of the TESS PDC-SAP light curves, we recover an even shorter spot lifetime  $\eta_{r_s}$ , indicating that the PDC can lead to introducing systematics that lead to inaccurate characterization of the stellar activity (Figure 12).

### 3.2.4. ExoFAST

In this section, we perform an EXOFASTv2 analysis of the candidate planet's transit light curves. After normalizing the TESS PDC-SAP data as described in Section 2, we cut out a region of at least 8 hr around each individual transit and create separate data files for each transit and use these as input data for EXOFASTv2.

We jointly model the TESS, Spitzer, and ground-based light curves, and all RVs with EXOFASTv2. The EXOFASTv2 RV results are presented in Appendix H in Figure 41. However, while ExoFAST can jointly model the light curves and RVs, the EXOFASTv2 RV model does not account for the stellar activity manifested in the RV measurements. Thus, we perform an independent modeling of the RVs with a stellar activity model in Section 3.3.

Our minimal set of priors are detailed in Table 5, including the period  $P$ , time of conjunction, and planetary radius  $R_p/R_*$  for TOI 560 b and c (the EXOFASTv2 full results are in Table 7). We allow other model parameters, i.e., eccentricity  $e$ , inclination  $i$ , and argument of periastron  $\omega$  to vary with no imposed priors, starting with circular  $e$  and edge-on  $i$  values. The posterior values for this initial MCMC run are then used as the initial values for a second iteration run, though we keep the same uniform and Gaussian priors as the initial run. We allow this second run to run

**Table 5**  
Planetary and Stellar Prior Probability Distributions for Our EXOFASTv2 MCMC Simulations

Parameter [Units]	Initial Value [ $P_0$ ]	Priors
$P_b$ (days)	6.3981	$\mathcal{U}(P_0 \pm 10\%)$
$TC_b$ (days)	2458517.69007	$\mathcal{U}(P_0 \pm P/3)$
$P_c$ (days)	18.881	$\mathcal{U}(P_0 \pm 10\%)$
$TC_c$ (days)	2458533.59092	$\mathcal{U}(P_0 \pm P/3)$
$R_{p,b}/R_*$	0.0388	...
$R_{p,c}/R_*$	0.0382	...
$M_{p,b}/M_\odot$	0.000030	...
$M_{p,c}/M_\odot$	0.000030	...
$R_*$	0.674	...
$R_{*,SED}$	0.679	...
$T_{eff}$ (K)	4599.94	...
$T_{eff,SED}$ (K)	4591.85	...
feh	-0.031	$\mathcal{N}(-0.210, 0.080)$
initfeh	-0.043	...
eep	319.8	...
$\log M_*$	-0.145	...
$A_V$	0.097	$\mathcal{U}(0, 0.143)$
errscale	1.22	...
distance (pc)	31.567	...

**Note.**  $\mathcal{U}(\ell, r)$  signifies a uniform prior with left bound  $\ell$  and right bound  $r$ .  $A_V$  is the galactic extinction in the  $V$  band, “feh” is metallicity, “initfeh” is the initial metallicity at the time of the zero-age main sequence, “eep” stands for equivalent evolutionary point,  $\log M_*$  is the log of the stellar mass, and “errscale” is the error scale. The eccentricity  $e$  and the argument of periastron  $\omega$  are assumed to be circular, with no priors.

longer, and we confirm the second MCMC converges on the same results within  $1\sigma$  to check for the robustness of the MCMC posteriors. Note that the model is parameterized in the EXOFASTv2 standard basis for transit only fits. This model parameterization is  $\{TC, \log P, R_p/R_*, \cos i, \sqrt{e} \sin \omega, \sqrt{e} \cos \omega\}$  (Eastman et al. 2019).

### 3.3. RV Analysis

In this section, we jointly analyze our RVs (Table 15) from three spectrographs (iSHELL, PFS, and HIRES). We analyze the RVs as a planetary system with a chromatic GP stellar activity model, and make model comparisons. We constrain our GP model hyperparameters from the SuperWASP light-curve analysis, in particular the stellar-rotation period and spot lifetime timescale.

#### 3.3.1. Planet System Multispectrograph RV Analysis

To jointly model the RVs from iSHELL, PFS, and HIRES, we again use `pychell`, this time in combination with the co-dependent package `optimize`, which is a general-purpose Bayesian analysis tool that `pychell` expands upon with RV-specific MCMC tools. In Section 5.2 we show that no statistically significant periodic signals were identified in the raw RVs, and so we proceed herein with the assumption of a two-planet model in our Bayesian analysis with the ephemerides from TESS. Each planet in our model consists of five parameters, which comprise a complete orbit basis: the period  $P$ , time of conjunction  $TC$ , eccentricity  $e$ , argument of periastron  $\omega$ , and RV semiamplitude  $K$ , with subscripts denoting the planet that said parameter is

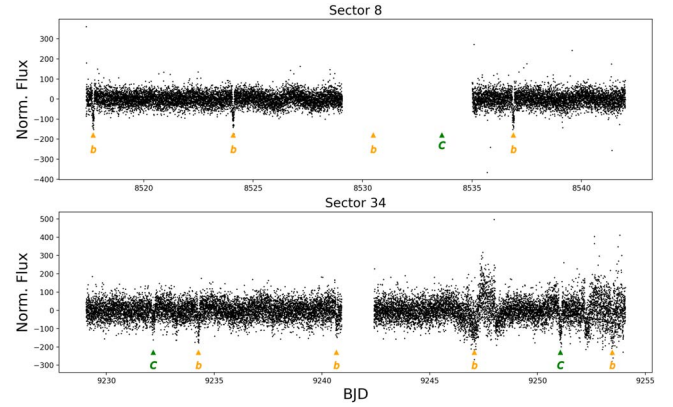


**Figure 13.** TESS Sector 8 (top) and 34 (bottom) TESS light curves, after subtracting from the PDC-SAP time-series the cubic-spline fit model for the stellar activity in Figure 10, shown as normalized flux on the vertical axis as a function of time in BJD on the horizontal axis. The transit midpoint times of TOI 560 b and c are indicated.

associated with (in this case, b and c). We next include a GP model for the stellar activity, which is described further in the next subsection. We also include an absolute RV offset term ( $\gamma$ ) to account for the average overall recessional velocity of the star, and a jitter term ( $\sigma$ ) that quantifies the variational RV amplitude not accounted for by any modeled planets, stellar activity, or instrumental noise that is nonfrequency dependent on our timescales of interest (e.g., white noise). Analyses of the PDC-SAP TESS transit data (Section 4.1.1, Figure 13 and Table 5) shows a period and time of conjunction consistent with those listed on the ExoFOP-TESS database in the TESS Object of Interest (TESS Project section)<sup>77</sup> (Akeson et al. 2013), which are  $P_b = 6.398069 \pm 0.000015$  days,  $P_c = 18.879744 \pm 0.000162$ ,  $TC_b = 2458517.690108 \pm 0.000747$  days, and  $TC_c = 2458533.620329 \pm 0.005422$ , all of which have uncertainties that are orders of magnitude finer than we can hope to resolve with our RV cadence. We thus decide to lock both parameters at their nominal values for all analyses in this paper. For all MCMC results quoted, the median value is defined as the 50th percentile, while the lower and upper uncertainty bounds are the 15.9th and 84.1th percentile posterior confidence intervals, respectively. We sample the posterior distributions using the `emcee` package (Foreman-Mackey et al. 2013) for a subset of models to determine parameter uncertainties, always starting from the MAP-derived parameters (i.e., affine invariant is our actual sampler). We perform a burn-in phase of 1000 steps followed by an MCMC analysis for approximately 50 times the median autocorrelation time (steps) of all chains. The prior, posterior distributions, and results of this model are given in Section 4. Finally, we also perform a model comparison test (Table 9) by calculating the  $\ln \mathcal{L}$ , small-sample Akaike Information Criterion (AIC; Akaike 1974; Burnham & Anderson 2002), and Bayesian information criterion (BIC) for each combination of planets in our model. These results are shown in Section 4.2.

#### 3.3.2. Stellar Activity RV Model—RVs

Rather than applying an independent GP model to each individual RV data set for PFS, HIRES, and iSHELL, we extend the kernel in Equation (1) to utilize a single global

<sup>77</sup> <https://exofop.ipac.caltech.edu/tess/target.php?id=101011575>

**Table 6**Model Parameters and Prior Distributions Used in Our RV Model That Considers the Transiting b and c Planets, as Well as the Recovered MAP Fit and MCMC Posteriors for the  $J_2$  Kernel

Parameter [units]	Initial Value ( $P_0$ )	Priors	MAP Value $J_2$	MCMC Posterior $J_2$
$P_b$ (days)	6.3980661	locked <sup>a</sup>	...	...
$TC_b$ (days)	2458517.68971	locked <sup>a</sup>	...	...
$e_b$	0.294	$\mathcal{U}(0, 1); \mathcal{N}(P_0, 0.13)$	0.0.33	$0.29^{+0.09}_{-0.09}$
$\omega_b$	$130\pi/180$	$\mathcal{U}(P_0 - \pi, P_0 + \pi); \mathcal{N}(P_0, 45\pi/180)$	4.11	$3.94^{+0.26}_{-0.49}$
$K_b$ ( $\text{m s}^{-1}$ )	10	$\mathcal{U}(0, \infty)$	6.57	$6.98^{+1.76}_{-1.82}$
$P_c$ (days)	18.8805	locked <sup>a</sup>	...	...
$TC_c$ (days)	2458533.593	locked <sup>a</sup>	...	...
$e_c$	0.093	$\mathcal{U}(0, 1); \mathcal{N}(P_0, 0.13)$	0.19	$0.19^{+0.10}_{-0.10}$
$\omega_c$	$-190\pi/180$	$\mathcal{U}(P_0 - \pi, P_0 + \pi); \mathcal{N}(P_0, 45\pi/180)$	-3.87	$-3.53^{+0.62}_{-0.063}$
$K_c$ ( $\text{m s}^{-1}$ )	10	$\mathcal{U}(0, \infty)$	6.80	$6.64^{+1.36}_{-1.42}$
$\gamma_{\text{ISHELL}}$ ( $\text{m s}^{-1}$ )	$\text{MEDIAN}(\text{RV}_{\text{ISHELL}}) + \pi/100^{\text{b}}$	$\mathcal{N}(P_0, 100)$	4.22	$3.52^{+4.63}_{-4.62}$
$\gamma_{\text{PFSS}}$ ( $\text{m s}^{-1}$ )	$\text{MEDIAN}(\text{RV}_{\text{PFSS}}) + \pi/100^{\text{b}}$	$\mathcal{N}(P_0, 100)$	-13.28	$-13.30^{+17.87}_{-17.63}$
$\gamma_{\text{HIRES}}$ ( $\text{m s}^{-1}$ )	$\text{MEDIAN}(\text{RV}_{\text{HIRES}}) + \pi/100^{\text{b}}$	$\mathcal{N}(P_0, 100)$	4.59	$7.07^{+13.68}_{-13.48}$
$\eta_P$	12.03	$\mathcal{N}(P_0, 0.13)$	12.02	$12.00^{+0.09}_{-0.0}$
$\eta_\ell$	0.44	locked <sup>a</sup>	...	...
$\eta_\tau$	57.96	locked <sup>a</sup>	...	...
$\eta_{\sigma,0}$	1	$\mathcal{J}(0.67, 50)$	23.42	$27.87^{+5.58}_{-4.30}$
$\eta_\lambda$	1.17	$\mathcal{U}(-1, 2)$	0.61	$0.66^{+0.30}_{-0.30}$

**Notes.** Initial values for orbital period, timing conjunction, eccentricity, and planet radius for both planets as well as stellar mass come from our ExoFAST analysis in Section 3.2.4, and the stellar activity model hyperparameters and prior distributions come from our SuperWASP light-curve analysis in Section 3.2.3.

<sup>a</sup> Locked indicates the parameter is fixed. Gaussian priors are denoted by  $\mathcal{N}(\mu, \sigma)$ , uniform priors by  $\mathcal{U}(\text{lower bound, upper bound})$ , and Jeffrey’s priors by  $\mathcal{J}(\text{lower bound, upper bound})$ . The +1 on the initial gamma values is in case the RVs are already median-subtracted, and to pseudo-randomize this initial parameter.

<sup>b</sup> We want the initial value to be the median of the RVs for that spectrograph; the +1 is used in case the median is already zero, as Nelder–Mead solvers cannot start at zero.

(joint) GP model and covariance kernel across multiple spectrographs. We follow Cale et al. (2021) where they already implemented our desired framework in two Python packages. As in Cale et al. (2021), we first reparameterize the GP amplitude through a linear kernel, hereafter referred to as the  $J_1$  kernel as in Cale et al. (2021), as follows:

$$K_{J_1}(t_i, t_j) = \eta_{\sigma,s(i)} \eta_{\sigma,s(j)} \times \exp[...]. \quad (3)$$

Here,  $\eta_{\sigma,s(i)}$  and  $\eta_{\sigma,s(j)}$  are the effective stellar activity amplitudes for each spectrograph  $s$  at times  $t_i$  and  $t_j$ , respectively, where  $s(i)$  represents an indexing set between the observations at time  $t_i$ .<sup>78</sup> In the  $J_1$  kernel, each instrument is given its own independent amplitude hyperparameter,  $\eta_{\sigma,s(i)}$ , but the other three hyperparameters are shared between all instruments. Also, the covariance kernel is still square, but now has dimensions corresponding to the total number of observations across all spectrographs, and thus represents a “joint” covariance matrix.

Second, to first order, we expect the amplitude from stellar activity to be linearly proportional to frequency (or inversely proportional to wavelength; Cale et al. 2021). This approximation is a direct result of the spot-contrast scaling with the photon frequency (or inversely with wavelength) from the ratio of two blackbody functions with different effective temperatures (Reiners et al. 2010). Thus, we also consider a variation of this kernel that further enforces the expected inverse relationship between the amplitude with wavelength. As in

Cale et al. (2021), we parameterize the kernel to become:

$$K_{J_2}(t_i, t_j, \lambda_i, \lambda_j) = \eta_{\sigma,0}^2 \left( \frac{\lambda_0}{\sqrt{\lambda_i \lambda_j}} \right)^{2\eta_\lambda} \times \exp[...], \quad (4)$$

which hereafter we refer to as the  $J_2$  kernel, as in Cale et al. (2021). Here,  $\eta_{\sigma,0}$  is the effective amplitude at  $\lambda = \lambda_0$ , and  $\eta_\lambda$  is an additional power-law scaling parameter with wavelength to allow for a more flexible nonlinear (with frequency) relation.  $\lambda_i$  and  $\lambda_j$  are the effective wavelengths for observations at times  $t_i$  and  $t_j$ , respectively. Note for this kernel that we are ignoring the chromatic effects of limb-darkening and convective blueshifts on the RVs, which will impact the covariance matrix; however, given the flexibility of the GPs, Cale et al. (2021) found this chromatic kernel effectively recovers the wavelength dependence of stellar activity induced RV variations. For both Equations (3) and (4), the expression within square brackets is identical to that in Equation (2).

We apply Kernels  $J_1$  and  $J_2$  to our RV data, using the priors in Table 6, the priors from our FF’ analysis in Section 3.2.3 for the model hyperparameters, as well as a set of disjoint quasiperiodic kernels as in Equation (1), one GP for each spectrograph akin to RadVel (Fulton et al. 2018). In the analysis presented herein, we fix  $\eta_\ell$  and  $\eta_\tau$  to the median values from the SuperWASP light-curve analysis posteriors; letting these model hyperparameters vary in our RV analysis—with prior minimums of 0.2 and 20 days, respectively—yields quantitatively identical results for the median posterior values for  $K_b$  and  $K_c$ , albeit with slightly larger confidence intervals.

<sup>78</sup> Truly simultaneous measurements with identical midpoint exposure times, i.e.,  $t_i = t_j$ , would necessitate a more sophisticated indexing set.

Table 7

EXOFASTv2 Planetary Parameters: Median Values and 68% Confidence Interval Created for TOI 560 b and c, EXOFASTv2 Commit Number 101011575.2p.2

Planetary Parameter	Units	Planet b	Planet c
$P$	Period (days)	$6.3980661^{+0.000095}_{-0.000097}$	$18.8805^{+0.0024}_{-0.0011}$
$R_P$	Radius ( $R_J$ )	$0.253^{+0.014}_{-0.011}$	$0.2433^{+0.011}_{-0.0096}$
$R_P$	Radius ( $R_{Nep}$ )	$0.74^{+0.04}_{-0.03}$	$0.71^{+0.03}_{-0.03}$
$R_P$	Radius ( $R_{\oplus}$ )	$2.84^{+0.16}_{-0.12}$	$2.73^{+0.12}_{-0.11}$
$T_c$	Time of conjunction <sup>a</sup> (BJD <sub>TDB</sub> )	$2458517.68971^{+0.00053}_{-0.00054}$	$2458533.593^{+0.041}_{-0.091}$
$T_T$	Time of minimum projected separation <sup>b</sup> (BJD <sub>TDB</sub> )	$2458517.68973^{+0.00053}_{-0.00054}$	$2458533.593^{+0.041}_{-0.091}$
$T_0$	Optimal conjunction Time <sup>c</sup> (BJD <sub>TDB</sub> )	$2458703.23362^{+0.00044}_{-0.00045}$	$2459251.0510^{+0.0016}_{-0.0014}$
$a$	Semimajor axis (AU)	$0.05995^{+0.00074}_{-0.00072}$	$0.1233 \pm 0.0015$
$i$	Inclination (degrees)	$89.45^{+0.38}_{-0.50}$	$89.61^{+0.26}_{-0.24}$
$e$	Eccentricity	$0.294^{+0.13}_{-0.062}$	$0.093^{+0.13}_{-0.066}$
$\omega_*$	Argument of Periastron (degrees)	$130^{+30}_{-46}$	$-190 \pm 130$
$T_{eq}$	Equilibrium temperature <sup>d</sup> (K)	$742.7^{+7.2}_{-7.0}$	$517.8^{+5}_{-4.9}$
$\tau_{cir}$	Tidal circularization timescale (Gyr)	$44^{+69}_{-36}$	$9500^{+15000}_{-7100}$
$K$	RV semiamplitude ( $m s^{-1}$ ) <sup>e</sup>	$2.9^{+2.7}_{-1.9}$	$1.5^{+1.9}_{-1.1}$
$R_P/R_*$	Radius of planet in stellar radii	$0.03803^{+0.00063}_{-0.00064}$	$0.0379 \pm 0.0011$
$a/R_*$	Semimajor axis in stellar radii	$19.03^{+0.51}_{-0.48}$	$39.15^{+1.0}_{-0.99}$
$\delta$	$(R_P/R_*)^2$	$0.001446 \pm 0.000048$	$.001433^{+0.000086}_{-0.000082}$
$\delta_B$	Transit depth in B (fraction)	$0.00192^{+0.00059}_{-0.00032}$	$0.00186^{+0.00056}_{-0.00029}$
$\delta_R$	Transit depth in R (fraction)	$0.00216^{+0.00080}_{-0.00047}$	$0.00208^{+0.00076}_{-0.00043}$
$\delta_{z'}$	Transit depth in z' (fraction)	$0.00202^{+0.00085}_{-0.00041}$	$0.00195^{+0.00081}_{-0.00036}$
$\delta_{4.5\mu m}$	Transit depth in 4.5 $\mu m$ (fraction)	$0.0046^{+0.0023}_{-0.0012}$	$0.0042^{+0.0023}_{-0.0012}$
$\delta_{TESS}$	Transit depth in TESS (fraction)	$0.00163^{+0.00021}_{-0.00013}$	$0.0042^{+0.0023}_{-0.0012}$
$\tau$	Ingress/egress transit duration (days)	$0.003232^{+0.00020}_{-0.000078}$	$0.00588^{+0.00098}_{-0.00040}$
$T_{14}$	Total transit duration (days)	$0.0866 \pm 0.0014$	$0.1510^{+0.0039}_{-0.0032}$
$T_{FWHM}$	FWHM transit duration (days)	$0.0833^{+0.0014}_{-0.0013}$	$0.1448^{+0.0038}_{-0.0031}$
$b$	Transit impact parameter	$0.134^{+0.13}_{-0.093}$	$0.26^{+0.18}_{-0.17}$
$b_s$	Eclipse impact parameter	$0.19^{+0.18}_{-0.13}$	$0.26^{+0.13}_{-0.17}$
$T_s$	Ingress/egress eclipse duration (days)	$0.00500^{+0.00049}_{-0.00066}$	$0.00597^{+0.00047}_{-0.00046}$
$T_{s,14}$	Total eclipse duration (days)	$0.127^{+0.012}_{-0.017}$	$0.152^{+0.013}_{-0.015}$
$T_{s,FWHM}$	FWHM eclipse duration (days)	$0.122^{+0.012}_{-0.016}$	$0.147^{+0.012}_{-0.015}$
$T_{s,2.5\mu m}$	Blackbody eclipse depth at 2.5 $\mu m$ (ppm)	$1.57^{+0.12}_{-0.11}$	$0.0537^{+0.0065}_{-0.0059}$
$T_{s,5.0\mu m}$	Blackbody eclipse depth at 5.0 $\mu m$ (ppm)	$26.8^{+1.3}_{-1.2}$	$4.85^{+0.39}_{-0.36}$
$T_{s,7.5\mu m}$	Blackbody eclipse depth at 7.5 $\mu m$	$61.4^{+2.7}_{-2.5}$	$18.8^{+1.3}_{-1.2}$
$\langle F \rangle$	Incident flux ( $10^9 \text{ erg s}^{-1} \text{ m}^{-2}$ )	$0.0629^{+0.0034}_{-0.0054}$	$0.01600^{+0.00071}_{-0.00078}$
$T_P$	Time of periastron (BJD <sub>TDB</sub> )	$2458511.67^{+0.15}_{-0.43}$	$2458517.0^{+4.0}_{-5.8}$
$T_S$	Time of eclipse (BJD <sub>TDB</sub> )	$2458520.15^{+0.83}_{-0.85}$	$2458524.1^{+1.3}_{-1.7}$
$T_A$	Time of ascending node (BJD <sub>TDB</sub> )	$2458516.27^{+0.32}_{-0.49}$	$2458528.85^{+0.70}_{-1.0}$
$T_D$	Time of descending node (BJD <sub>TDB</sub> )	$2458512.20^{+0.27}_{-0.25}$	$2458538.22 \pm 0.80$
$V_c/V_e$	Equivalent circular to measured eccentric velocity ratio	$0.791^{+0.029}_{-0.027}$	$0.991^{+0.061}_{-0.048}$
$e \cos \omega_*$	Eccentricity times cosine of the periastron angle	$-0.18^{+0.20}_{-0.22}$	$-0.004^{+0.11}_{-0.14}$
$e \sin \omega_*$	Eccentricity times sine of the periastron angle	$0.199^{+0.043}_{-0.069}$	$-0.003^{+0.047}_{-0.066}$
$d/R_*$	Separation at mid-transit	$14.2^{+1.1}_{-1.2}$	$38.6 \pm 2.7$
$P_T$	A priori nongrazing transit prob	$0.0676^{+0.0061}_{-0.0048}$	$0.0249^{+0.0018}_{-0.0016}$
$P_{T,G}$	A priori transit prob	$0.0730^{+0.0066}_{-0.0051}$	$0.0269^{+0.0020}_{-0.0017}$
$P_S$	A priori nongrazing eclipse prob	$0.0437^{+0.093}_{-0.0024}$	$0.0247^{+0.0025}_{-0.0011}$
$P_{S,G}$	A priori eclipse prob	$0.0472^{+0.010}_{-0.0026}$	$0.0267^{+0.0027}_{-0.0012}$

**Notes.** See Table 3 in Eastman et al. (2019) for a detailed description of all parameters.

<sup>a</sup> Time of conjunction is commonly reported as the “transit time.”

<sup>b</sup> Time of minimum projected separation is a more correct “transit time.”

<sup>c</sup> Optimal time of conjunction minimizes the covariance between TC and period.

<sup>d</sup> Assumes no albedo and perfect redistribution.

<sup>e</sup> The recovered semiamplitudes for the planets in the EXOFASTv2 analysis are significantly smaller than the those recovered in Table 6 with our RV analysis that includes a stellar activity model, and thus would appear at first to be contradictory. However, they are not statistically significant detections in this EXOFASTv2 analysis, as the posteriors are peaked at 0  $m s^{-1}$ , and the reported confidence intervals herein are consequently misleading. The corresponding 5 $\sigma$  upper limits are  $\sim 15$  and 10  $m s^{-1}$  for  $K_b$  and  $K_c$ , respectively.

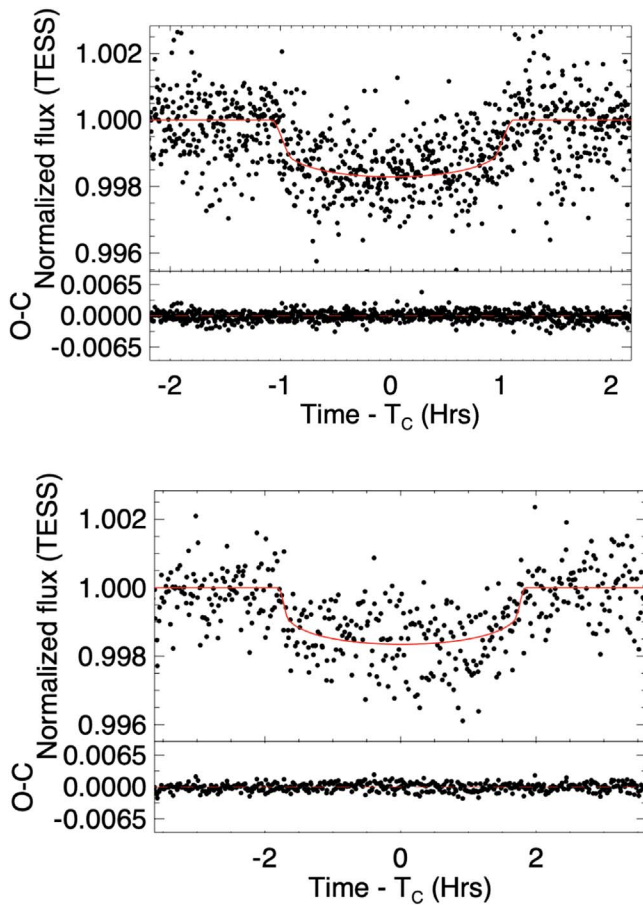


**Figure 14.** TOI 560 b (top) and TOI 560 c (bottom) TESS phase-folded transit light curves, plotted as normalized flux as a function of time since transit conjunction in hours on the horizontal axis. The median MCMC transit models are overlaid as red lines. The bottom panel show the median-model subtracted residuals.

We also analyze the RVs using no GP, effectively assuming the stellar activity is not present.

## 4. Results

In Section 4.1, we present the transit analyses of the TESS, Spitzer, and ground-based light curves using EXOFASTv2. Then in Section 4.2 we present the RV analysis with `pychell` and the GP stellar activity model.

### 4.1. Transit Light Curves

In this subsection we represent the results of our EXOFASTv2 analysis of the light curves and vetting results.

#### 4.1.1. TESS Light Curves

The TOI 560 TESS light curves for Sectors 8 and 34 are shown in Figure 13, after subtracting off a cubic-spline regression fit for the out-of-transit stellar activity from the PDC-SAP light curves shown in Figure 10. The EXOFASTv2 analysis reveals clear transits of TOI 560 b and c with expected depths and transit times consistent with the TESS mission TOI 560 b and 560.02 candidates. Table 7 shows the median and confidence intervals for the model and derived planetary parameters. Figure 14 shows the phased TESS transits. Of particular note, we confirm a nonzero eccentricity for TOI 560 b at  $4.7\sigma$ ; the eccentricity

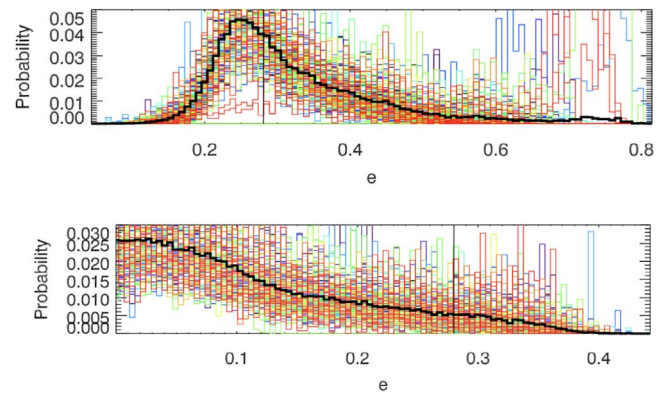


**Figure 15.** Eccentricity posteriors for TOI 560 b and c from our EXOFASTv2 results. The eccentricity values are on the horizontal axis, and the normalized probabilities are on the vertical axis. The colored histograms show individual MCMC walker chains, with the black histogram showing the medians of all walkers. The posterior for TOI 560 b slightly favors a mild eccentricity, whereas for TOI 560 c, a circular orbit is preferred.

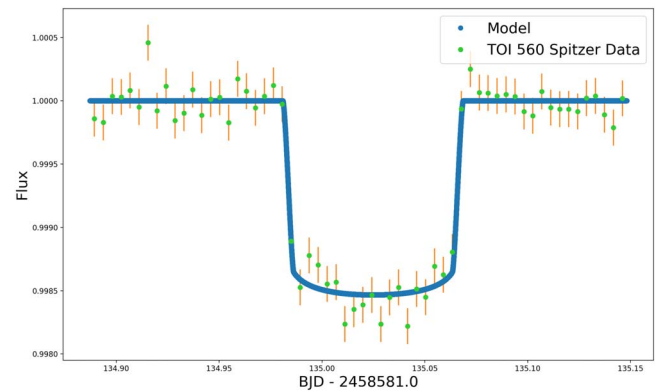


**Figure 16.** The Spitzer light curve for TOI 560, with normalized flux plotted as a function of time since mid-transit. The Spitzer data points are binned for clarity, and overlaid with a transit model independently fit in blue.

posterior for TOI 560 c is consistent with zero (Figure 15). The statistical significance of the nonzero eccentricity detection for TOI 560 b is primarily driven by the photoeccentric effect using the Spitzer data (Dawson & Johnson 2012), as excluding this particular data set decreases the statistical significance on  $e_b > 0$  to  $1.6\sigma$ , but still with a similar nonzero median eccentricity. Finally, the Spitzer light curve is presented in Section 4.1.2, and ground-based PEST, NGTS, and LCO light curves are presented in Figures 26–28 in Appendix C.

#### 4.1.2. Spitzer Light Curve

The Spitzer light curve (Figure 16) shows a transit that is consistent with the expected timing, duration, and depth from TESS for TOI 560 b. This helps rule out false-positive eclipsing binary scenarios due to the lack of any observed chromaticity in the depth and shape of the observed transit. Additionally, the Spitzer light curve is at higher photometric precision and temporal sampling with respect to TESS given the larger aperture of Spitzer; there is less limb-darkening compared to visible wavelengths, and less photometric variations due to stellar activity. Therefore, these observations help further constrain the exoplanet parameters of TOI 560 b and refine the orbital ephemerides. In particular, the Spitzer light curve enables us to detect the eccentricity of TOI 560 b via the photoeccentric effect

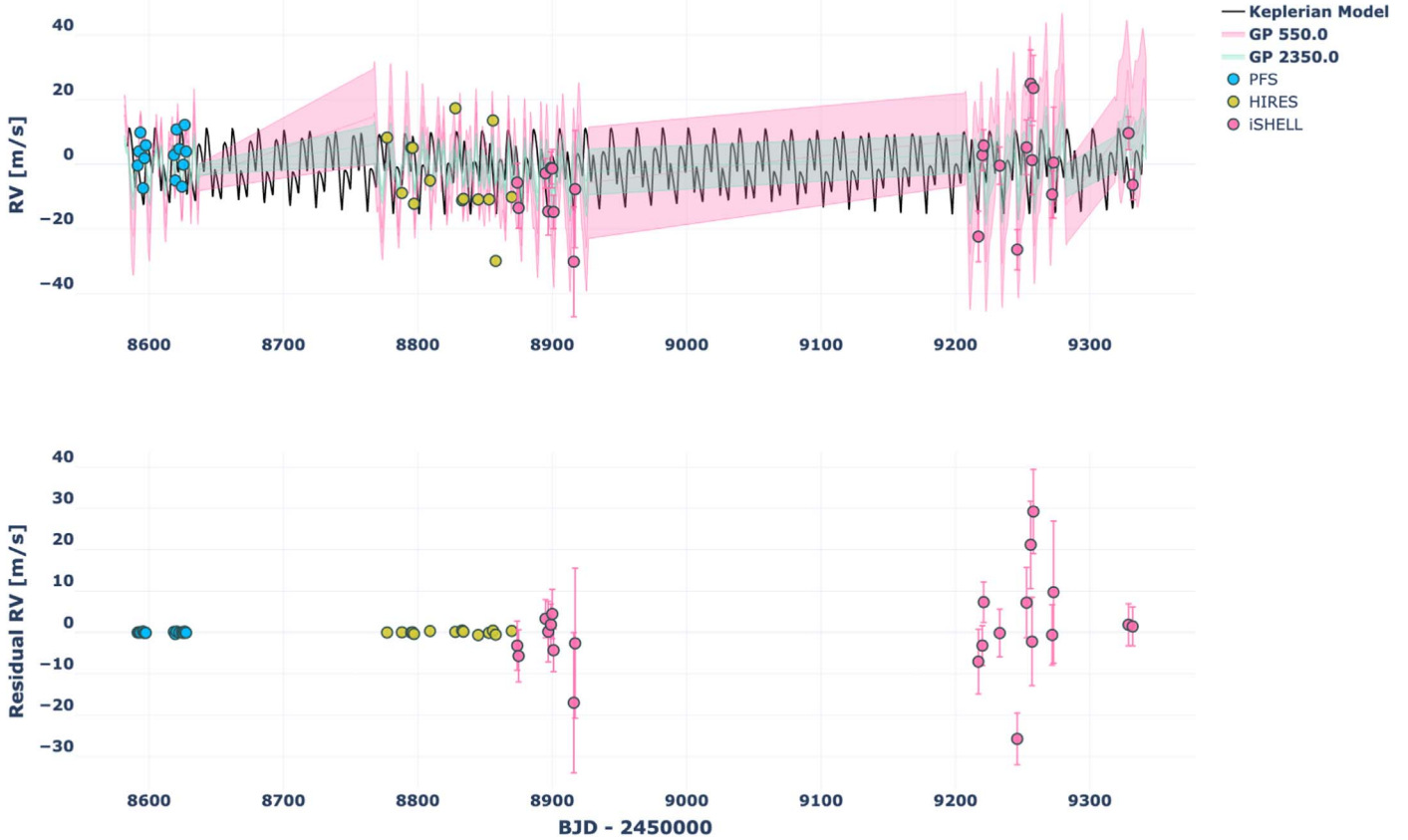


**Figure 17.** Full RV time-series plot for the joint chromatic GP kernel  $J_2$  model, with time in BJD on the horizontal axis and RV on the vertical axis in meters per second. RV measurements are shown as colored circles for each RV spectrograph. The black solid line is the Keplerian best-fit MAP model for TOIs 560 b and c. The shaded regions are the chromatic GP  $1\sigma$  uncertainty regions from realizations of the  $J_2$  covariance kernel, with the PFS and HIRES sharing the same GP at 550 nm, and a marginally smaller GP amplitude in the NIR for iSHELL. Residuals (data – model) are shown in the lower plot.

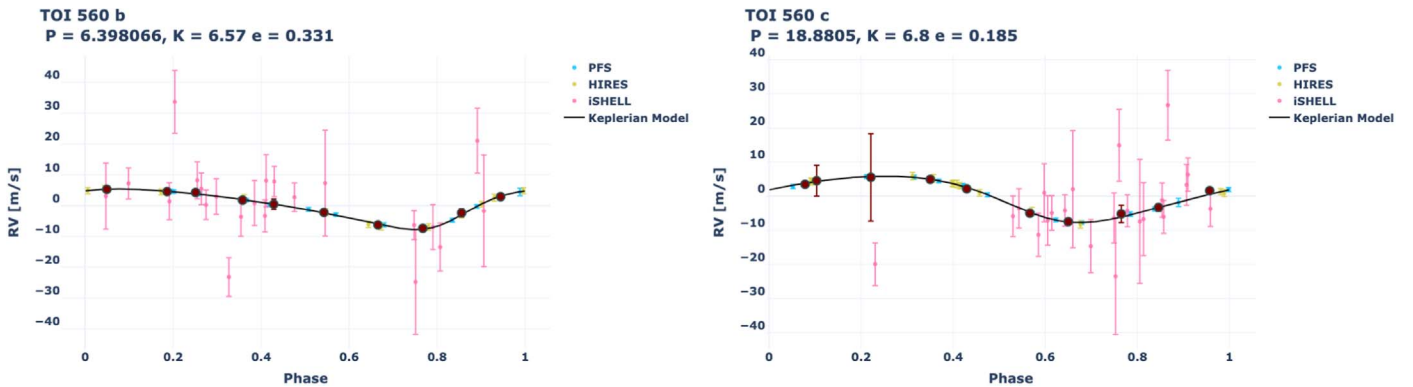


**Figure 18.** Phased RV time-series plot for the joint chromatic GP kernel  $J_2$  model, with orbital phase on the horizontal axis and RV on the vertical axis in meters per second. The left panel is phased to TOI 560 b, and the right panel TOI 560 c. RV measurements, after subtracting the best-fit GP are shown as small colored circles for each RV spectrograph. The maroon points are binned RVs every 0.1 in orbital phase. The best-fit MAP Keplerian model is shown as the black curve, with a fixed circular orbit, velocity semi-amplitude  $K$ , and orbital period  $P$  indicated.

as deviating from zero at  $4.7\sigma$ . This eccentricity is marginally detected in the TESS transits, but is not statistically significant without the Spitzer observations.

#### 4.2. RV *pychell* Results

Using our RV model with *pychell*, we produce consistent and stable MCMC results for all GP kernels considered that provide detections for the masses of TOI 560 b and c, establishing their nature as a pair of Neptune-mass exoplanets consistent with their radii (Table 6). For our adopted final result

using the  $J_2$  kernel, the RV models with MAP values and MCMC cornerplot are shown in Figures 17, 18, and 19. The best MAP fit, and MCMC median and confidence intervals are presented in Table 6. The table of exoplanet mass and density measurements derived from our RV analysis are given in Table 8. In Appendix B, in Figure 25, we present the mass–radius diagram for known transiting exoplanets with measured masses (Akeson et al. 2013), with the detections for TOI 560 b and c shown to be consistent with the older Neptune-mass regime.

We present in Appendix D the results of the RV analyses for the  $J_1$  joint GP kernel (Figures 32–34), the disjoint

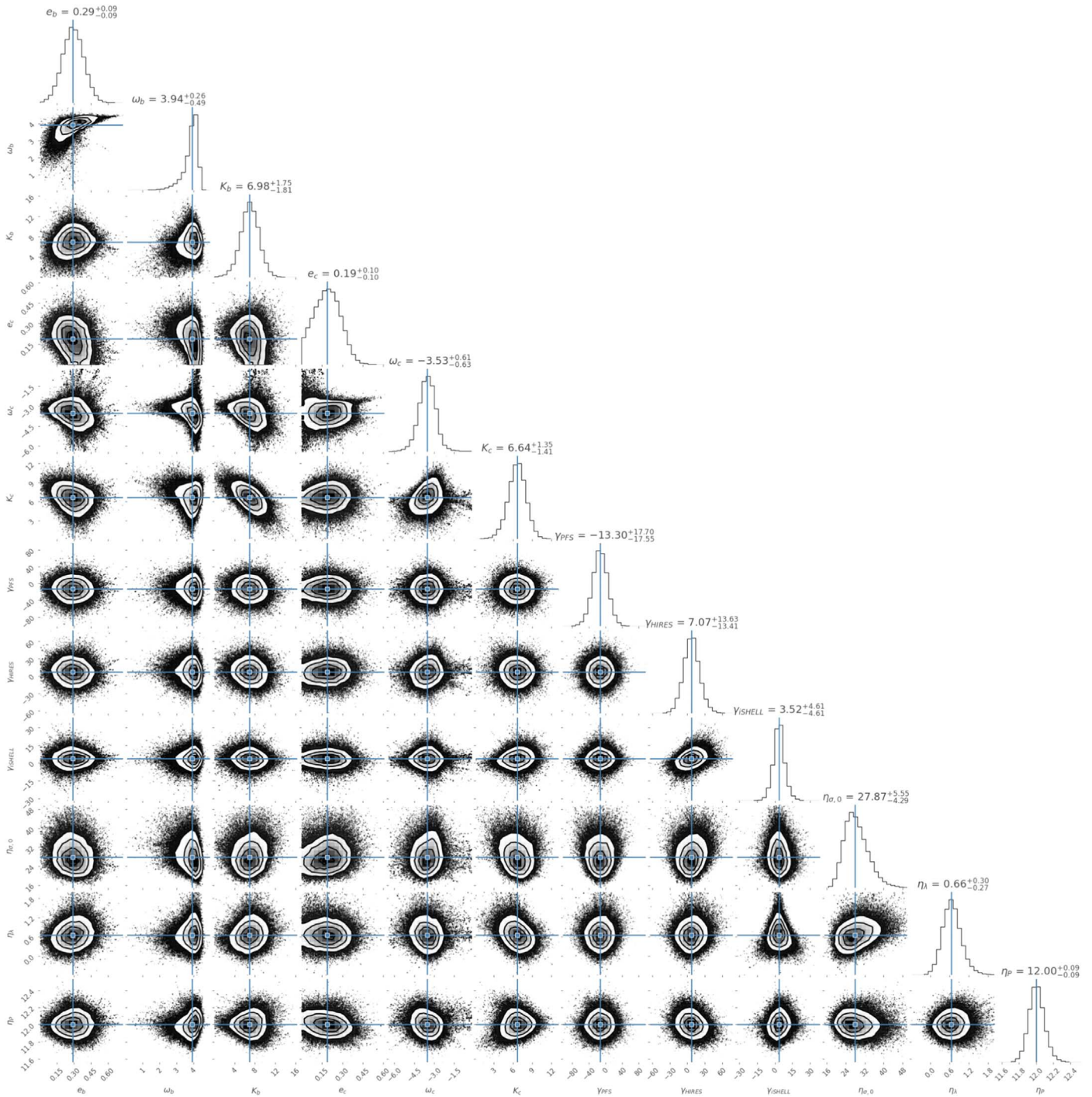


**Figure 19.** MCMC cornerplot for our joint chromatic GP kernel  $J_2$  RV model. Posterior distributions are along the diagonal, and two-parameter covariances are shown off the diagonal. The model parameter median and 68% confidence interval ranges are displayed at the top of each posterior distribution; median values are also indicated with horizontal and vertical blue lines for the covariance plots, and vertical lines for the posterior distribution. For the covariance plots,  $1\sigma$ ,  $2\sigma$ , and  $3\sigma$  contours are shown in place of the individual sample values  $<3\sigma$  from the medians.

“classic” quasiperiod GP kernel where there is a separate GP for every spectrograph (Figures 35–37), and for the RV analysis with no stellar activity assumed in Tables 13 and 14, respectively (Figures 29–31). All yield similar detections or upper limits to the exoplanet velocity semi-amplitudes and consistent model hyperparameters for the stellar activity.

A model comparison in Table 9 shows that the RVs support the detection of both planets b and c combined and also planets

b and c individually. The one- and two-planet models are statistically indistinguishable. The no-planet scenario is ruled out. Additionally, we do recover  $3.8\sigma$  ( $4.7\sigma$ ) detections of TOI 560 b (c) with our  $J_2$  kernel. For the other kernels presented in Appendices D and E, we find qualitatively similar marginal and  $>3\sigma$  recoveries of  $K_b$  and/or  $K_c$ . Our  $J_2$  kernel model estimates the masses of planets b and c to be  $0.94^{+0.31}_{-0.23}M_{\text{Nep}}$  and  $1.32^{+0.29}_{-0.32}M_{\text{Nep}}$ .

**Table 8**Mass and Density Detections from Our Joint Chromatic  $J_2$  GP Kernel RV Model

Planet	Mass	Density ( $\text{g cm}^{-3}$ )
b	$15.9^{+5.3}_{-3.9} M_{\oplus}$ , $0.94^{+0.31}_{-0.23} M_{\text{Nep}}$	$3.8^{+1.4}_{-1.1}$
c	$22.5^{+5.0}_{-5.5} M_{\oplus}$ , $1.32^{+0.29}_{-0.32} M_{\text{Nep}}$	$6.1^{+1.6}_{-1.7}$

**Table 9**Model Comparison Test for Planets b and c Generated through the Joint  $J_2$  Kernel Model, Which Support the Detection of At Least One Planet, b or c Individually, or Both Planets with Indistinguishable AICc Values

Planets	$\ln \mathcal{L}$	$\Delta \text{AICc}$	$\Delta \text{BIC}$	N free	$\chi^2_{\text{red}}$
b, c	-197.0	0.0	1.5	12	1.1
b	-202.1	0.3	0.0	9	0.9
c	-204.5	5.1	4.7	9	0.9
None	-233.9	55.3	51.7	6	1.4

**Note.** The no-planet scenario is ruled out.

## 5. Discussion

In the previous sections, we validated the presence of a two-planet system orbiting a young,  $\sim 600$  Myr host star TOI 560, detected the individual planet masses at  $>3\sigma$ , establishing the planets as Neptune analogs. In this discussion, in Section 5.1, we present a dynamical stability analysis of the system, which appears stable over the 10 Myr timescale explored. Next we consider the near 1:3 orbital resonance of TOI 560 b and c, and what implications that may have for additional planets and formation in Section 5.3. Finally, in Section 5.4 we discuss the suitability of the TOI 560 system for future atmospheric characterization.

### 5.1. Dynamical Stability: Two-planet REBOUND Simulation

We perform dynamical stability tests of the TOI 560 system over a duration of 10 Myr using REBOUND, an  $N$ -body gravitational integrator built in C and usable in python (Rein & Liu 2012; Rein & Spiegel 2015). To define each orbit, we use the  $P$ ,  $T_p$ , eccentricity, and inclination median values from our EXOFASTv2 MCMC analysis in Table 7, and we use the median planet masses  $M_p$  from our  $J_2$  kernel model values from Table 8. We choose an integration time step shorter than 1/20th of the shortest orbital period ( $dt = 0.32$  days). The results of this dynamical simulation are shown in Figures 20 and 21. The simulations show the dynamical interactions between TOI 560 b and c, with a mean-motion resonant libration precession of the longitudes of periastron. This demonstrates that the detected eccentricity for TOI 560 b could be a consequence of the dynamical interaction with TOI 560 c. The orbits of both planets are stable and possessing moderate eccentricities over the entire 10 Myr simulation duration. We did not run the simulation to  $\sim 1$  Gyr, the estimated lifetime of the system, because of the near 1:3 orbital resonance; a mean-motion orbital resonance can either stabilize or destabilize the system within a timescale of a few hundred orbits, so if the system was unstable, the instability would have been apparent in the simulation well within a few megayears.

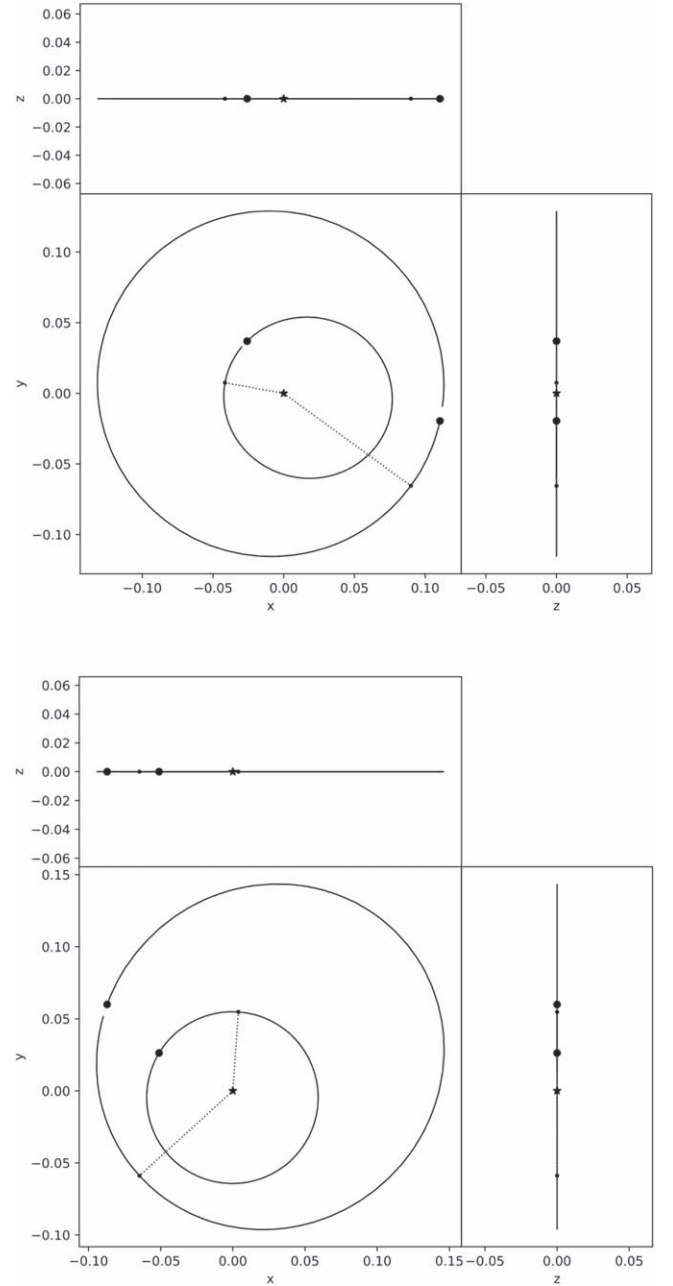


**Figure 20.** Overhead and edge-on diagrams showing the initial (top) and final (bottom) orbital configurations of our two-planet model in REBOUND with inclination estimated from EXOFASTv2. The  $x$ -,  $y$ -, and  $z$ -axes are in astronomical unit. The planet positions are noted as black dots, and the orbits as circles. The periastron vectors are marked with dashed lines starting from the star (star symbol) at the origin of the orbits, and show significant evolution from the start to the beginning of the simulation.

### 5.2. The Search for Additional Candidates

Fourier-like periodograms can be useful in determining prominent frequencies in unevenly sampled RV time-series. First, we calculate generalized Lomb-Scargle (GLS; Scargle 1982; Zechmeister & Kurster 2009) periodograms. The GLS periodogram power at a given trial period directly correlates with the Keplerian velocity semiamplitude of a circular-orbit planet signal at that trial period. Multiple periodic signals are identified by subtracting a best-fit periodic signal from the data, and then repeating the periodogram calculation

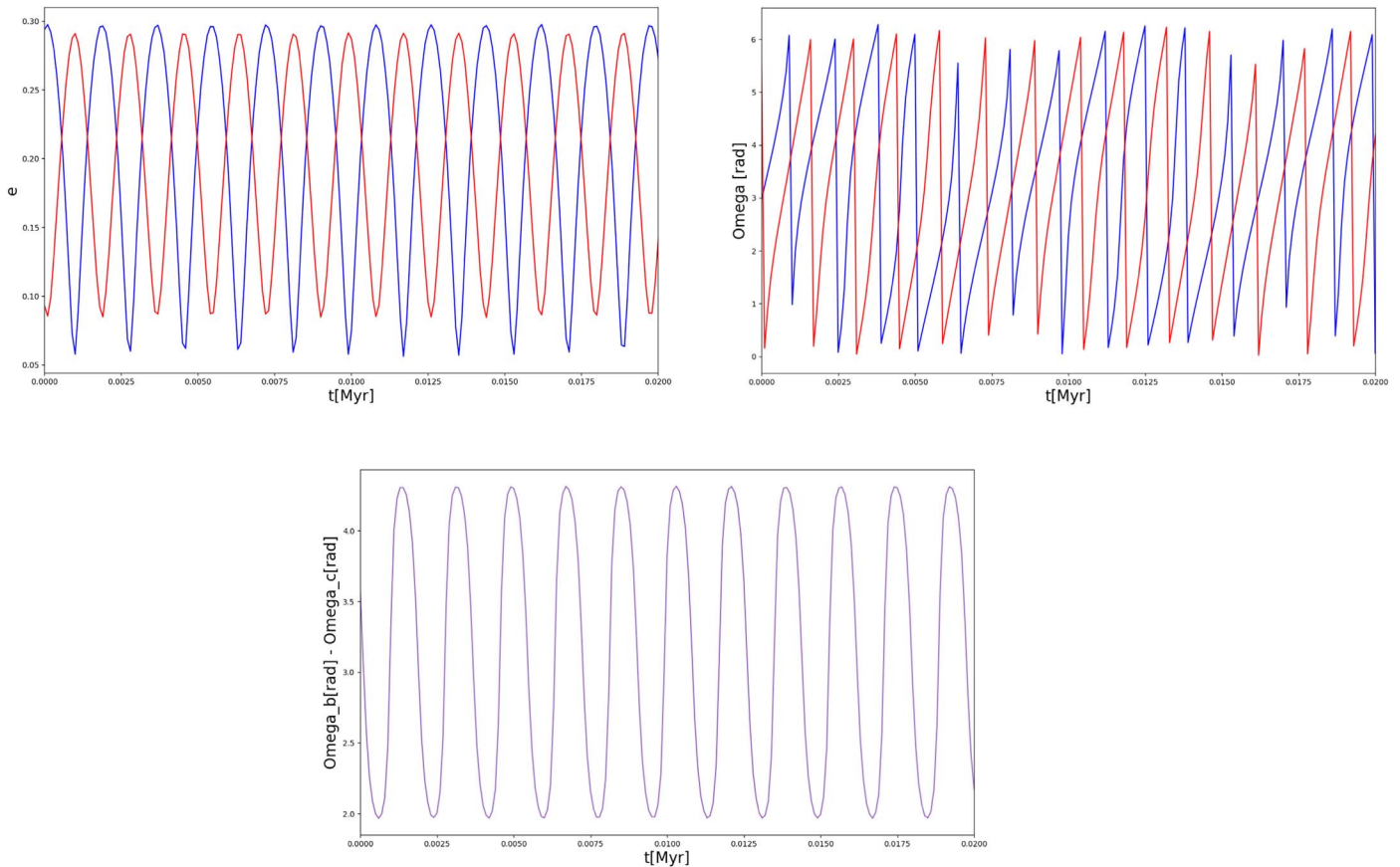


**Figure 21.** REBOUND simulations showing the evolution of the orbital elements of TOI 560 b (blue) and c (red). The semimajor axis evolution is stable (not shown), and the planets are assumed coplanar so there is no inclination variation (not shown). The first panel shows the significant temporal evolution of the eccentricities for TOI 560 b and c, consistent with the moderate eccentricity we detect for TOI 560 b. The second panel shows the longitudes of periastron (in degrees) on the vertical axes as a function of time on the horizontal axes, showing significant dynamical precession. The bottom panel shows the difference in the longitudes of periastron between the two planets, showing that the system exhibits a libration in the longitudes of periastron. Only the first 20,000 yr of orbital evolution are shown, but the system behaves similarly for the duration of the 10 Myr simulation.

on the residuals; this process is repeated until no more statistically significant signals are identified.

For TOI 560 in particular, we compute a GLS periodogram utilizing a stellar activity + two-planet model for b and c. We first remove the nominal GP and zero-points; this periodogram is used to see if we can identify the RV signal of b or c, or any additional planet(s) present in the system as a periodogram peak. Then we further remove the best-fit RV signal for TOI 560 b, and recompute the periodogram; this periodogram is used to see if we can identify the RV signal of TOI 560 c or any additional planet(s) present in the system. Third, we subtract off the best-fit model for planet c, and recompute the periodogram of the residuals; this periodogram is used to search for any additional planets in the system. In all cases, the orbital period and time of conjunction and thus orbital phase of either TOI 560 b and/or c are fixed in fitting the planet signals to the RV time-series data, and only the velocity semiamplitude, eccentricity, and angle of periastron are free (fitted) parameters. We calculate false-alarm probabilities (FAPs) using both the standard analytic formula derived from the periodogram power (Scargle 1982; Zechmeister & Kurster 2009), and empirically through a 1000-trial bootstrap process of: scrambling (re-ordering) the times of observations while holding the ordering of the RV values fixed (or conversely, scrambling the ordering of the RV values while holding the ordering of the times of observations fixed), then

recomputing the periodogram, and then investigating the empirical distribution of the top power values. While GLS periodograms have historically been successful in identifying genuine multiplanet signals in RV time-series data, this approach is also fraught with the identification of false-positive signals because of the overly simplistic assumptions (e.g., Robertson et al. 2014, 2015); it can be difficult to discern whether GLS periodogram peaks are real planet signals, or some form of systematic red noise (e.g., a cadence alias, imperfect signal subtraction in the iterated residuals, or stellar rotational modulation of activity; Dawson & Fabrycky 2010; Vanderburg et al. 2016). We also compute the window function of the RV time-series by setting all RV values equal to zero and computing a Lomb-Scargle periodogram to identify any periodogram peaks that are associated with temporal sampling cadence aliases, such as integer fraction multiples of 1 day or 1 yr.

Second, Bayesian model-based  $\ln \mathcal{L}$  periodograms enable statistically robust comparisons that jointly capture the full model complexity of potentially multiplanet systems with models for stellar activity embedded in the noisy, unevenly sampled RVs (e.g., Tuomi et al. 2014; Anglada-Escude et al. 2016). First, we compute a maximum-likelihood fit to the RVs for a model with stellar activity and a first “trial” planet of unknown phase and velocity semiamplitude at a trial orbital period. We follow the same implementation as in

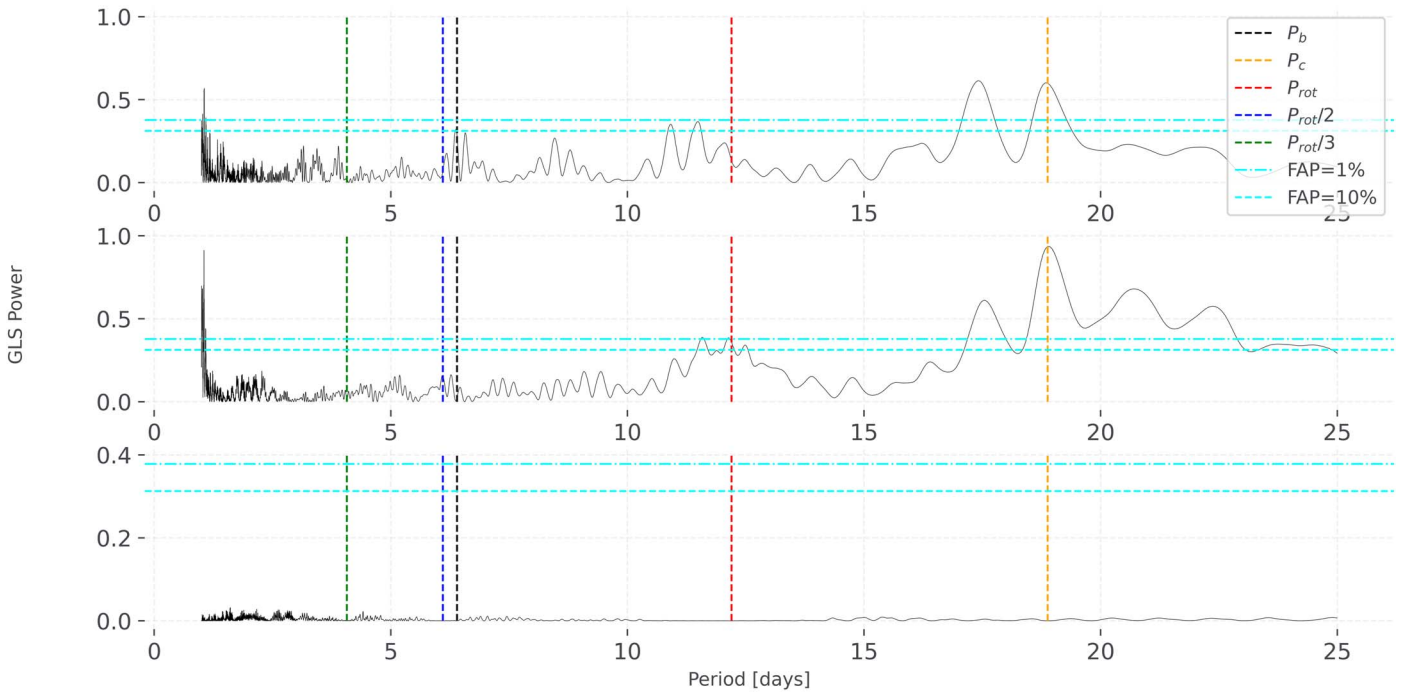


**Figure 22.** A series of GLS periodograms examining the signals in our TOI 560 RV time-series as described in the text including iSHELL, HIRES, and PFS. The top panel is a periodogram of the RVs after subtracting a stellar activity model fit. The middle panel additionally subtracts a model fit for TOI 560 b and stellar activity to search for a second planet, and the bottom panel subtracts a model fit for both TOI 560 b and c and stellar activity to search for a third planet. The periods of b and c are marked with dashed black and orange vertical lines and also the rotation period, one-half of it, and one-third of it are marked with dashed red, blue, and green vertical lines, respectively, in each panel. The bootstrap FAPs of 1% and 10% were marked with cyan horizontal dashed lines. Note, it remains challenging to find nontransiting RV planets at orbital periods near the stellar-rotation period or one of its prominent integer fraction aliases (e.g., 1/2, 1/3), as the GP stellar activity model could potentially “absorb” such a Keplerian signature (Vanderburg et al. 2016; Kossakowski et al. 2022).

Cale et al. (2021). We compute this one-planet model  $\ln \mathcal{L}$  over a set of trial periods to generate the first  $\ln \mathcal{L}$  periodogram, which is used to see if we can identify the RV signal of b or c, or any additional planet present in the system as a periodogram peak. Second, we add to our model a planet at the orbital period and time of conjunction of TOI 560 b, in addition to the trial planet. We compute maximum-likelihood fits to this two-planet model over the same set of trial periods to compute the second  $\ln \mathcal{L}$  periodogram, which is used to see if we can identify the RV signal of TOI 560 c, or any additional planet present in the system as a periodogram peak. Third, we add to our model a third planet at the orbital period and time of conjunction of TOI 560 c to see if we can identify the RV signal for any additional planet present in the system besides TOI 560 b or c.

The GLS periodograms are shown in Figure 22, and the  $\ln \mathcal{L}$  periodograms are shown in Figure 23. We find two  $\ln \mathcal{L}$  periodogram peaks that are persistent with a  $\Delta \ln \mathcal{L} > 15$  at 4.57 and 5.54 days, particularly for the periodograms where TOI 560 b is included in the model. The 5.54 day period would likely not be dynamically stable with the TOI 560 b at 6.40 days. However, the 4.57 periodogram peak suggests a possible nontransiting candidate that would be near a 2:3 orbital resonance with TOI 560 b. This period is also not near an alias of the stellar-rotation period. Furthermore, the 5.54 day peak is close to the frequency difference between the 4.57 day peak and the cadence alias of 5 days and is thus potentially a cadence alias of the 4.57 day peak. Consequently, we perform a model comparison with a third nontransiting interior planet at this orbital period of 4.57 days. However, the model comparison disfavors the detection of this planet. Thus, our existing data is

insufficient to confirm the possibility of an additional nontransiting candidate planet in this system.

### 5.3. Implication of the Near 1:3 Orbital Period Resonance of TOI 560 b and c

Given the youth of TOI 560, neither planet would have been tidally circularized by the star if they started with an initial high-eccentricity formation mechanism (Rasio et al. 1996; Bodenheimer et al. 2003). Our RVs are not sufficient to constrain the eccentricities of either planet, given that we have only a marginal mass detection of TOI 560 b and a nondetection of TOI 560 c, and also due to the presence of the stellar activity. However, our EXOFASTv2 analysis of the TESS Spitzer and ground transits of TOI 560 b confirms a moderate eccentricity of 0.29 (Figure 15). Both planets show that a high eccentricity is disfavored. This implies that TOI 560 b and c likely did not form in a high-eccentricity migration scenario, and more likely formed in situ, unless the migration took place when a significant gas disk was still present to dampen the orbital eccentricities (Lin et al. 1996; Ward 1997; Plavchan & Bilinski 2013). The orbital eccentricity of TOI 560 b will be an important parameter to further constrain with future observations, such as may be possible with secondary eclipse observations and additional high-precision RVs.

The orbital period near-commensurability of TOI 560 b and c to a 1:3 ratio also has interesting implications for planet formation. For one, such an orbital resonance is rare among mature exoplanet systems identified by Kepler (Figure 4 in Fabrycky et al. 2014). Far more common among mature compact multiexoplanet systems are the 2:3 and 1:2 near-commensurability orbital period resonances. This raises the

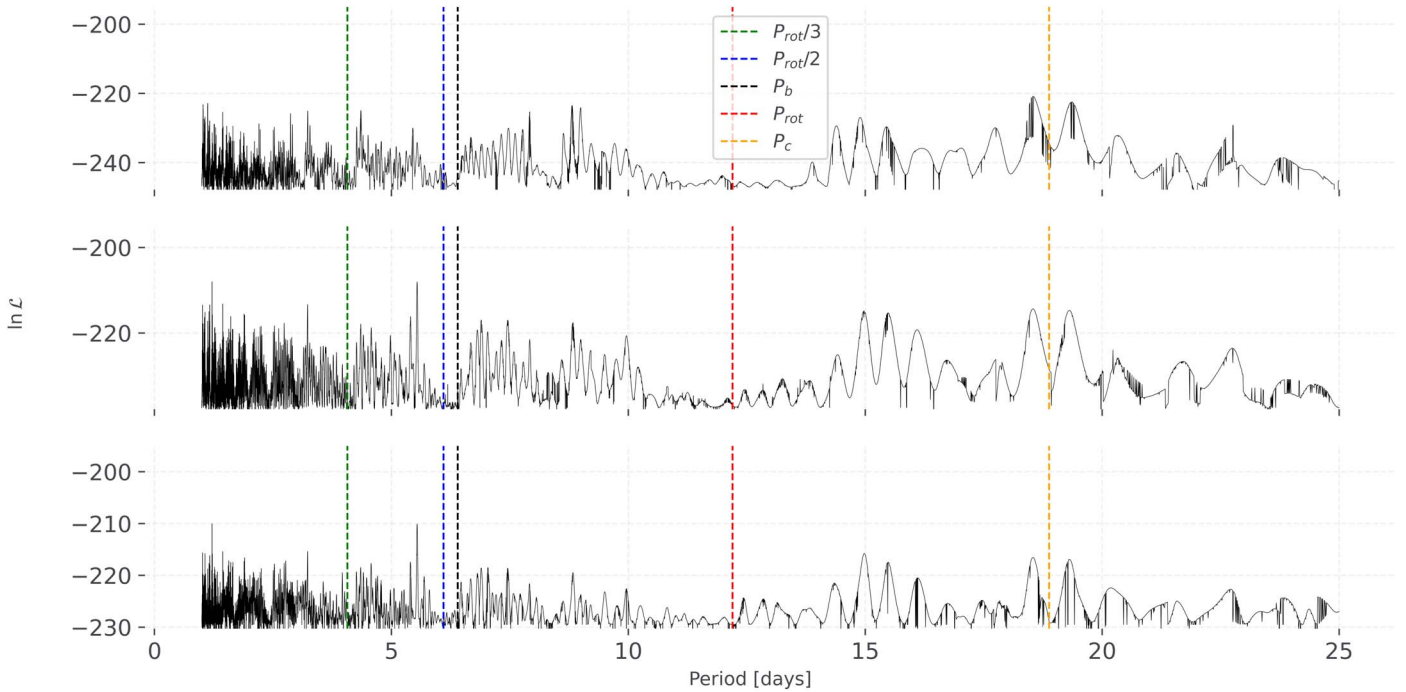


**Figure 23.** Similar to the previous figure, a series of  $\ln \mathcal{L}$  periodograms examining the signals in our TOI 560 RV time-series. All three panels depict a single, circular planet search with a floating TC. The top panel includes no extra planets, the middle panel models out TOI 560 b to search for a second planet, and the bottom panel models out both TOI 560 b and c to search for a second planet. The periods of b and c are marked with dashed black and orange vertical lines and also the rotation period, one-half of it, and one-third of it are marked with dashed red, blue, and green vertical lines, respectively, in each panel.

interesting possibility that there could be a third middle planet in the TOI 560 system that is nontransiting with an orbital period of  $\sim 12.6$  days that would establish the TOI 560 system in a 1:2:3 orbital resonant chain at an age of  $< 1.5$  Gyr. Such systems of transiting exoplanet systems orbiting mature stars with middle nontransiting companions are more common than perceived—e.g., Christiansen et al. (2017), Buchhave et al. (2016), Sun et al. (2019), and Osborn et al. (2021) identified similar exoplanet configurations for the HD 3167, Kepler-20, Kepler-411, and TOI-431 planetary systems, respectively.

The 22 Myr au Mic system is possibly also in a resonant 4:6:9 orbital chain with a middle nontransiting planet candidate (Cale et al. 2021; Wittrock et al. 2022), and the 20 Myr  $\nu$ 1298 Tau system is in a 2:3:6:10 resonant chain (David et al. 2019a; Feinstein et al. 2022b; Suárez Mascareño et al. 2021). Similarly, it is an interesting coincidence that TOI 560 b and c are near 1:2 and 2:3 orbital period resonant near-commensurability with the stellar-rotation period of TOI 560 of 12.2 days. It has recently been shown that AU Mic b is in a 4:7 orbital period commensurability with the rotation period of the AU Mic host star (Szabó et al. 2021). These period commensurabilities are perhaps coincidental. However, if indeed resonant chains are common for young exoplanet systems, and if there are further instances of stellar spin–planet orbital period commensurabilities found in the future for young exoplanet systems, this could have important implications for planet formation mechanisms. It will be important to conduct future Rossiter-McLaughlin observations of TOI 560 b and c to determine if their orbits are also aligned with the stellar spin axes, as is the case for AU Mic b and  $\nu$ 1298 Tau b (Hirano et al. 2020; Martioli et al. 2020; Palle et al. 2020; Addison et al. 2021b; Johnson et al. 2022; Gaidos et al. 2022). The expected amplitude for the R-M effect for TOI 560 b and c is  $\sim 4$   $\text{m s}^{-1}$ ,

calculated with a  $v \sin i = 2.8$   $\text{km s}^{-1}$  from the known rotation period of 12.2 days, and our  $R_p/R_*$  and  $R_*$  from our EXOFASTv2 analysis (Table 7), and assuming the stellar-rotation axis is in the planet of the sky, which is consistent with the observed constraints on  $v \sin i$  from TRES and NRES (Section 3.1.1).

Finally, we do investigate the dynamical stability of one test case of a middle, nontransiting planet for TOI 560—simulated with masses 9.2, 4.2, and 1  $M_{\oplus}$  for TOI 560 b, c and the hypothetical middle d at  $P = 12.6$  days, respectively. However, we find that this particular test case was not dynamically stable. Exploring the full dynamical stability of possible scenarios is beyond the scope of this work, but the mild eccentricity of TOI 560 b may preclude the dynamical stability of any middle planets. It would also be incredibly challenging to detect such a middle planet with RVs alone given that the rotation period of the star is 12.2 days; stellar activity will potentially hide any such RV signal given our current stellar activity modeling tools (Vanderburg et al. 2016).

#### 5.4. The Suitability for the TOI 560 Planets for Atmospheric Characterization

Finally, we evaluate the suitability of TOI 560 b and c for atmospheric characterization. We compute the transmission spectroscopy metrics (TSM) and emission spectroscopy metrics (ESM; Kempton et al. 2018) for a set of TOIs in Figure 24, including TOI 560 b and c of 151.9, 11.2 and 102.8, 3.4 for TSM and ESM, respectively:

$$\text{TSM} = (\text{Scale factor}) \times \frac{R_p^3 T_{\text{eq}}}{M_p R_*^2} \times 10^{-m_j/5} \quad (5)$$

**Table 10**  
Upcoming Transit Pairs of TOI 560 b and c Visible by JWST, with Midpoint Time Separations of <6 Hr

Planet	$T_c$ (JD-2460000)	$T_c$ (UT)	$\Delta T_c$ (hr)	$T'_1 - T_4$ (hr)
b	$251.5643 \pm 0.0047$	11/3/2023 01:33	...	...
c	$251.67 \pm 0.02$	11/3/2023 04:15	$2.71 \pm 0.50$	$-0.17 \pm 0.94$
c	$270.56 \pm 0.02$	11/22/2023 01:22	...	...
b	$270.7584 \pm 0.0047$	11/22/2023 06:12	$4.84 \pm 0.50$	$1.96 \pm 0.94$
b	$629.0054 \pm 0.0056$	11/14/2024 13:12	...	...
c	$629.20 \pm 0.02$	11/14/2024 18:32	$5.33 \pm 0.58$	$2.45 \pm 1.02$
c	$648.15 \pm 0.02$	12/3/2024 15:38	...	...
b	$648.2440 \pm 0.0056$	12/3/2024 17:51	$2.22 \pm 0.58$	$-0.66 \pm 1.02$
b	$1025.6710 \pm 0.0065$	12/16/2025 05:30	...	...
c	$1025.67 \pm 0.03$	12/16/2025 05:55	$0.41 \pm 0.66$	$-2.47 \pm 1.10$
b	$1403.2150 \pm 0.0073$	12/28/2026 17:10	...	...
c	$1403.34 \pm 0.03$	12/28/2026 20:12	$3.03 \pm 0.74$	$0.15 \pm 1.18$

**Note.** A negative egress-ingress separation between the two planets ( $T'_1 - T_4$ ) indicates an overlapping double transit.

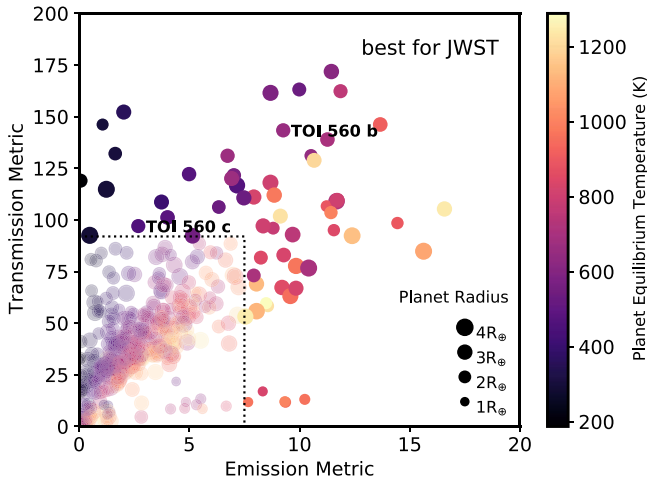


**Figure 24.** Kempton et al. (2018) metrics of signal-to-noise for hypothetical observations of exoplanet atmospheres in transmission (during primary transit) on the vertical axis and emission (during secondary eclipse) on the horizontal axis for a subset of TOIs detected as of the end of 2021 September (NASA Exoplanet Archive; Akeson et al. 2013). Only planets smaller than Neptune, with  $T_{\text{eq}} < 1300$  K, and that are predicted to impart a Doppler RV signal  $K > 3$   $\text{ms}^{-1}$  are shown. The points' sizes are scaled with radius and the color scaled to estimated equilibrium temperature, with the color bar on the right. Increased metric means higher S/N, and the dashed lines indicate the boundary above and to the right of which systems are suitable for JWST observations (Kempton et al. 2018). TOIs 560 b and c are labeled immediately to the right of their data points.

$$\text{ESM} = 4.29 \times 10^6 \times \frac{B_{7.5}(T_{\text{day}})}{B_{7.5}(T_{\text{eff}})} \times \left(\frac{R_p}{R_*}\right)^2 \times 10^{-m_K/5} \quad (6)$$

where  $R_p$  and  $M_p$  are in Earth masses,  $T_{\text{eq}}$  is in kelvin,  $R_*$  is in solar units,  $B_{7.5}$  is the Planck function at a wavelength of  $7.5 \mu\text{m}$ ,  $T_{\text{day}} = 1.1T_{\text{eq}}$ , the scale factor for planets with  $2.75 < R_p < 4 R_{\oplus}$  is 1.28, and  $m_J$  and  $m_K$  are the magnitudes of the host star in the  $J$  and  $K$  bands, respectively. Note that to maintain consistency with ExoFOP-TESS, we use the Chen & Kipping (2016) mass-radius

relation for estimating the planet masses in computing the TSM and ESM values. However, using the Wolfgang et al. (2016) exoplanet mass-radius relation—which includes a different treatment of sample selection in deriving their mass-radius relation—or our median planet masses yields similar results. The TSM and ESM uncertainties are largely due to the current planet mass constraints.

TOI 560 b in particular is among the best TOIs identified to date for both transmission and emission spectroscopy characterization, and TOI 560 c is also suitable for transmission spectroscopy with JWST. The significance of TOI 560 b and c for atmospheric characterization is in part due to its youth and relative brightness at NIR wavelengths, which coincidentally also makes it a priority candidate for NIR RVs. This system is also useful for comparative planetology with other well-studied sub-Neptunes. For example, TOI 560 c is similar size and temperature to GJ 1214b, which is well known for its thick clouds/hazes (Kreidberg et al. 2014). This provides an opportunity to test whether the same is true for a planet with a different host star type, and a different system architecture. In addition, the inner planet is hotter, so it can be used to test the prediction that the atmospheres of hotter planets are less affected by clouds/haze (Crossfield & Kreidberg 2017). Another nice feature of TOI 560 is that the star is not too bright, so it can be observed by every JWST instrument.

Further, since TOI 560 is a multiplanet system, JWST observations could be optimized to capture both transits of b and c with a single telescope pointing and perform comparative planetology; such an observation would be achievable by timing the observations so that the egress of one planet occurs  $\sim 1$  hr before the ingress of the second. Using the NASA Exoplanet Archive (Akeson et al. 2013), for example, there are 129 transits of TOI 560 b and c visible by JWST between 2022 January 6 and 2027 May 5. Of these, there are six (nine) pairs of transits of b and c that have their transit-midpoints within 6 (10) hr of one another visible by JWST, or about one (two) per year. Three of these six closest transit pairs are overlapping, and the other three have predicted time separations of 9 minutes—2.5 hr. We summarize these transits in Table 10.

Given that both planets are nearly equal in size, the impact of stellar insolation on atmospheric evolution will be amenable to

investigation. The youth of the TOI 560 system also makes these planets touchstones for constraining the temporal evolution of Neptune-sized exoplanet atmospheres. It will be particularly interesting to constrain atmospheric escape rates for the TOI 560 system to understand the role atmospheric escape may play in the radius distribution of exoplanets at short orbital periods orbiting older main-sequence stars (Pascucci et al. 2019), and the implications it may have for terrestrial planet occurrence rates (Petigura et al. 2013; Mulders et al. 2015, 2018; Fernandes et al. 2019; Dulz et al. 2020).

### 5.5. Comparisons to Contemporaneous Works

During the preparation of this manuscript, additional papers were written presenting an independent HARPS RV analysis of this system in Barragán et al. (2022) as well as transit spectroscopy in Zhang et al. (2022). Our analyses arrived at similar conclusions to Barragán et al. (2022) for the youth of the TOI 560 system, primarily supported by our common analysis of the archival SuperWASP light curve to identify the stellar-rotation period. Our detections of the RV semi-amplitudes are consistent to within the uncertainties of TOI 560 b and c with the work presented in Barragán et al. (2022). Our analysis also included the PFS and HIRES RVs, but not the HARPS and CORALIE RVs, and a joint chromatic RV analysis combining these data sets with our iSHELL RVs may be warranted with continued future RV monitoring of this system to further constrain the masses and confirm the mild eccentricities from the RV data alone.

Differentiating our two works, we had evidence for a moderate eccentricity orbit for planet b from the Spitzer light-curve photoeccentric effect, and therefore we proceeded our analysis with an eccentric model, whereas in Barragán et al. (2022), they assumed a circular-orbit model. Barragán et al. (2022) also presented a more detailed investigation of the suitability of the planets for atmospheric characterization and the search for hydrogen and helium escape, the latter of which a repeated detection of helium escape is reported in Zhang et al. (2022).

## 6. Conclusions and Future Work

In this work, we have presented a validation of the TOI 560 system orbiting a young  $\sim 0.15\text{--}1.4$  Gyr active K4 star, based on three seasons of noncontemporaneous RV measurements from iSHELL, PFS, and HIRES, photometric data from TESS Spitzer, and ground-based follow-up observations from PEST, NGTS and LCO, and high-resolution images from Gemini South, North, and SOAR. The system consists of two nearly equal-sized transiting Neptune-sized planets ( $P = 6.3981, 18.8865$  days,  $R_p = 0.74, 0.71 R_{\text{Nep}}$ ,  $M_b = 0.94^{+0.31}_{-0.23} M_{\text{Nep}}$ ,  $M_c = 1.32^{+0.29}_{-0.32}$ ) in a near 1:3 orbital resonance, both of which are suitable for comparative atmospheric characterization with JWST in a single observation sequence (e.g., a double transit and/or double eclipse). Additionally with the aid of the Spitzer light curve, we confirm a moderate eccentricity for TOI 560 b via the photoeccentric effect. The youth, orbital dynamics, and suitability of TOI 560 b and c for atmospheric characterization make it a touchstone system for characterizing and constraining the dynamics and atmospheric formation and evolution of compact multi-Neptune planetary systems.

In the future, additional visible and NIR precise and high cadence RVs are necessary to further constrain the stellar activity, dynamical masses of the planets, to assess if the planets are underdense relative to exoplanets orbiting older main-sequence stars, and to search for additional candidates in the system. Future

contemporaneous and high cadence precise RVs at visible and NIR wavelengths will enable more stringent constraints.

M.M. and P.P.P. acknowledge support from NASA (Exoplanet Research Program award No. 80NSSC20K0251, TESS Cycle 3 Guest Investigator Program award No. 80NSSC21K0349, JPL Research and Technology Development, and Keck Observatory Data Analysis) and the NSF (Astronomy and Astrophysics grants No. 1716202 and 2006517), and the Mt Cuba Astronomical Foundation.

This paper includes data collected by the NASA TESS mission that are publicly available from the Mikulski Archive for Space Telescopes (MAST). Funding for the TESS mission is provided by NASA's Science Mission Directorate. We acknowledge the use of public TESS data from pipelines at the TESS Science Office and at the TESS Science Processing Operations Center.

The authors wish to recognize and acknowledge the very significant cultural role and reverence that the summit of Maunakea has always had within the indigenous Hawaiian community, where the iSHELL and HIRES observations were recorded. We are most fortunate to have the opportunity to conduct observations from this mountain. The authors also wish to thank the California Planet Search (CPS) collaboration for carrying out the HIRES observations recorded in 2020 presented in this work.

This work includes observations obtained at the international Gemini Observatory, a program of NSF's NOIRLab, which is managed by the Association of Universities for Research in Astronomy (AURA) under a cooperative agreement with the National Science Foundation. Some of the observations in the paper made use of the High-Resolution Imaging instrument Zorro obtained under Gemini LLP Proposal Number: GN/S-2021A-LP-105. Zorro was funded by the NASA Exoplanet Exploration Program and built at the NASA Ames Research Center by Steve B. Howell, Nic Scott, Elliott P. Horch, and Emmett Quigley. On behalf of the Gemini Observatory partnership: the National Science Foundation (United States), National Research Council (Canada), Agencia Nacional de Investigación y Desarrollo (Chile), Ministerio de Ciencia, Tecnología e Innovación (Argentina), Ministério da Ciência, Tecnologia, Inovações e Comunicações (Brazil), and Korea Astronomy and Space Science Institute (Republic of Korea). Data were collected as part of program GN-2019A-LP-101.

Based on data collected under the NGTS project at the ESO La Silla Paranal Observatory. The NGTS facility is operated by the consortium institutes with support from the UK Science and Technology Facilities Council (STFC) projects ST/M001962/1 and ST/S002642/1. This work has made use of data from the European Space Agency (ESA) mission Gaia (<https://www.cosmos.esa.int/gaia>), processed by the Gaia Data Processing and Analysis Consortium (DPAC; <https://www.cosmos.esa.int/web/gaia/dpac/consortium>). Funding for the DPAC has been provided by national institutions, in particular the institutions participating in the Gaia Multilateral Agreement.

This paper is based on observations obtained from the Las Campanas Remote Observatory that is a partnership between Carnegie Observatories, The Astro-Physics Corporation, Howard Hedlund, Michael Long, Dave Jurasevich, and SSC Observatories.

MINERVA-Australis is supported by Australian Research Council LIEF grant LE160100001, Discovery grant DP1801-00972, Mount Cuba Astronomical Foundation, and institutional partners University of Southern Queensland, UNSW Sydney, MIT, Nanjing University, George Mason University, University

of Louisville, University of California Riverside, University of Florida, and The University of Texas at Austin. We respectfully acknowledge the traditional custodians of all lands throughout Australia, and recognize their continued cultural and spiritual connection to the land, waterways, cosmos, and community. We pay our deepest respects to all Elders, ancestors and descendants of the Giabal, Jarowair, and Kambuwal nations, upon whose lands the Minerva-Australis facility at Mt Kent is situated.

This work makes use of observations from the LCOGT network. Part of the LCOGT telescope time was granted by NOIRLab through the Mid-Scale Innovations Program (MSIP). MSIP is funded by NSF.

E.A.P. acknowledges the support of the Alfred P. Sloan Foundation.

L.M.W. is supported by the Beatrice Watson Parent Fellowship and NASA ADAP grant 80NSSC19K0597.

A.C. is supported by the NSF Graduate Research Fellowship, grant No. DGE 1842402.

D.H. acknowledges support from the Alfred P. Sloan Foundation, the National Aeronautics and Space Administration (80NSSC19K0379), and the National Science Foundation (AST-1717000).

I.J.M.C. acknowledges support from the NSF through grant AST-1824644.

P.D. acknowledges support from a National Science Foundation Astronomy and Astrophysics Postdoctoral Fellowship under award AST-1903811.

A.B. is supported by the NSF Graduate Research Fellowship, grant No. DGE 1745301.

R.A.R. is supported by the NSF Graduate Research Fellowship, grant No. DGE 1745301.

C.D.D. acknowledges the support of the Hellman Family Faculty Fund, the Alfred P. Sloan Foundation, the David & Lucile Packard Foundation, and the National Aeronautics and

Space Administration via the TESS Guest Investigator Program (80NSSC18K1583).

J.M.A.M. is supported by the NSF Graduate Research Fellowship, grant No. DGE-1842400. J.M.A.M. also acknowledges the LSSTC Data Science Fellowship Program, which is funded by LSSTC, NSF Cybertraining grant No. 1829740, the Brinson Foundation, and the Moore Foundation; his participation in the program has benefited this work.

T.F. acknowledges support from the University of California President's Postdoctoral Fellowship Program.

C.A.B. notes that some of the research described in this publication was carried out in part at the Jet Propulsion Laboratory, California Institute of Technology, under a contract with the National Aeronautics and Space Administration.

*Facilities:* NASA IRTF, Keck Observatory, Magellan Telescope, Gemini North, Gemini South, Fred L. Whipple Observatory, TESS, ESO La Silla Paranal Observatory, Las Cumbres Observatory, SOAR telescope.

*Software:* Python: pycell (Cale et al. 2019), AstroImageJ (Collins et al. 2017), EDI-Vetter Unplugged (Zink et al. 2020), DAVE (Kostov et al. 2019), tpfplotter (Aller et al. 2020), REBOUND (Rein & Liu 2012; Rein & Spiegel 2015), NumPy (Harris et al. 2020), SciPy (Virtanen et al. 2020), Matplotlib (Hunter 2007), AstroPy (Astropy Collaboration et al. 2013), Numba (Finkel et al. 2015), EXOFASTv2 (Eastman et al. 2013).

## Appendix

In this Appendix, we present the results of additional analyses not included in the main text.

### Appendix A Reconnaissance Spectroscopy

Herein we present the detailed reconnaissance spectroscopy from NRES and TRES.

**Table 11**

Average Results for the Stellar Parameters and the Internal Error rms Deviation for the Three NRES Observations (e.g., the Quoted Uncertainties Are Not Propagated)

Parameter	2019-05-12	2019-10-29	2019-11-04	Average
$T_{\text{eff}}$ (K)	$4626 \pm 100$	$4641 \pm 100$	$4650 \pm 100$	$4639 \pm 12$
$\log g$	$4.6 \pm 0.1$	$4.7 \pm 0.1$	$4.7 \pm 0.1$	$4.7 \pm 0.1$
$Fe/H$	$-0.08 \pm 0.06$	$-0.04 \pm 0.06$	$-0.13 \pm 0.06$	$0.08 \pm 0.05$
$v_{\text{ sini}}$ [kms $^{-1}$ ]	$\leq 2$	$\leq 2$	$\leq 2$	$\leq 2$
$M_*$ <sup>a</sup>	$0.702 \pm 0.031 M_{\odot}$	$0.71 \pm 0.03 M_{\odot}$	$0.69 \pm 0.03 M_{\odot}$	$0.7 \pm 0.01$
$R_*$ <sup>a</sup>	$0.677 \pm 0.024 R_{\odot}$	$0.686 \pm 0.024 R_{\odot}$	$0.664 \pm 0.023 R_{\odot}$	$0.676 \pm 0.01$

#### Note.

<sup>a</sup> Estimated from NRES ExoFASTv2 analysis.

**Table 12**

Stellar Parameters for the Two TRES Observations

Parameter	2019-04-16	2019-04-19	SPC
$cc^{\text{PI}}$	0.97	0.97	0.97
S/Ne <sup>b</sup>	39.7	29.9	34.8
$T_{\text{eff}}$ (K)	$4689 \pm 50$	$4688 \pm 50$	$4689 \pm 50^{\text{c}}$
$\log g$	$4.67 \pm 0.1$	$4.69 \pm 0.1$	$4.68 \pm 0.1$
$V_{\text{rot}}$ [Km s $^{-1}$ ]	$2.4 \pm 0.5$	$3.7 \pm 0.5$	$3.1 \pm 0.5$
$[m/H]$	$-0.25 \pm 0.08$	$0.17 \pm 0.08$	$-0.21 \pm 0.08$

**Notes.** The first two columns are from the TRES analysis of each individual spectra, and the SPC analysis of both nights is presented in the third column, with the uncertainties quoted derived from the internal error rms deviation (see *P*; Section 3.1.1).

<sup>a</sup> Peak value of the cross-correlation function.

<sup>b</sup> Effective S/N per spectral pixel.

<sup>c</sup> The formal error is only 1 K, but we adopt a systematic noise floor of 50 K as commonly used for TRES spectra.

## Appendix B Mass–Radius Relation

Figure 25 below shows the mass–radius relationship of TOI 560’s  $3\sigma$  masses plotted in green, compared to all other exoplanets.

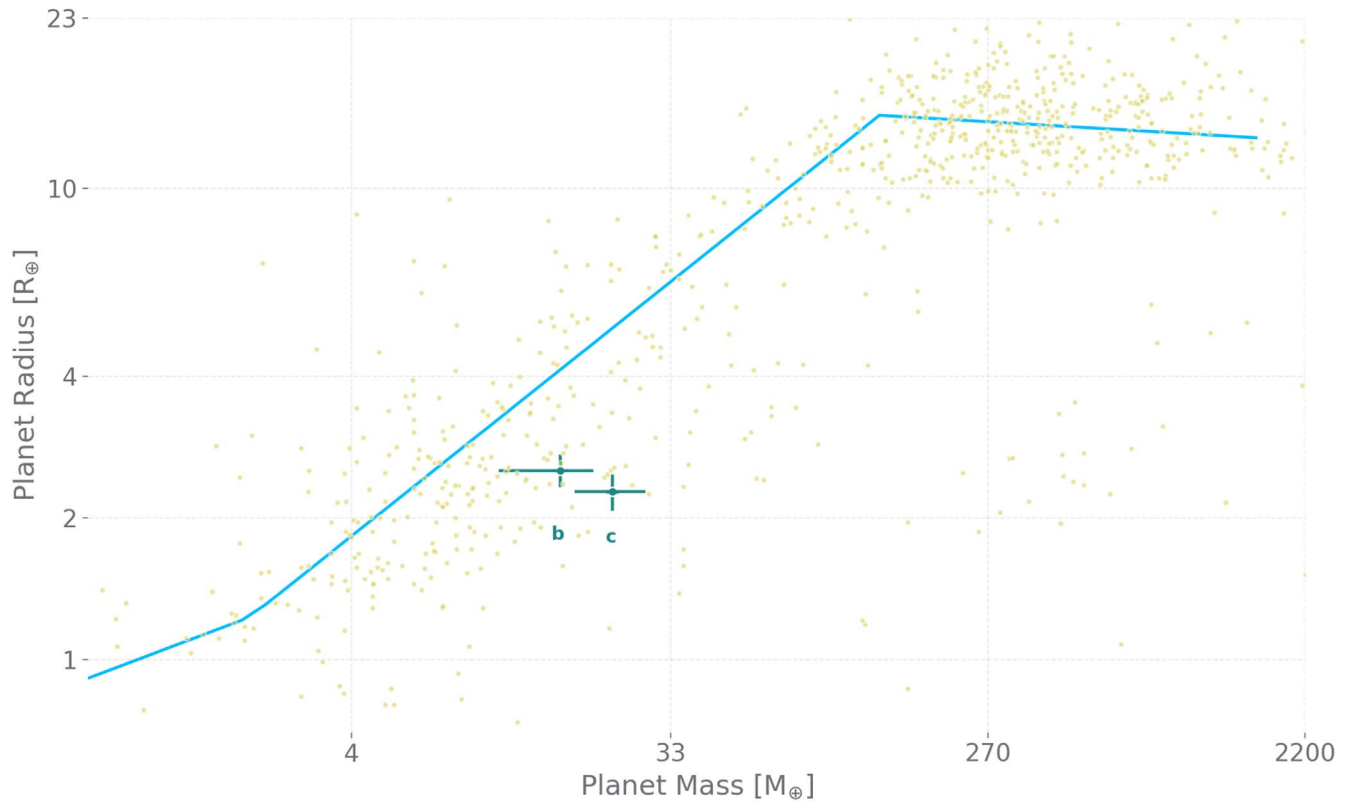


**Figure 25.** The mass–radius diagram for all exoplanets with provided radii and masses from the NASA Exoplanet Archive in yellow. TOI 560’s b and c masses are plotted in green with  $1\sigma$  error bars.

### Appendix C Ground-based Transit Light Curves

The transit light curves of TOI 560 b are shown in Figures 26, 27, and 28.

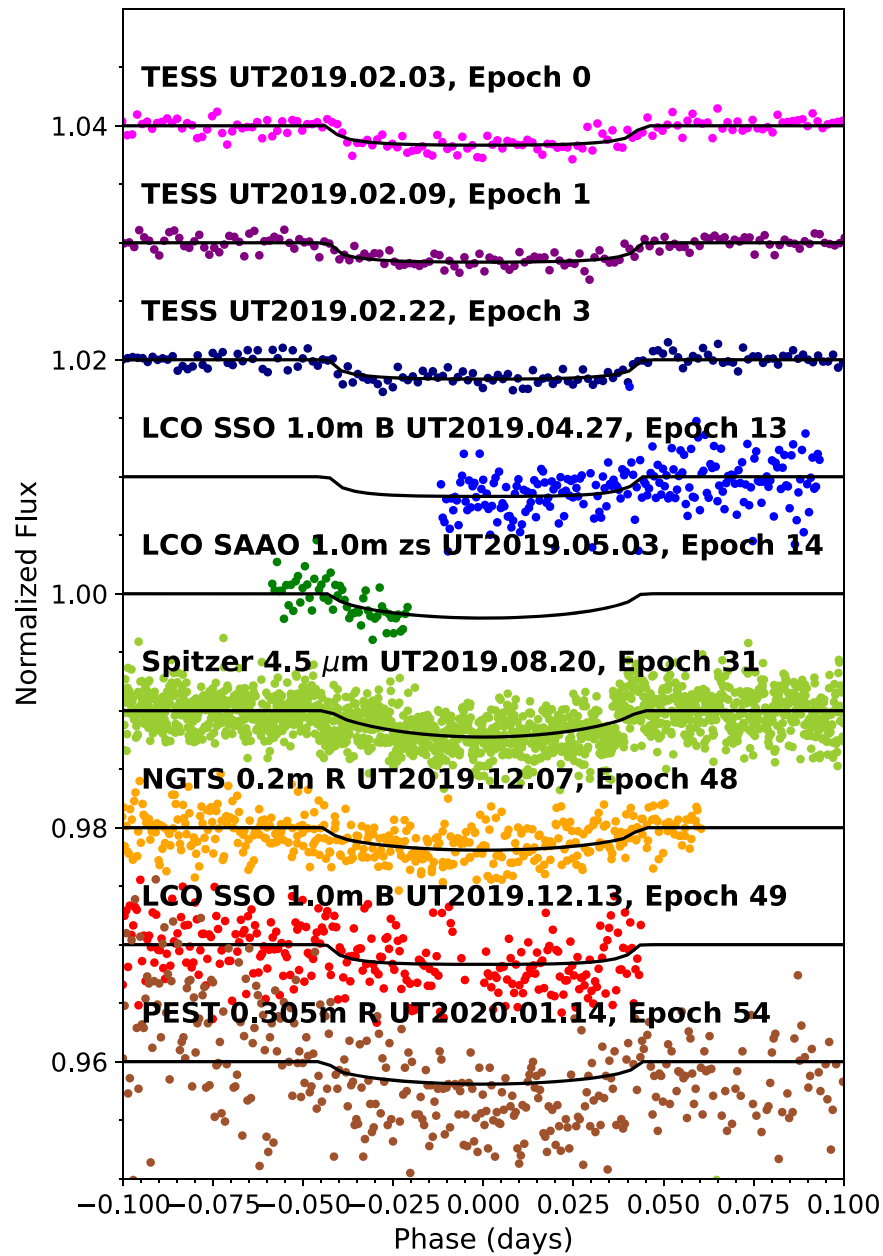


**Figure 26.** TOI 560 b light curves from TESS LCO SSO, LCO SAAO, Spitzer, NGTS, LCO SSO, and PEST observatories as labeled, on the UT dates and in the filters labeled, plotted as a function of time since mid-transit on the horizontal axis and normalized flux with relative arbitrary offsets on the vertical axis. The ground-based and Spitzer data show clear transit detections consistent with the predicted ephemerides from TESS.

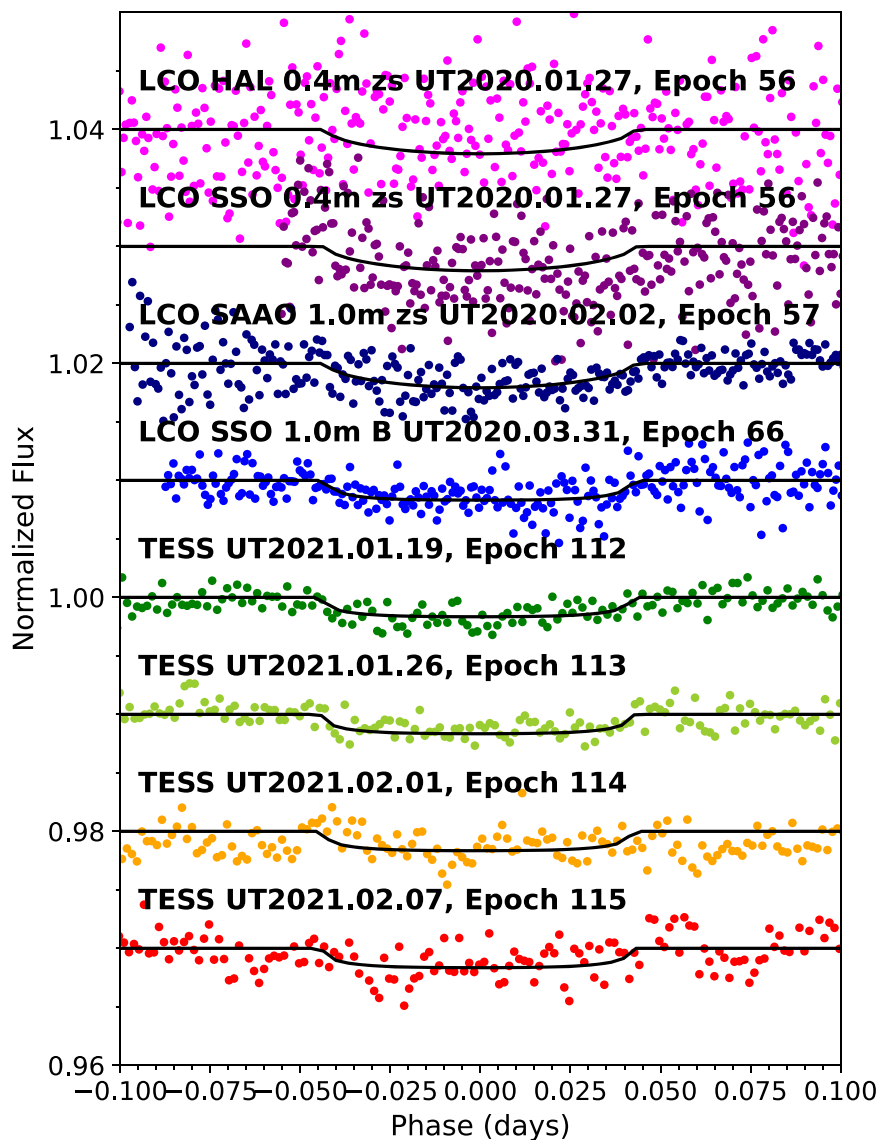


**Figure 27.** TOI 560 b light curves from TESS and LCO HAL, LCO SSO, LCO SAAO, and LCO SSO observatories as labeled, on the UT dates and in the filters labeled, plotted as a function of time since mid-transit on the horizontal axis and normalized flux with relative arbitrary offsets on the vertical axis.

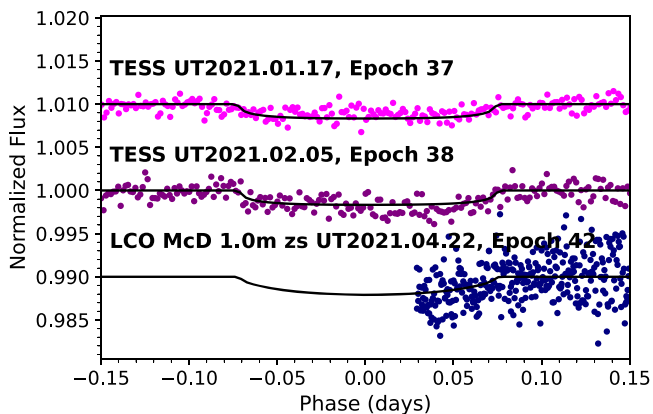


**Figure 28.** TOI 560 c light curves from TESS LCO McD observatories as labeled, on the UT dates and in the filters labeled, plotted as a function of time since mid-transit on the horizontal axis and normalized flux with relative arbitrary offsets on the vertical axis.

### Appendix D RV Models

In this section we show the results if other models that we considered in our RV analysis.

#### *D.1. No Gaussian Process Model for Stellar Activity*

Here we present the results of an RV model with no GP applied to account for the stellar activity.

#### *D.2. Joint GP First Chromatic Kernel $J_1$ Model*

Here we present the results of an RV model using the joint GP chromatic Kernel  $J_1$  model to parameterize the stellar activity amplitude through a linear kernel where each amplitude is a free parameter, as in Cale et al. (2021).

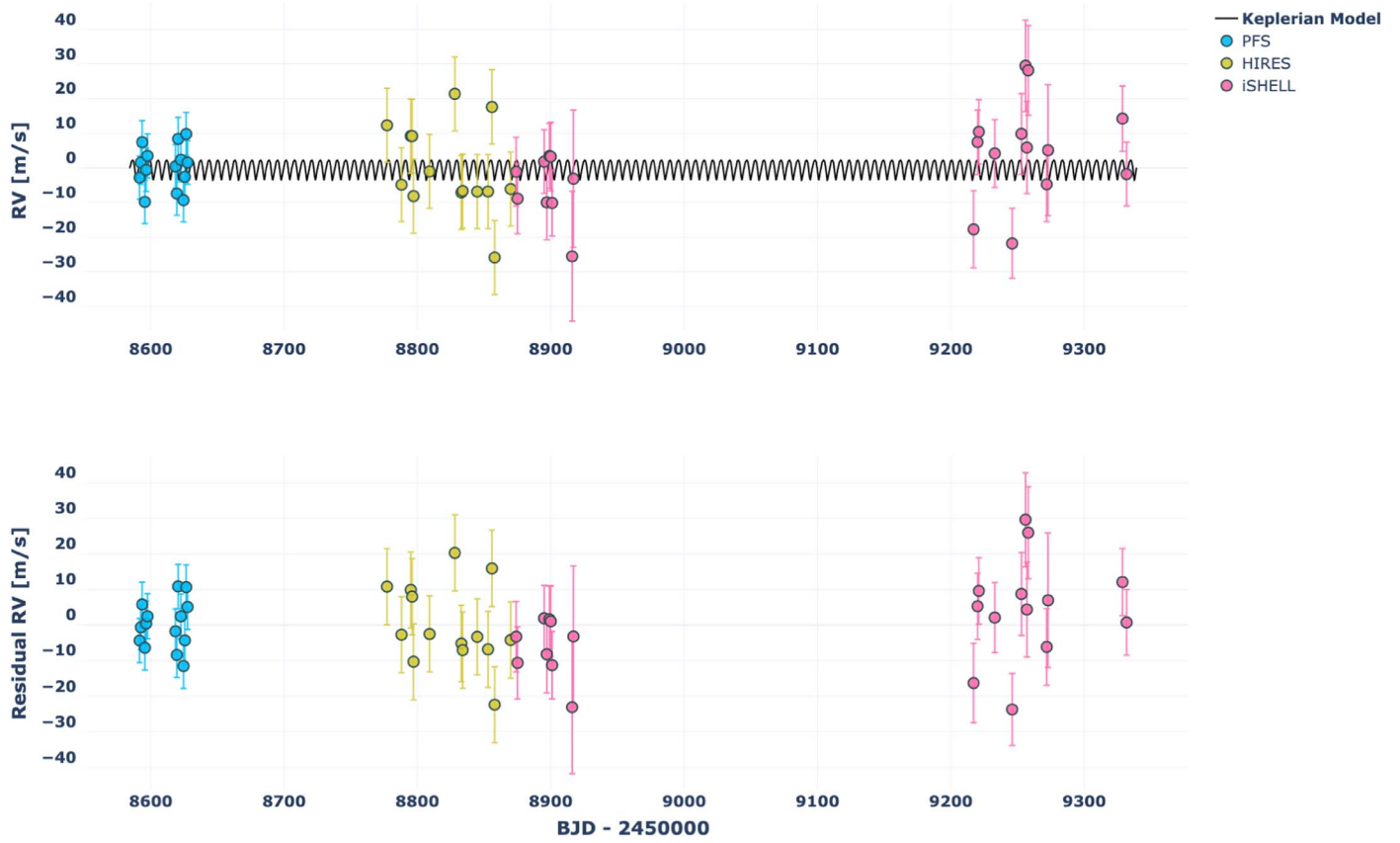


**Figure 29.** Full RV time-series plot, with the black line representing our Keplerian model of the b and c planets. Pink, yellow, and blue data points are nightly iSHELL, HIRES, and PFS RVs, respectively. The top plot shows the RVs over the full time baseline of observations, while the bottom plot shows the residuals (data – model).

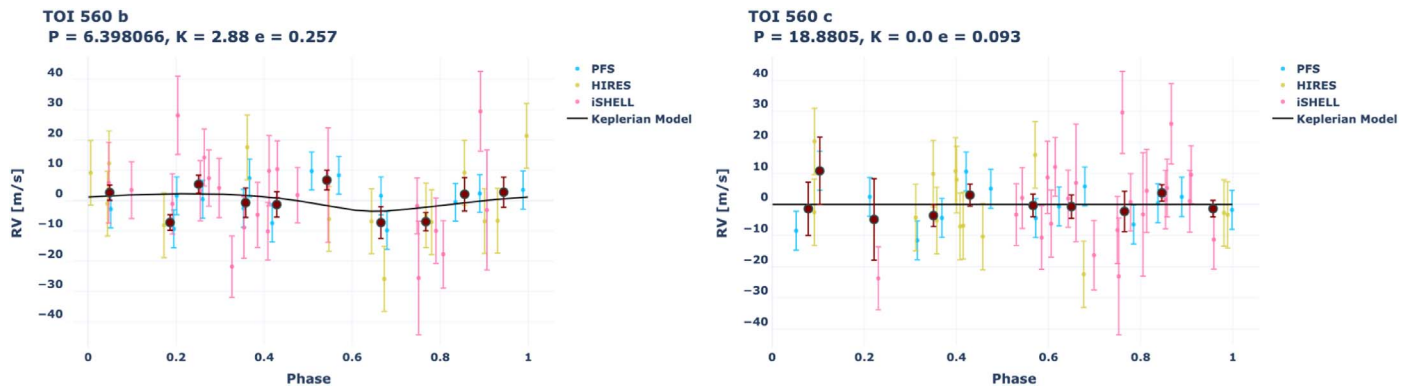


**Figure 30.** RV time-series plots phased to the period of b (left) and c (right), with the black models representing each individual planet signal, after subtracting the other planet signal. Pink, yellow, and blue data points are nightly iSHELL, HIRES, and PFS RVs, and red points are binned nightly RVs.

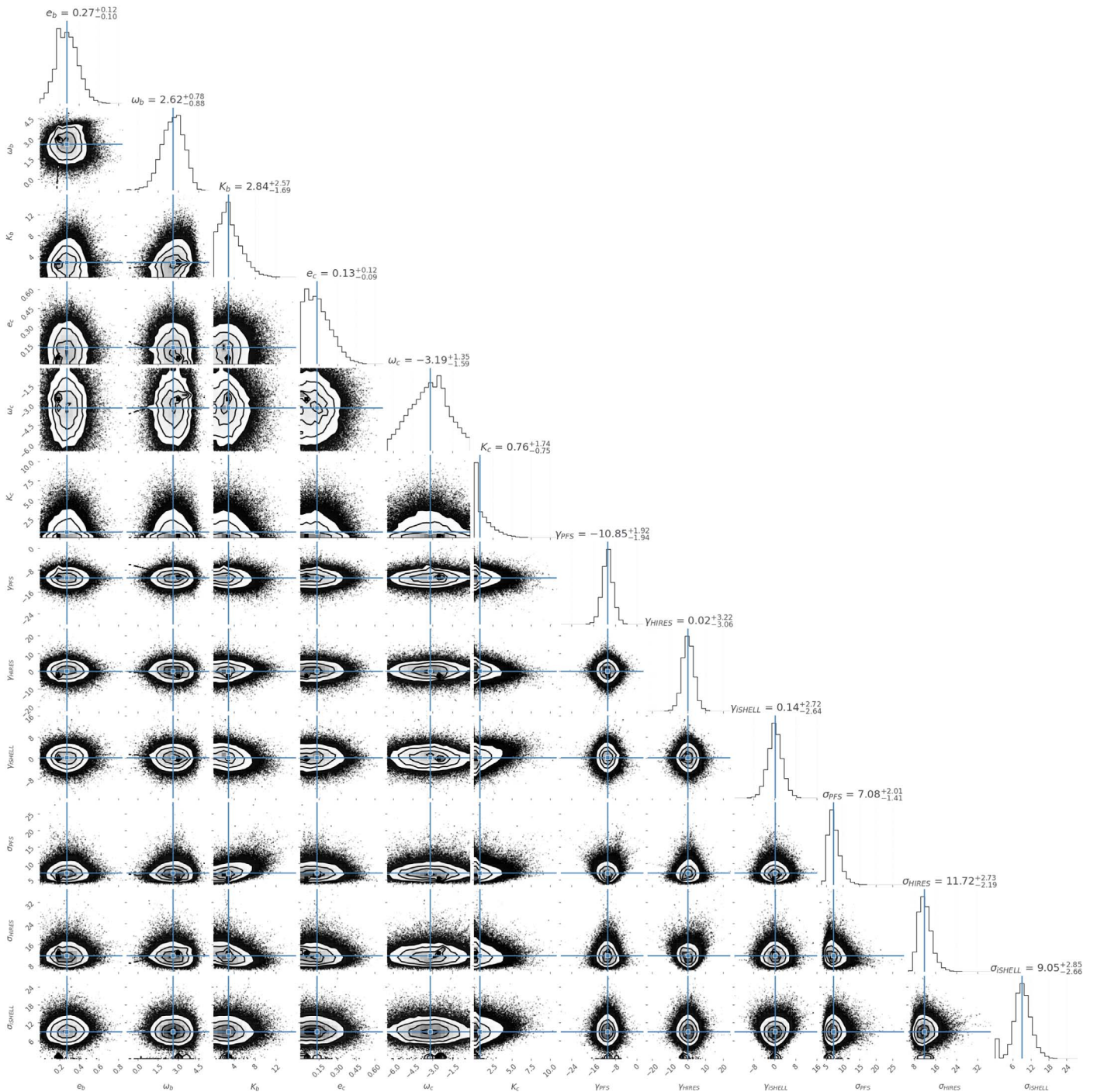


**Figure 31.** MCMC cornerplot of our two-planet RV model (iSHELL+HIRES+PFS), showing the posterior distributions and covariances of each model parameter that we allowed to vary.

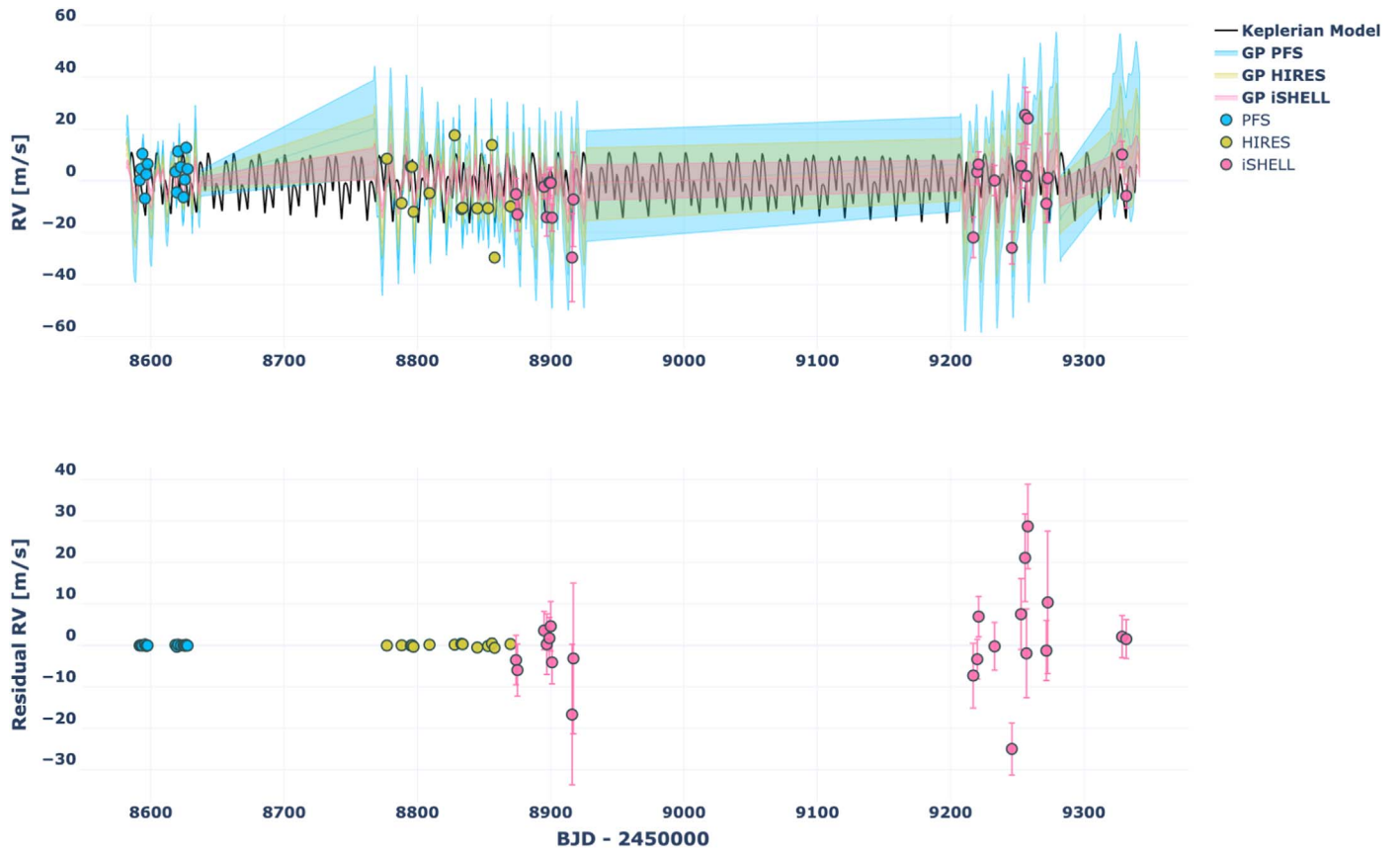


**Figure 32.** Full, unphased RV time-series plot for the joint GP first chromatic Kernel  $J_1$  model with the 12.2 day prior on  $\eta_p$ . Residuals (data – model) are shown in the lower plot. The stellar activity GP model appears to be flexible enough to over-fit the HIRES and PFS RVs.

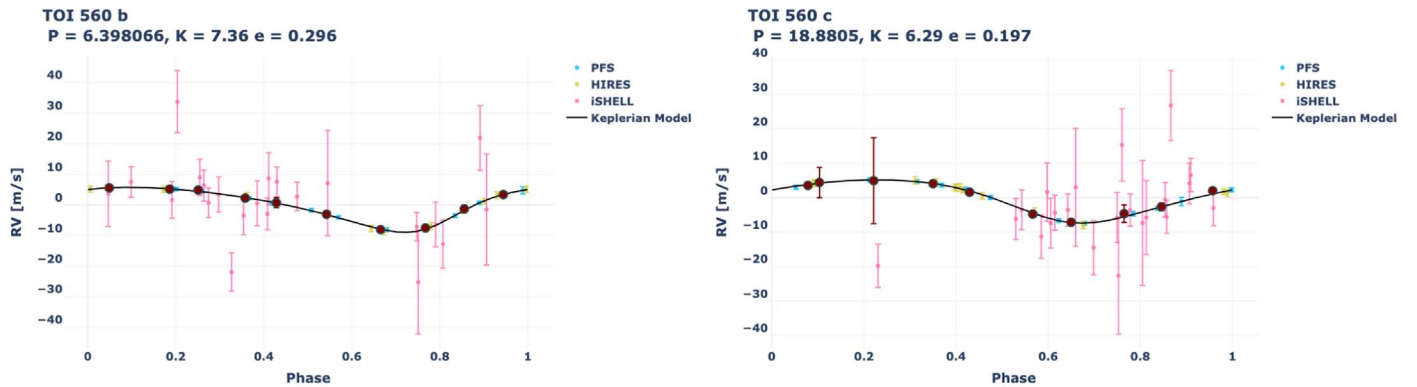


**Figure 33.** RV time-series plot for the joint GP first chromatic Kernel  $J_1$  model with the 12.2 day prior on  $\eta_p$ , phased to the period of b and c, respectively, after subtracting the best-fit stellar activity model and the other planet.

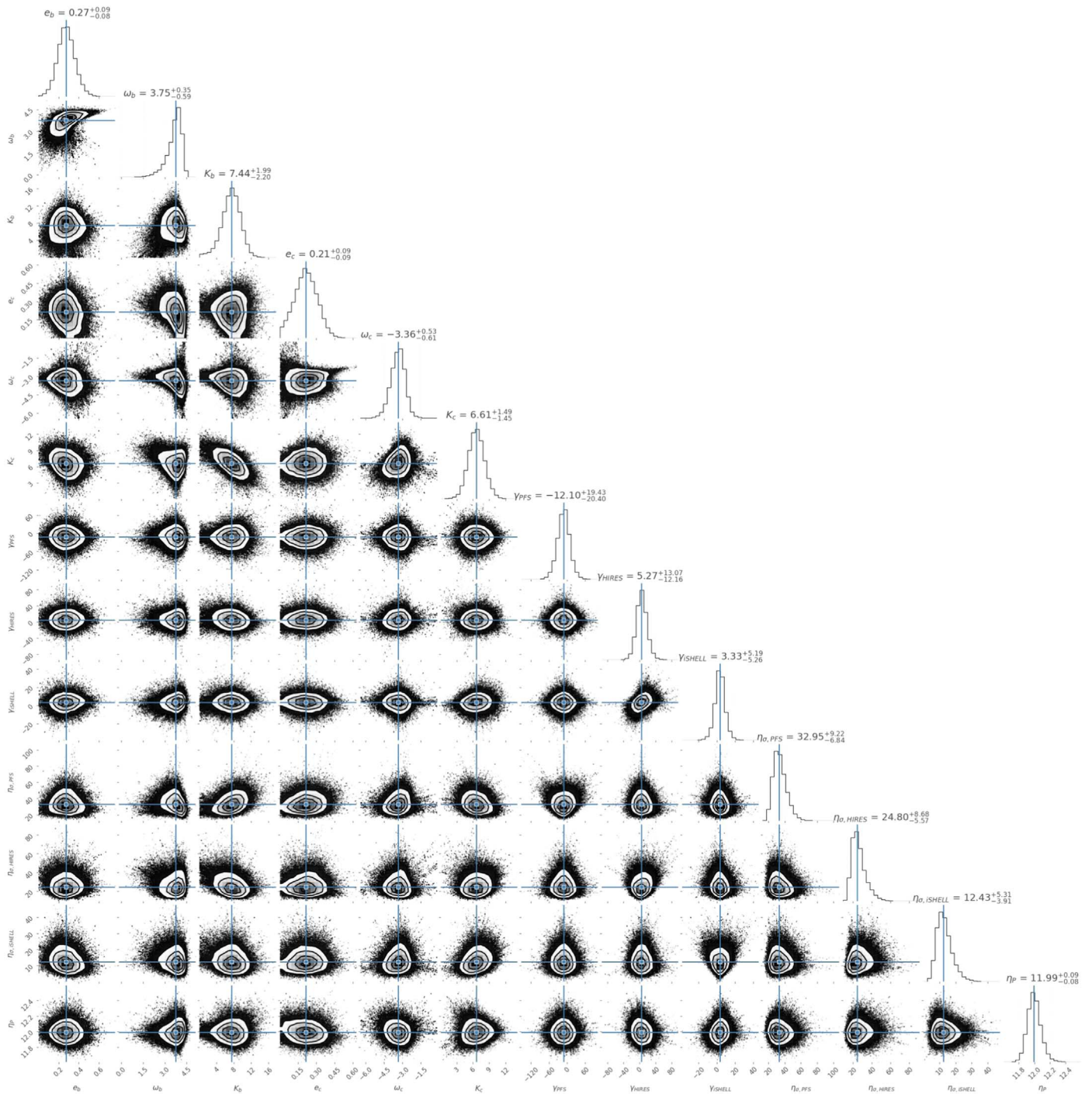


**Figure 34.** MCMC cornerplot of our joint GP first chromatic Kernel  $J_1$  model with the 12.2 day prior on  $\eta_p$ , showing the posterior distributions and covariances of each model parameter that we allowed to vary.

### Appendix E Results of Our Disjoint Model

This model is using an independent (disjoint) GP to model each RV data set, akin to `RadVel` (Fulton et al. 2017). Given the lack of overlap between RV data sets, and the relatively sparse RV cadence sampling, this RV model yields similar over-fit results to our  $J_1$  joint kernel analysis in the previous subsection.

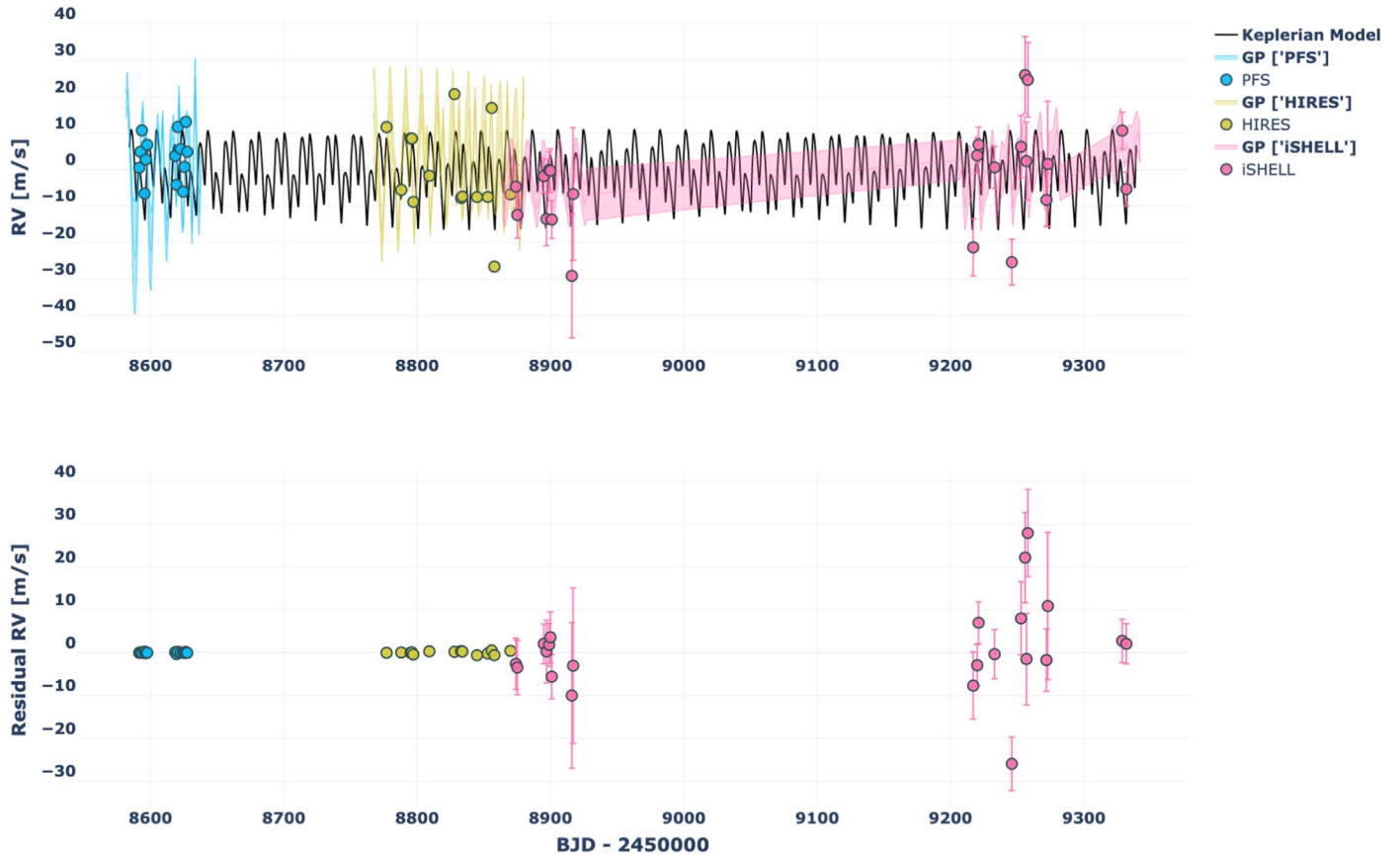


**Figure 35.** Full, unphased RV time-series plot for the disjoint GP model with the 12.2 day prior on  $\eta_p$ . Residuals (data – model) are shown in the lower plot as in previous figures.

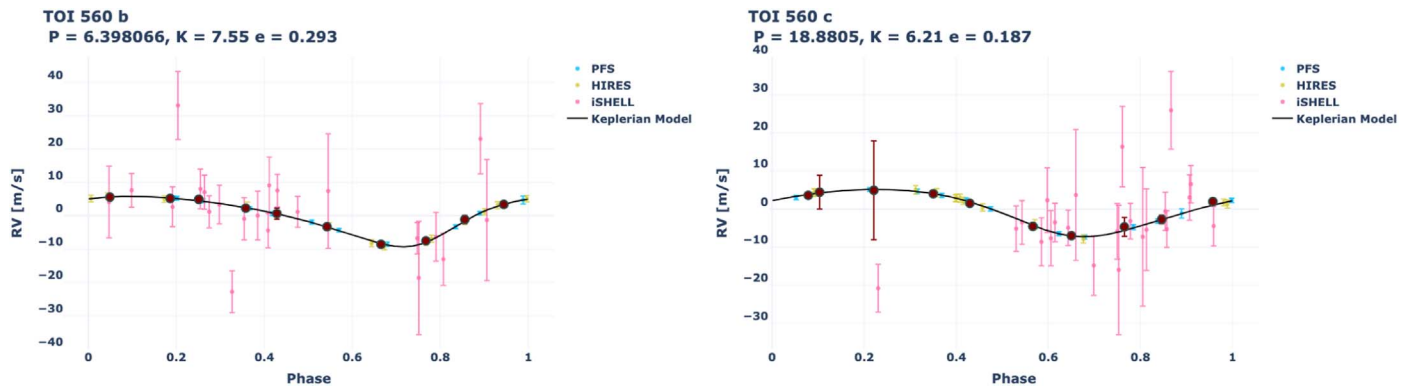


**Figure 36.** RV time-series plot for the disjoint GP model with the 12.2 day prior on  $\eta_p$ , phased to the period of b and c, respectively, after subtracting the best-fit stellar activity model and the other planet.

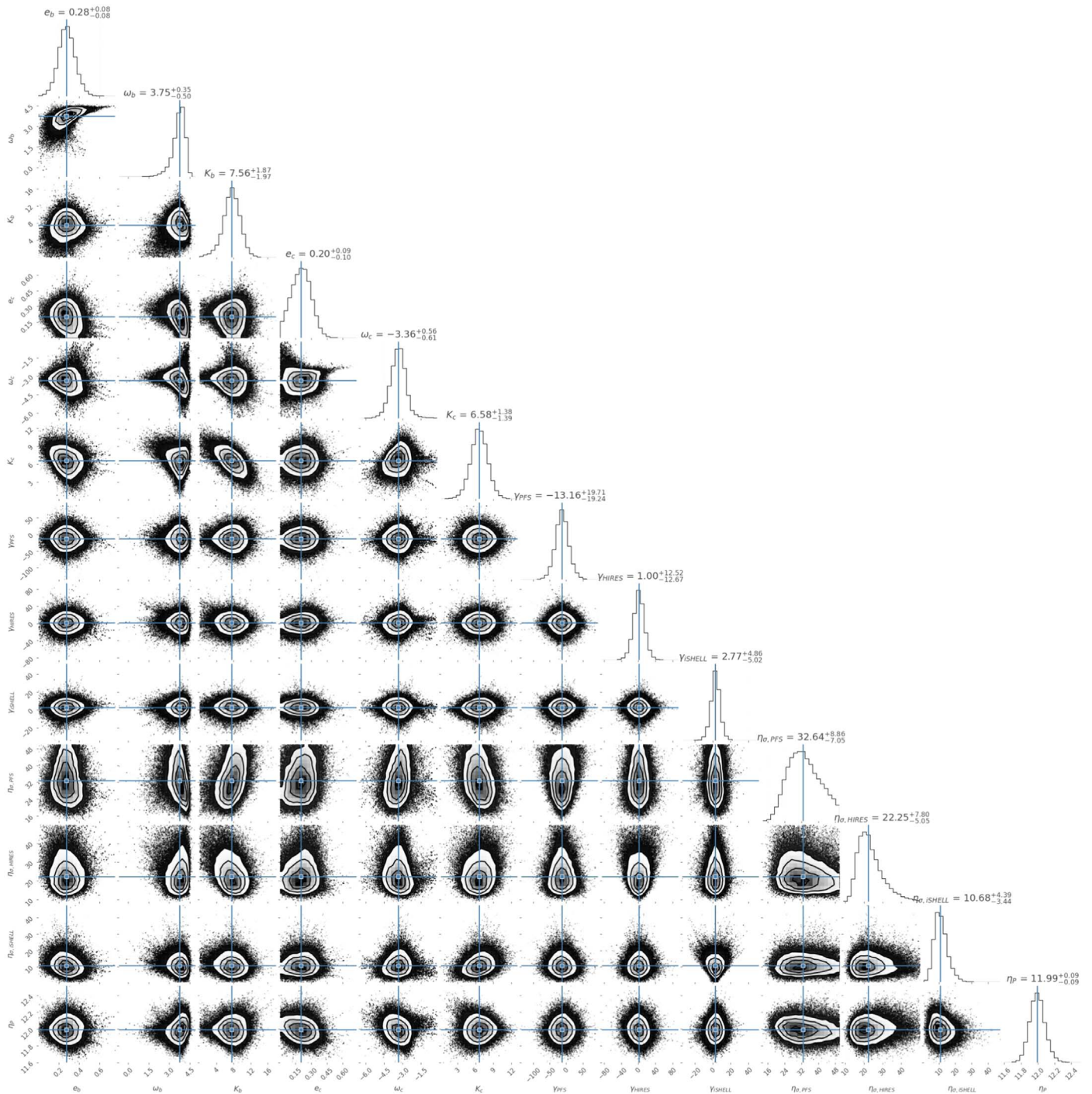


**Figure 37.** MCMC cornerplot of our disjoint GP model for all spectrographs with the 12.2 day prior on  $\eta_p$ , showing the posterior distributions and covariances of each model parameter that we allowed to vary.

## Appendix F

### Summary of the Priors Used in the $J_1$ and Disjoint Kernels

Here we present the model parameters and priors used in the  $J_1$  and disjoint kernels.

**Table 13**

Circular Model Parameters and Prior Distributions Used in Our Model That Considers the Transiting b and c Planets, as well as the Recovered MAP Fit and MCMC Posteriors for the  $J_1$  and Disjoint Kernel Models

Parameter [units]	Initial Value ( $P_0$ )	Priors	MAP Value ( $J_1$ )	MCMC Posterior ( $J_1$ )	MAP Value (Disjoint)	MCMC Posterior (Disjoint)
$P_b$ (days)	6.3980661	locked <sup>a</sup>	...	...	...	...
$TC_b$ (days)	2458517.68971	locked <sup>a</sup>	...	...	...	...
$e_b$	0.294	$\mathcal{U}(0, 1);$ $\mathcal{N}(P_0, 0.13)$	0.30	$0.27^{+0.09}_{-0.08}$	0.29	$0.28^{+0.08}_{-0.08}$
$\omega_b$	$130\pi/180$	$\mathcal{U}(P_0 - \pi, P_0 + \pi);$ $\mathcal{N}(P_0, 45\pi/180)$	3.87	$3.75^{+0.35}_{-0.59}$	3.81	$3.75^{+0.35}_{-0.50}$
$K_b$ ( $\text{m s}^{-1}$ )	10	$\mathcal{U}(0, \infty)$	7.36	$7.43^{+1.10}_{-2.21}$	7.54	$7.56^{+1.88}_{-1.97}$
$P_c$ (days)	18.8805	locked <sup>a</sup>	...	...	...	...
$TC_c$ (days)	2458533.593	locked <sup>a</sup>	...	...	...	...
$e_c$	0.093	$\mathcal{U}(0, 1);$ $\mathcal{N}(P_0, 0.13)$	0.20	$0.21^{+0.09}_{-0.09}$	0.19	$0.20^{0.10}_{-0.10}$
$\omega_c$	$190\pi/180$	$\mathcal{U}(P_0 - \pi, P_0 + \pi);$ $\mathcal{N}(P_0, 45\pi/180)$	-3.61	$-3.36^{+0.53}_{-0.62}$	-3.57	$-3.36^{+0.56}_{-0.62}$
$K_c$ ( $\text{m s}^{-1}$ )	10	$\mathcal{U}(0, \infty)$	6.29	$6.61^{+1.49}_{-1.49}$	6.21	$6.58^{+1.39}_{-1.40}$
$\gamma_{\text{ISHELL}}$ ( $\text{m s}^{-1}$ )	$\text{MEDIAN}(\text{RV}_{\text{ISHELL}})+1^{\text{b}}$	$\mathcal{N}(P_0, 100)$	3.73	$3.33^{+5.21}_{-5.29}$	3.15	$2.77^{+4.88}_{-5.04}$
$\gamma_{\text{PFS}}$ ( $\text{m s}^{-1}$ )	$\text{MEDIAN}(\text{RV}_{\text{PFS}})+1^{\text{b}}$	$\mathcal{N}(P_0, 100)$	-13.85	$-12.10^{+19.52}_{-20.47}$	-14.20	$-13.16^{+19.80}_{-19.31}$
$\gamma_{\text{HIRES}}$ ( $\text{m s}^{-1}$ )	$\text{MEDIAN}(\text{RV}_{\text{HIRES}})+1^{\text{b}}$	$\mathcal{N}(P_0 + 1, 100)$	4.34	$5.27^{+13.12}_{-12.22}$	1.19	$0.996^{+12.57}_{-12.73}$
$\eta_P$	12.03	$\mathcal{N}(P_0, 0.07)$	111.97	$11.99^{+0.09}_{-0.08}$	11.97	$11.99^{+0.09}_{-0.09}$
$\eta_\ell$	0.44	locked <sup>a</sup>	...	...	...	...
$\eta_\tau$	57.96	locked <sup>a</sup>	...	...	...	...
$\eta_{\sigma,\text{ISHELL}}$	$\text{STDDEV}_{\text{ISHELL}}$	$\mathcal{J}(0.67, 50)$	9.54	$12.43^{+5.34}_{-3.92}$	8.43	$10.68^{+4.41}_{-3.45}$
$\eta_{\sigma,\text{PFS}}$	$\text{STDDEV}_{\text{PFS}}$	$\mathcal{J}(0.67, 50)$	29.36	$32.95^{+9.27}_{-6.86}$	30.04	$32.64^{+8.90}_{-7.07}$
$\eta_{\sigma,\text{HIRES}}$	$\text{STDDEV}_{\text{HIRES}}$	$\mathcal{J}(0.67, 50)$	13.63	$18.77^{+7.49}_{-5.30}$	17.34	$22.25^{+7.84}_{-5.06}$

#### Notes.

<sup>a</sup> Locked indicates the parameter is fixed. Gaussian priors are denoted by  $\mathcal{N}(\mu, \sigma)$ , uniform priors by  $\mathcal{U}(\text{lower bound}, \text{upper bound})$ , and Jeffrey's priors by  $\mathcal{J}(\text{lower bound}, \text{upper bound})$ . The initial values for  $\eta_\sigma$  are set to the standard deviation of the respective data sets.

<sup>b</sup> We want the initial value to be the median of the RVs for that spectrograph; the +1 is used in case the median is already zero, as Nelder–Mead solvers cannot start at zero.

## Appendix G

### Summary of the Priors Used in the No GP RV Analysis

**Table 14**

Circular Model Parameters and Prior Distributions Used in Our Model That Considers the Transiting b and c Planets, as well as the Recovered MAP Fit and MCMC Posteriors for the No GP Runs

Parameter [units]	Initial Value ( $P_0$ )	Priors	MAP Value	MCMC Value
$P_b$ (days)	6.3980661	locked <sup>a</sup>	...	...
$TC_b$ (days)	2458517.68971	locked <sup>a</sup>	...	...
$e_b$	0.294	$\mathcal{U}(0, 1); \mathcal{N}(P_0, 0.13)$	0.26	$0.13^{+0.1}_{-0.1}$
$\omega_b$	$130\pi/180$	$\mathcal{U}(P_0 - \pi, P_0 + \pi), \mathcal{N}(P_0, 45\pi/180)$	2.88	$-3.2^{+1.4}_{-1.6}$
$K_b$ [ $\text{m s}^{-1}$ ]	10	$\mathcal{U}(0, \infty)$	2.3	$2.97^{+2.49}_{-1.85}$
$P_c$ (days)	18.8805	locked <sup>a</sup>	...	...
$TC_c$ (days)	2458533.593	locked <sup>a</sup>	...	...
$e_c$	0.093	$\mathcal{U}(0, 1); \mathcal{N}(P_0, 0.13);$	0.093	$0.13^{+0.1}_{-0.1}$
$\omega_c$	$190\pi/180$	$\mathcal{U}(P_0 - \pi, P_0 + \pi), \mathcal{N}(P_0, 45\pi/180)$	-3.3	$-3.2^{+1.4}_{-1.6}$
$K_c$ [ $\text{m s}^{-1}$ ]	10	$\mathcal{U}(0, \infty)$	$7.4 \times 10^{-5}$	$1.15^{+1.58}_{-0.91}$
$\gamma_{\text{ISHELL}}$ ( $\text{m s}^{-1}$ )	$\text{MEDIAN}(\text{RV}_{\text{ISHELL}}) + \pi/100^{\text{b}}$	$\mathcal{N}(P_0, 100)$	-0.32	$0.18^{+2.78}_{-2.77}$
$\gamma_{\text{PFS}}$ ( $\text{m s}^{-1}$ )	$\text{MEDIAN}(\text{RV}_{\text{PFS}}) + \pi/100^{\text{b}}$	$\mathcal{N}(P_0, 100)$	-10.9	$-10.83^{+1.95}_{-2.03}$
$\gamma_{\text{HIRES}}$ ( $\text{m s}^{-1}$ )	$\text{MEDIAN}(\text{RV}_{\text{HIRES}}) + \pi/100^{\text{a}}$	$\mathcal{N}(P_0, 100)$	0.15	$-0.26^{+3.2}_{-3.1}$

**Notes.**

<sup>a</sup> Locked indicates the parameter is fixed. Gaussian priors are denoted by  $\mathcal{N}(\mu, \sigma)$ .

<sup>b</sup> We want the initial value to be the median of the RVs for that spectrograph; the +1 is used in case the median is already zero, as Nelder–Mead solvers cannot start at zero.

### Appendix H Dave Results

Figures 38 and 39 below show the full DAVE vetting results (top table) for the Sector 8 and 34 light curves, respectively. TESS transit data (top row), the binned data (second row), and different phased diagnostic plots to look for odd-even effects (third row) secondary, tertiary, and “negative” eclipses such as

would be produced by false positives (fourth row). Neither analysis identifies statistically significant evidence for a false-positive scenario for TOI 560 b.

Figure 40 shows the photocenter difference images and PSFs for the TESS light curves. No significant photocenter motion in transit is observed, helping exclude blended eclipsing binary scenarios.

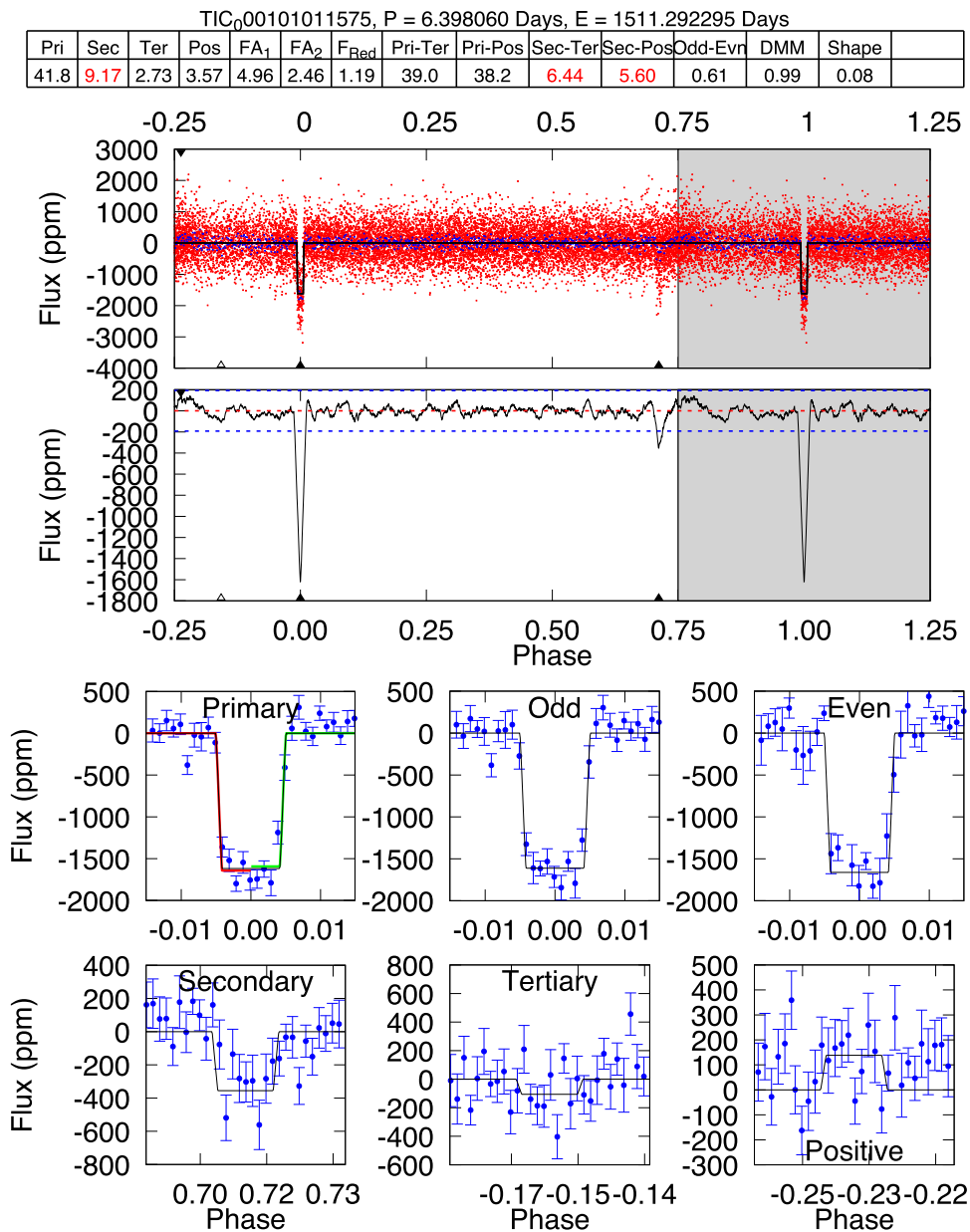


**Figure 38.** Sector 8: full transit data (top), convolved (middle), and different phased scenarios (bottom, labeled) showing primary, odd, even, secondary, tertiary, and positive transits. The table on top show the DV Model-Shift Uniqueness Test. The top line shows the TCE ID and associated orbital period and epoch. The table lists the values for the significances of each event (Pri = primary, Sec = secondary, Ter = tertiary, and Pos = positive), the false-alarm detection thresholds (FA1 and FA2), and the ratio of the noise level on the timescale of the transit duration (red noise) divided by the Gaussian noise (Fred). The difference in significance between the primary and tertiary events (Pri-Ter), the primary and positive events (Pri-Pos), the secondary and tertiary events (SecTer), the secondary and positive events (Sec-Pos), and odd- and even-numbered events (Odd-Evn) are listed next. Finally the values for the depth mean-to-median (DMM), Shape, and the transit asymmetry test (TAT) tests are shown.

TIC<sub>0</sub>00101011575, P = 18.879744 Days, E = 2213.291098 Days

Pri	Sec	Ter	Pos	FA <sub>1</sub>	FA <sub>2</sub>	F <sub>Rad</sub>	Pri-Ter	Pri-Pos	Sec-Ter	Sec-Pos	Odd-Evn	DMM	Shape	TAT
17.0	9.27	6.57	9.23	5.08	2.67	1.87	10.5	7.82	2.69	0.04	5.88	1.00	0.35	1.70

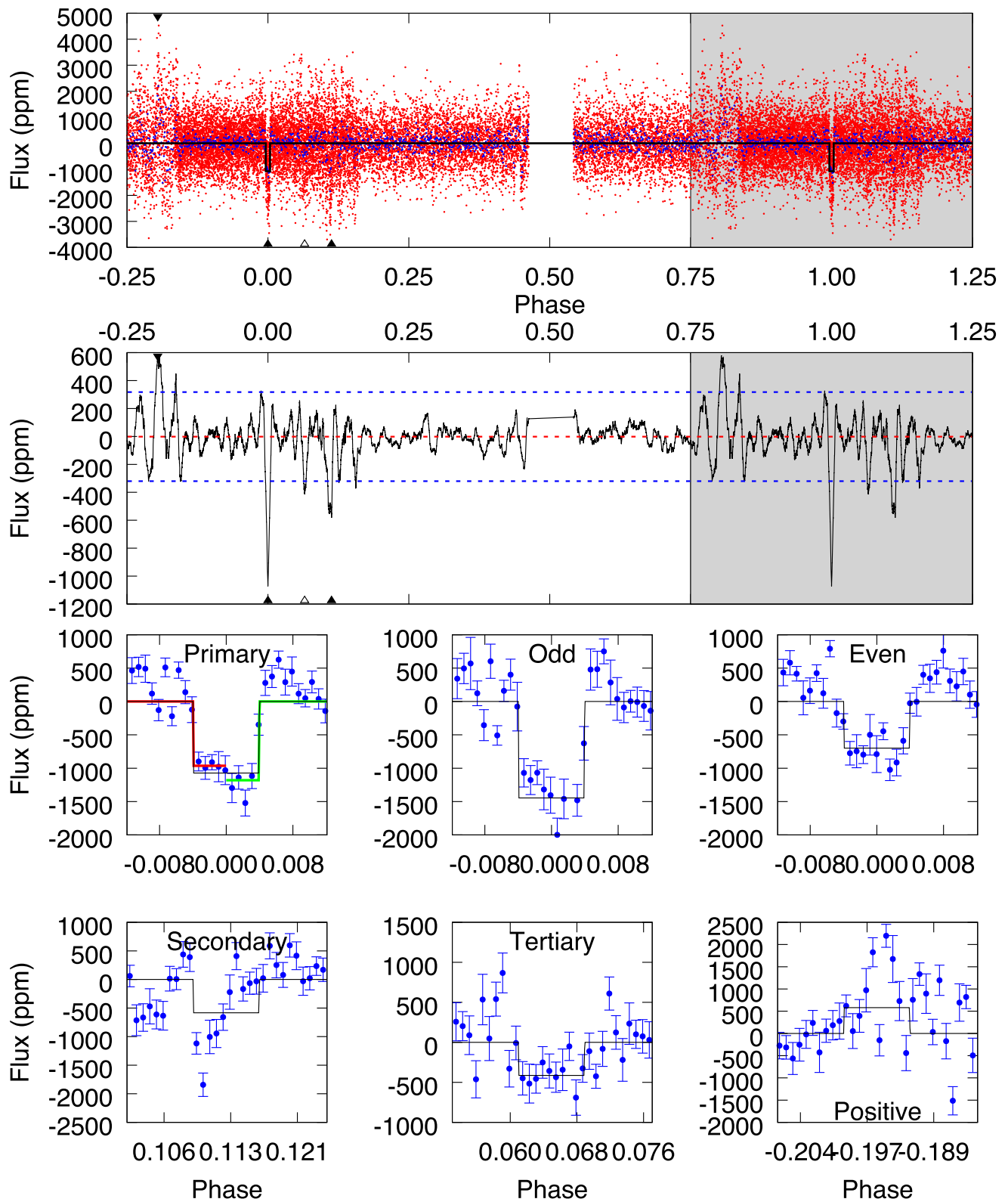


**Figure 39.** Sector 34: full transit data (top), convolved (middle), and different phased scenarios (bottom, labeled) showing primary, odd, even, secondary, tertiary, and positive transits. The table on top show the DV Model-Shift Uniqueness Test. The top line shows the TCE ID and associated orbital period and epoch. The value of Sec-Ter appears red because Sec-Ter < FA<sub>2</sub>. The value of Odd-Evn appears in red because Odd-Evn > FA<sub>1</sub>. The value of “Shape” appears in red if it is >0.3.

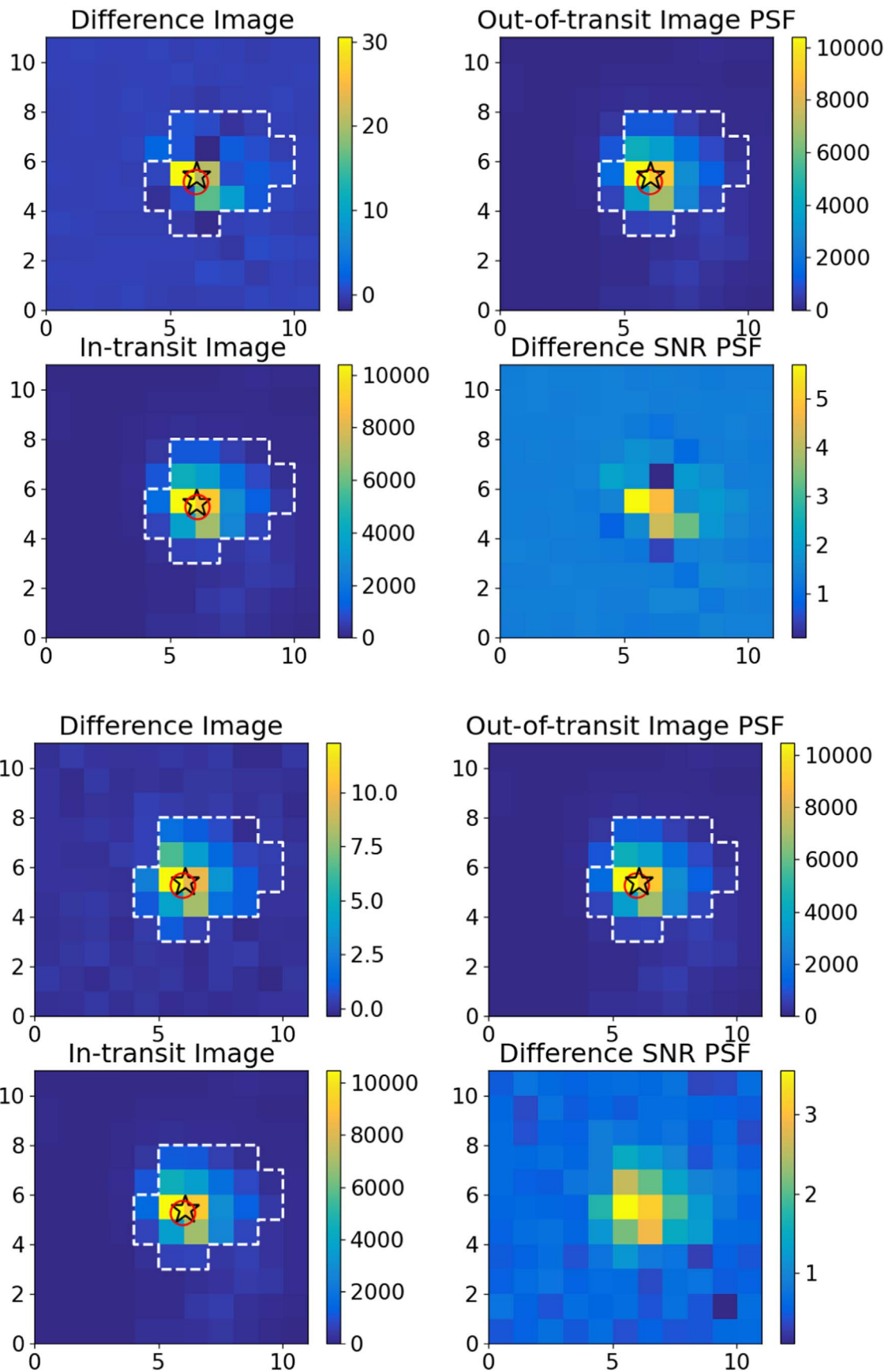


**Figure 40.** Photocenter difference images and PSFs for Sector 8 (top two rows) and 34 (bottom two rows). The black star indicates the TIC position, while the red circle is the observed photocenter. The white dashed line indicates the TESS target pixel aperture used to extract the light curve, just as the orange outlines shown in the TPF plot (Figure 1).

### H.1. RVs of Our EXOFASTv2 Analysis

With EXOFASTv2, we carry out an independent RV analysis with no GP to account for stellar activity, as a means of cross-checking our RV analysis with `pychell`. We recover similar upper limits and posteriors with both approaches. The phased and unphased RVs from the EXOFASTv2 analysis are shown in Figure 41.

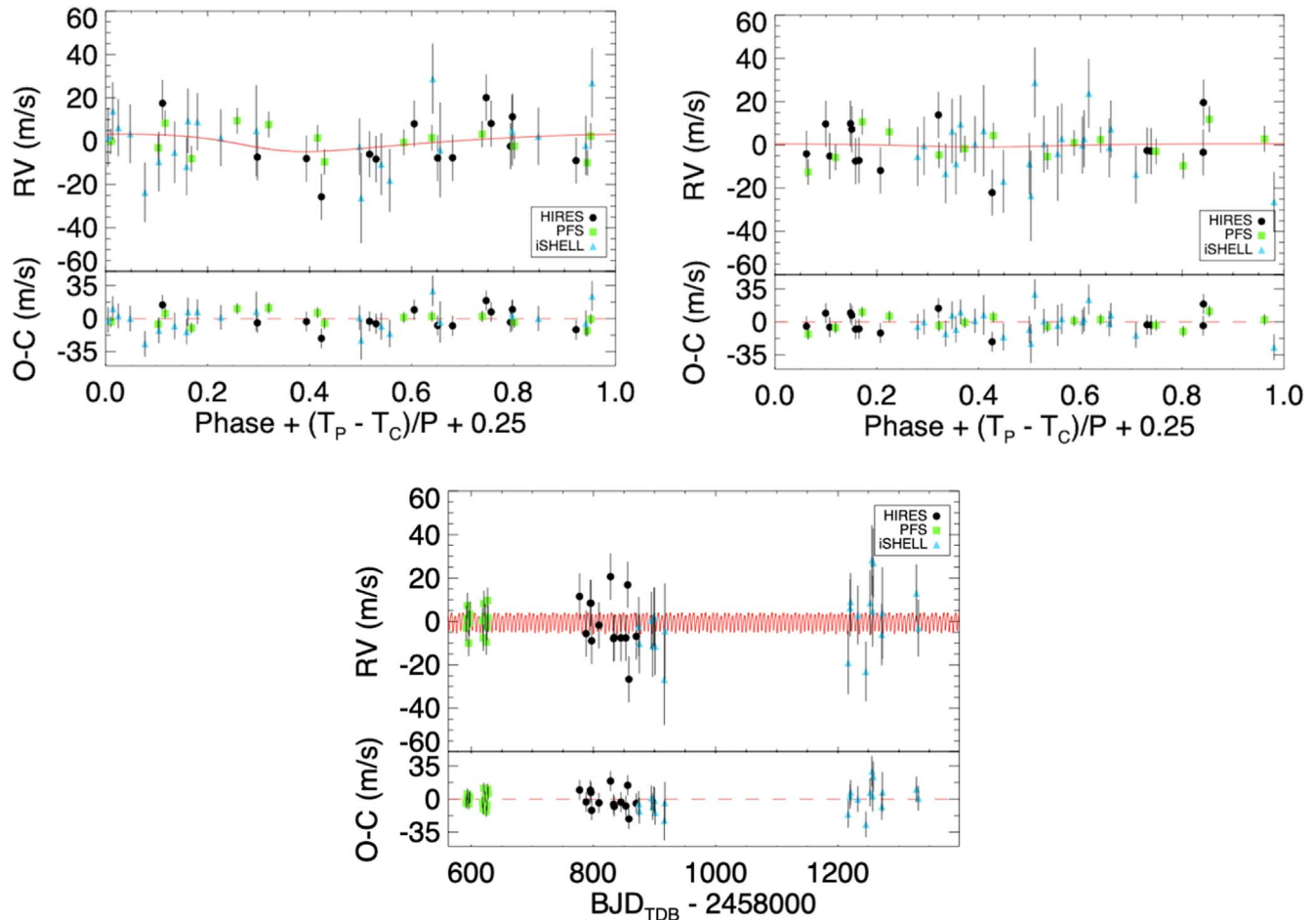


**Figure 41.** RVs obtained from our EXOFASTv2 analysis. Top row: phased RVs and residuals, with the best-fit model in red. Bottom row: unphased RVs.

## Appendix I Radial Velocities

Table 15 lists the RVs used in our analysis from three different spectrographs, iSHELL, PFS, and HIRES.

**Table 15**  
RVs from the Different Spectrographs We Have Used in Our Analysis

Time	Mnvel	Errvel	Tel
2458874.008515	-1.466217	5.969914	iSHELL
2458875.0489	-9.277676	6.318843	iSHELL
2458895.020254	1.423469	4.620647	iSHELL
2458897.033761	-10.358407	7.313267	iSHELL
2458899.005408	3.073978	5.014754	iSHELL
2458900.0048987	2.879875	5.961691	iSHELL
2458900.988993	-10.525324	5.177452	iSHELL
2458915.97533	-25.92508	16.986916	iSHELL
2458916.96779	-3.498715	18.169736	iSHELL
2459217.043971	-18.129482	7.833479	iSHELL
2459220.036259	7.051904	4.807669	iSHELL
2459221.028598	10.012615	4.878999	iSHELL
2459232.98009	3.793529	5.757477	iSHELL
2459245.961775	-22.181634	6.264058	iSHELL
2459252.899543	9.439542	8.503822	iSHELL
2459255.971086	29.092975	10.547535	iSHELL
2459256.967084	5.499865	10.704609	iSHELL
2459257.97079	27.775656	10.204183	iSHELL
2459271.925394	-5.116571	7.272103	iSHELL
2459272.952189	4.726328	17.173103	iSHELL
2459328.734044	13.861937	5.093228	iSHELL
2459331.828947	-2.145161	4.680086	iSHELL
2458591.59721	-13.67	0.44	PFS
2458592.55596	-9.3	0.53	PFS
2458593.61288	-3.46	0.51	PFS
2458595.61376	-20.71	0.66	PFS
2458596.60841	-11.42	0.6	PFS
2458597.591	-7.39	1.2	PFS
2458618.52548	-10.43	0.59	PFS
2458619.53717	-18.31	0.6	PFS
2458620.50553	-2.51	0.52	PFS
2458622.55362	-8.55	0.54	PFS
2458624.50368	-20.21	0.59	PFS
2458625.51752	-13.44	0.55	PFS
2458626.50784	-1.11	0.62	PFS
2458627.5164	-9.31	0.59	PFS
2458777.117606	12.8465553361664	0.874164164066315	HIRES
2458788.120576	-4.3158532184062	0.883318662643433	HIRES
2458795.078952	9.74058435517379	0.96750670671463	HIRES
2458796.044556	9.71581891692533	0.99626761674881	HIRES
2458797.109961	-7.62476348436288	0.957593381404877	HIRES
2458809.083128	-0.466031437909477	0.951945245265961	HIRES
2458827.972435	21.9254428753361	0.960972011089324	HIRES
2458832.988014	-6.58019230860952	1.08839976787567	HIRES
2458833.948473	-6.12234576086814	1.06621098518372	HIRES
2458844.911132	-6.30641359100671	1.05241250991821	HIRES
2458852.955442	-6.28103672598236	0.923207104206085	HIRES
2458855.901039	18.1420626828827	1.26564979553223	HIRES
2458857.895081	-25.3380374118174	1.04208660125732	HIRES
2458869.88686	-5.56625046683735	1.06461870670319	HIRES

## ORCID iDs

Mohammed El Mufti  <https://orcid.org/0000-0001-8364-2903>  
 Peter P. Plavchan  <https://orcid.org/0000-0002-8864-1667>  
 Howard Isaacson  <https://orcid.org/0000-0002-0531-1073>  
 Bryson L. Cale  <https://orcid.org/0000-0001-6279-0595>  
 Dax L. Feliz  <https://orcid.org/0000-0002-2457-7889>  
 Michael A. Reefe  <https://orcid.org/0000-0003-4701-8497>  
 Coel Hellier  <https://orcid.org/0000-0002-3439-1439>  
 Keivan Stassun  <https://orcid.org/0000-0002-3481-9052>  
 Jason Eastman  <https://orcid.org/0000-0003-3773-5142>  
 Eric Gaidos  <https://orcid.org/0000-0002-5258-6846>  
 Veselin Kostov  <https://orcid.org/0000-0001-9786-1031>  
 Justin M. Wittrock  <https://orcid.org/0000-0002-7424-9891>  
 Joshua E. Schlieder  <https://orcid.org/0000-0001-5347-7062>  
 Luke G. Bouma  <https://orcid.org/0000-0002-0514-5538>  
 Kevin I. Collins  <https://orcid.org/0000-0003-2781-3207>  
 Farzaneh Zohrabi  <https://orcid.org/0000-0003-2872-9883>  
 Rena A. Lee  <https://orcid.org/0000-0001-7058-4134>  
 David Vermilion  <https://orcid.org/0000-0002-4501-564X>  
 Patrick Newman  <https://orcid.org/0000-0003-3848-3418>  
 Claire Geneser  <https://orcid.org/0000-0001-9596-8820>  
 Natalie M. Batalha  <https://orcid.org/0000-0002-7030-9519>  
 Courtney Dressing  <https://orcid.org/0000-0001-8189-0233>  
 Benjamin Fulton  <https://orcid.org/0000-0003-3504-5316>  
 Andrew W. Howard  <https://orcid.org/0000-0001-8638-0320>  
 Daniel Huber  <https://orcid.org/0000-0001-8832-4488>  
 Stephen R. Kane  <https://orcid.org/0000-0002-7084-0529>  
 Erik A. Petigura  <https://orcid.org/0000-0003-0967-2893>  
 Paul Robertson  <https://orcid.org/0000-0003-0149-9678>  
 Arpita Roy  <https://orcid.org/0000-0001-8127-5775>  
 Lauren M. Weiss  <https://orcid.org/0000-0002-3725-3058>  
 Aida Behrard  <https://orcid.org/0000-0003-0012-9093>  
 Corey Beard  <https://orcid.org/0000-0001-7708-2364>  
 Ashley Chontos  <https://orcid.org/0000-0003-1125-2564>  
 Fei Dai  <https://orcid.org/0000-0002-8958-0683>  
 Paul A. Dalba  <https://orcid.org/0000-0002-4297-5506>  
 Tara Fetherolf  <https://orcid.org/0000-0002-3551-279X>  
 Steven Giacalone  <https://orcid.org/0000-0002-8965-3969>  
 Lea A. Hirsch  <https://orcid.org/0000-0001-8058-7443>  
 Rae Holcomb  <https://orcid.org/0000-0002-5034-9476>  
 Jack Lubin  <https://orcid.org/0000-0001-8342-7736>  
 Andrew Mayo  <https://orcid.org/0000-0002-7216-2135>  
 Teo Močnik  <https://orcid.org/0000-0003-4603-556X>  
 Joseph M. Akana Murphy  <https://orcid.org/0000-0001-8898-8284>  
 Lee J. Rosenthal  <https://orcid.org/0000-0001-8391-5182>  
 Ryan A. Rubenzahl  <https://orcid.org/0000-0003-3856-3143>  
 Nicholas Scarsdale  <https://orcid.org/0000-0003-3623-7280>  
 Christopher Stockdale  <https://orcid.org/0000-0003-2163-1437>  
 Karen Collins  <https://orcid.org/0000-0001-6588-9574>  
 Ryan Cloutier  <https://orcid.org/0000-0001-5383-9393>  
 Thiam-Guan Tan  <https://orcid.org/0000-0001-5603-6895>  
 Nicholas J Scott  <https://orcid.org/0000-0003-1038-9702>  
 Zach Hartman  <https://orcid.org/0000-0003-4236-6927>  
 Elisabeth Matthews  <https://orcid.org/0000-0003-0593-1560>  
 David R. Ciardi  <https://orcid.org/0000-0002-5741-3047>  
 Rachel A. Matson  <https://orcid.org/0000-0001-7233-7508>  
 Allyson Bieryla  <https://orcid.org/0000-0001-6637-5401>  
 E. Furlan  <https://orcid.org/0000-0001-9800-6248>  
 Crystal L. Gnilkka  <https://orcid.org/0000-0003-2519-6161>

Steve B. Howell  <https://orcid.org/0000-0002-2532-2853>  
 César Briceño  <https://orcid.org/0000-0001-7124-4094>  
 Nicholas Law  <https://orcid.org/0000-0001-9380-6457>  
 Andrew W. Mann  <https://orcid.org/0000-0003-3654-1602>  
 Markus Rabus  <https://orcid.org/0000-0003-2935-7196>  
 Marshall C. Johnson  <https://orcid.org/0000-0002-5099-8185>  
 Laura Kreidberg  <https://orcid.org/0000-0003-0514-1147>  
 David Anthony Berardo  <https://orcid.org/0000-0001-6298-412X>  
 Varoujan Gorjian  <https://orcid.org/0000-0002-8990-2101>  
 Farisa Y. Morales  <https://orcid.org/0000-0001-9414-3851>  
 Björn Benneke  <https://orcid.org/0000-0001-5578-1498>  
 Diana Dragomir  <https://orcid.org/0000-0003-2313-467X>  
 Robert A. Wittenmyer  <https://orcid.org/0000-0001-9957-9304>  
 Brendan P. Bowler  <https://orcid.org/0000-0003-2649-2288>  
 Jonathan Horner  <https://orcid.org/0000-0002-1160-7970>  
 John Kielkopf  <https://orcid.org/0000-0003-0497-2651>  
 Huigen Liu  <https://orcid.org/0000-0001-5162-1753>  
 Avi Shporer  <https://orcid.org/0000-0002-1836-3120>  
 C. G. Tinney  <https://orcid.org/0000-0002-7595-0970>  
 Hui Zhang  <https://orcid.org/0000-0003-3491-6394>  
 Duncan J. Wright  <https://orcid.org/0000-0001-7294-5386>  
 Brett C. Addison  <https://orcid.org/0000-0003-3216-0626>

## References

- Addison, B. C., Horner, J., Wittenmyer, R. A., et al. 2021b, *AJ*, 162, 137  
 Addison, B. C., Wright, D. J., Nicholson, B. A., et al. 2021a, *MNRAS*, 502, 3704  
 Addison, B., Wright, D. J., Wittenmyer, R. A., et al. 2019, *PASP*, 131, 115003  
 Aigrain, S., Pont, F., & Zucker, S. 2012, *MNRAS*, 419, 3147  
 Akaike, H. 1974, *ITAC*, 19, 716  
 Akeson, R. L., Chen, X., Ciardi, D., et al. 2013, *PASP*, 125, 989  
 Aller, A., Lillo-Box, J., Jones, D., Miranda, L. F., & Barceló Forteza, S. 2020, *A&A*, 635, A128  
 Alvarado-Gomez, J. D., Cohen, O., Drake, J. J., et al. 2022, *ApJ*, 928, 147  
 Anglada-Escude, G., Amado, P. J., Barnes, J., et al. 2016, *Natur*, 536, 437  
 Anglada-Escudé, G., Tumo, M., Gerlach, E., et al. 2013, *A&A*, 556, A126  
 Astropy Collaboration, Robitaille, T. P., Tollerud, E. J., et al. 2013, *A&A*, 558, A33  
 Ballard, S., Chaplin, W. J., Charbonneau, D., et al. 2014, *ApJ*, 790, 12  
 Barbary, K. 2016, *JOSS*, 1, 58  
 Barnes, S. A. 2007, *ApJ*, 669, 1167  
 Barnes, S. I., Gibson, S., Nield, K., et al. 2012, *Proc. SPIE*, 8446, 844688  
 Barragán, O., Armstrong, D. J., Gandolfi, D., et al. 2022, *MNRAS*, 514, 1606  
 Bean, J. L., Stevenson, K. B., Batalha, N. M., et al. 2018, *PASP*, 130, 114402  
 Benatti, S., Damasso, M., Borsari, F., et al. 2021, *A&A*, 650, A66  
 Bertin, E., & Arnouts, S. 1996, *A&AS*, 117, 393  
 Bianchi, L., Efremova, B., Herald, J., et al. 2011, *MNRAS*, 411, 2770  
 Bluhm, P., Luque, R., Espinoza, N., et al. 2020, *A&A*, 639, A132  
 Bodenheimer, P., Laughlin, G., & Lin, D. N. C. 2003, *ApJ*, 592, 555  
 Borucki, W. J., Koch, D. G., Basri, G., et al. 2011, *ApJ*, 736, 19  
 Brahm, R., Nielsen, L. D., Wittenmyer, R. A., et al. 2020, *AJ*, 160, 235  
 Brown, T. M., Becker, M., Burleson, B., et al. 2013, AAS Meeting Abstracts, 221, 345.23  
 Bryant, E. M., Bayliss, D., McCormac, J., et al. 2020, *MNRAS*, 494, 5872  
 Bryson, S., Kunimoto, M., Koppapu, R. K., et al. 2021, *AJ*, 161, 36  
 Buchhave, L. A., Bakos, G. Á., Hartman, J. D., et al. 2010, *ApJ*, 720, 1118  
 Buchhave, L. A., Bizzarro, M., Latham, D. W., et al. 2014, *Natur*, 509, 593  
 Buchhave, L. A., Dressing, C. D., Dumusque, X., et al. 2016, *AJ*, 152, 160  
 Buchhave, L. A., Latham, D. W., Johansen, A., et al. 2012, *Natur*, 486, 375  
 Burnham, K. P., & Anderson, D. R. 2002, Model Selection and Multimodel Inference (Berlin: Springer)  
 Butler, R. P., Marcy, G. W., Williams, E., et al. 1996, *PASP*, 108, 500  
 Cale, B., Plavchan, P., LeBrun, D., et al. 2019, *AJ*, 158, 170  
 Cale, B., Reefe, M., Plavchan, P., et al. 2021, *AJ*, 162, 295  
 Canto Martins, B. L., Gomes, R. L., Messias, Y. S., et al. 2020, *ApJS*, 250, 20  
 Carolan, S., Vidotto, A. A., Plavchan, P., Villarreal D'Angelo, C., & Hazra, G. 2020, *MNRAS*, 498, L53

- Chabrier, G. 2003, *PASP*, **115**, 763
- Chen, J., & Kipping, D. 2016, *ApJ*, **834**, 17
- Christiansen, J. L., Vanderburg, A., Burt, J., et al. 2017, *AJ*, **154**, 122
- Ciardi, D., Beichman, C., Horch, E., Howell, S., et al. 2015, *ApJ*, **805**, 16
- Ciardi, D. R., Fabrycky, D. C., Ford, E. B., et al. 2013, *ApJ*, **763**, 41
- Cohen, O., Alvarado-Gomez, J. D., Drake, J. J., et al. 2022, *ApJ*, **934**, 189
- Collins, K. A., Kielkopf, J. F., Stassun, K. G., & Hessman, F. V. 2017, *AJ*, **153**, 77
- Cretignier, M., Dumusque, X., Allart, R., et al. 2020, *A&A*, **633**, A76
- Crossfield, I. J. M., & Kreidberg, L. 2017, *AJ*, **154**, 261
- Crossfield, I., Werner, M., Dragomir, D., et al. 2018, Spitzer Transits of New TESS Planets, Spitzer Proposal, **14084**
- Cubillos, P., Harrington, J., Madhusudhan, N., et al. 2013, *ApJ*, **768**, 42
- Curtis, J. L., Aguiros, M. A., Matt, S. P., et al. 2020, *ApJ*, **904**, 140
- David, T. J., Petigura, E. A., Luger, R., et al. 2019a, *ApJL*, **885**, L12
- Dahm, S. E. 2015, *ApJ*, **813**, 108
- David, T. J., Cody, A. M., Hedges, C. L., et al. 2019b, *AJ*, **158**, 79
- Dawson, R. I., & Fabrycky, D. C. 2010, *ApJ*, **722**, 937
- Dawson, R. I., & Johnson, J. A. 2012, *ApJ*, **756**, 122
- Delgado Mena, E., Bertrán de Lis, S., Adibekyan, V. Z., et al. 2015, *A&A*, **576**, A69
- Desort, M., Lagrange, A.-M., Galland, F., Udry, S., & Mayor, M. 2007, *A&A*, **473**, 983
- Dotter, A. 2016, *ApJS*, **222**, 8
- Dreizler, S., Crossfield, I. J. M., Kossakowski, D., et al. 2020, *A&A*, **644**, A127
- Dressing, C. D., & Charbonneau, D. 2015, *ApJ*, **807**, 45
- Duck, A., Gaudi, B. S., Eastman, J. D., & Rodriguez, J. E. 2022, arXiv:2209.09266
- Dulz, S. D., Plavchan, P., Crepp, J. R., et al. 2020, *ApJ*, **893**, 122
- Dumusque, X. 2018, *A&A*, **620**, A47
- Dumusque, X., Boisse, I., Santos, N., et al. 2014, *ApJ*, **796**, 132
- Dumusque, X., Santos, N. C., Udry, S., Lovis, C., & Bonfils, X. 2011a, *A&A*, **527**, A82
- Dumusque, X., Udry, S., Lovis, C., Santos, N. C., & Monteiro, M. J. P. F. G. 2011b, *A&A*, **525**, A140
- Eastman, J. D., Rodriguez, J. E., Agol, E., et al. 2019, arXiv:1907.09480
- Eastman, J., Gaudi, B. S., & Agol, E. 2013, *PASP*, **125**, 83
- Fabrycky, D. C., Lissauer, J. J., Ragozzine, D., et al. 2014, *ApJ*, **790**, 146
- Fazio, G. G., Hora, J. L., Allen, L. E., et al. 2004, *ApJS*, **154**, 10
- Feinstein, A. D., David, T. J., Montet, B. T., et al. 2022b, *ApJL*, **925**, L2
- Feinstein, A. D., France, K., Youngblood, A., et al. 2022a, *AJ*, **164**, 110
- Fernandes, R. B., Mulders, G. D., Pascucci, I., Mordasini, C., & Emsenhuber, A. 2019, *ApJ*, **874**, 81
- Fűrész, G. 2008, [http://doktori.bibl.u-szeged.hu/id/eprint/1135/1/gabor\\_furesz\\_thesis.pdf](http://doktori.bibl.u-szeged.hu/id/eprint/1135/1/gabor_furesz_thesis.pdf)
- Findeisen, K., Hillenbrand, L., & Soderblom, D. 2011, *AJ*, **142**, 23
- Finkel, H., Lam, S. K., Pitrou, A., & Seibert, S. 2015, Numba: a LLVM-based Python JIT compiler, doi:10.1145/2833157.2833162
- Fischer, D. A., Anglada-Escude, G., Arriagada, P., et al. 2016, *PASP*, **128**, 066001
- Flagg, L., Johns-Krull, C., France, K., et al. 2022, *ApJ*, **934**, 8
- Foreman-Mackey, D., Hogg, D. W., Lang, D., & Goodman, J. 2013, *PASP*, **125**, 306
- Fulton, B. J., Petigura, E. A., Blunt, S., & Sinukoff, E. 2018, *PASP*, **130**, 044504
- Fulton, B. J., Petigura, E. A., Howard, A. W., et al. 2017, *AJ*, **154**, 109
- Gagné, J., Faherty, J. K., Moranta, L., & Popinchalk, M. 2021, *ApJL*, **915**, L29
- Gagné, J., Mamajek, E. E., Malo, L., et al. 2018, *ApJ*, **856**, 23
- Gaia Collaboration, Brown, A. G. A., Vallenari, A., et al. 2018, *A&A*, **616**, A1
- Gaidos, E., Hirano, T., Beichman, C., et al. 2022, *MNRAS*, **509**, 2969
- Gan, T., Bedell, M., Wang, S. X., et al. 2021, *MNRAS*, **507**, 2220
- Gao, P., Plavchan, P., Gagné, J., et al. 2016, *PASP*, **128**, 104501
- Gomes da Silva, J., Santos, N. C., Adibekyan, V., et al. 2021, *A&A*, **646**, A77
- Grunblatt, S., Howard, A., & Haywood, R. D. 2015, *ApJ*, **808**, 127
- Guerrero, N. M., Seager, S., Huang, C. X., et al. 2021, *ApJS*, **254**, 39
- Guyon, O. 2005, *ApJ*, **629**, 592
- Harris, C. R., Millman, K. J., van der Walt, S. J., et al. 2020, *Natur*, **585**, 357
- Haywood, R. D. 2015, PhD thesis, University of St Andrews
- Haywood, R. D., Collier Cameron, A., Queloz, D., et al. 2014, *MNRAS*, **443**, 2517
- Henry, T., Jao, W.-C., Subasavage, J., et al. 2006, *AJ*, **132**, 2360
- Hippke, M., & Heller, R. 2019, *A&A*, **623**, A39
- Hirano, T., Krishnamurthy, V., Gaidos, E., et al. 2020, *ApJL*, **899**, L13
- Hobson, M. J., Brahm, R., Jordan, A., et al. 2021, *AJ*, **161**, 235
- Hodapp, K. W., Jensen, J. B., Irwin, E. M., et al. 2003, *PASP*, **115**, 1388
- Howard, A., Johnson, J., Marcy, G., et al. 2010, *ApJ*, **721**, 1467
- Howard, A. W., Marcy, G. W., Bryson, S. T., et al. 2012, *ApJS*, **201**, 15
- Howell, S. B., Everett, M. E., Horch, E. P., et al. 2016, *ApJL*, **829**, L2
- Howell, S. B., Everett, M. E., Sherry, W., Horch, E., & Ciardi, D. R. 2011, *AJ*, **142**, 19
- Howell, S. B., Matson, R. A., Ciardi, D. R., et al. 2021, *AJ*, **161**, 164
- Hunter, J. D. 2007, *CSE*, **9**, 90
- Ilin, E., & Poppenhaeger, K. 2022, *MNRAS*, **513**, 4579
- Jenkins, J. M. 2002, *ApJ*, **575**, 493
- Jenkins, J. M., Chandrasekaran, H., McCauliff, S. D., et al. 2010, *Proc. SPIE*, **7740**, 77400D
- Jenkins, J. M., Tenenbaum, P., Seader, S., et al. 2020, Kepler Data Processing Handbook: Transiting Planet Search, Kepler Science Document KSCI-19081-003
- Jenkins, J. M., Twicken, J. D., McCauliff, S., et al. 2016, *Proc. SPIE*, **9913**, 99133E
- Johnson, M. C., David, T. J., Petigura, E. A., et al. 2022, *AJ*, **163**, 247
- Kanodia, S., & Wright, J. 2018, *RNAAS*, **2**, 4
- Kempton, E.-M.-R., Bean, J. L., Louie, D. R., et al. 2018, *PASP*, **130**, 114401
- Klein, B., Donati, J.-F., Moutou, C., et al. 2021, *MNRAS*, **502**, 188
- Klein, B., Zicher, N., Kavanagh, R. D., et al. 2022, *MNRAS*, **512**, 5067
- Kossakowski, D., Kürster, M., Henning, T., et al. 2022, *A&A*, **666**, A143
- Kostov, V. B., Mullally, S. E., Quintana, E. V., et al. 2019, *AJ*, **157**, 124
- Kovacs, G., Zucker, S., & Mazeh, T. 2002, *A&A*, **391**, 369
- Kreidberg, L., Bean, J. L., Desert, J.-M., et al. 2014, *Natur*, **505**, 69
- Lafreniere, D., Marois, C., Doyon, R., Nadeau, D., & Artigau, E. 2007, *ApJ*, **660**, 770
- Lester, K., Matson, R., Howell, S. B., et al. 2021, *AJ*, **162**, 75
- Li, J., Tenenbaum, P., Twicken, J. D., et al. 2019, *PASP*, **131**, 024506
- Lin, D. N. C., Bodenheimer, P., & Richardson, D. C. 1996, *Natur*, **380**, 606
- Lissauer, J. J. 2007, *ApJ*, **660**, L149
- Lissauer, J. J., Fabrycky, D. C., Ford, E. B., et al. 2011, *Natur*, **470**, 53
- Lissauer, J. J., Marcy, G. W., Rowe, J. F., et al. 2012, *ApJ*, **750**, 112
- Lomb, N. R. 1976, *Ap&SS*, **39**, 447
- Maggio, A., Locci, D., Pillitteri, I., et al. 2022, *ApJ*, **925**, 172
- Mamajek, E. E., & Hillenbrand, L. A. 2008, *ApJ*, **687**, 1264
- Mann, A. W., Johnson, M. C., Vanderburg, A., et al. 2020, *AJ*, **160**, 179
- Marchwinski, R. C., Mahadevan, S., Robertson, P., Ramsey, L., & Harder, J. 2015, *ApJ*, **798**, 63
- Marcy, G. W., Isaacson, H., Howard, A. W., et al. 2014, *ApJS*, **210**, 20
- Marois, C., Lafreniere, D., Doyon, R., Macintosh, B., & Nadeau, D. 2006, *ApJ*, **641**, 556
- Martoli, E., Hébrard, G., Moutou, C., et al. 2020, *A&A*, **641**, L1
- Matson, R. A., Howell, S. B., Horch, E. P., & Everett, M. E. 2018, *AJ*, **156**, 109.02
- Mawet, D., Milli, J., Wahhaj, Z., et al. 2014, *ApJ*, **792**, 97
- Maxted, P. F. L., Anderson, D. R., Collier Cameron, A., et al. 2011, *PASP*, **123**, 547
- May, E. M., & Stevenson, K. B. 2020, *AJ*, **160**, 140
- McCully, C., Volgenau, N. H., Harbeck, D.-R., et al. 2018, *Proc. SPIE*, **10707**, 107070K
- Mermilliod, J. C. 2006, yCat, II/122B
- Meunier, N., & Lagrange, A.-M. 2013, *A&A*, **551**, 17
- Mills, S. M., & Mazeh, T. 2017, *ApJL*, **839**, L8
- Morales, J., Mustill, L., et al. 2019, *Sci*, **365**, 1441
- Mulders, G. D., Pascucci, I., & Apai, D. 2015, *ApJ*, **798**, 112
- Mulders, G. D., Pascucci, I., Apai, D., & Ciesla, F. J. 2018, *AJ*, **156**, 24
- Nava, C., Lopez-Morales, M., Haywood, R. D., & Giles, H. A. C. 2020, *AJ*, **159**, 23
- Newton, E. R., Mann, A. W., Tofflemire, B. M., et al. 2019, *ApJL*, **880**, L17
- Nowak, G., Luque, R., Parviainen, H., et al. 2020, *A&A*, **642**, A173
- Osborn, A., Armstrong, D. J., Cale, B., et al. 2021, *MNRAS*, **507**, 2782
- Palle, E., Oshagh, M., Casasayas-Barris, N., et al. 2020, *A&A*, **643**, A25
- Pascucci, I., Mulders, G. D., & Lopez, E. 2019, *ApJL*, **883**, L15
- Petigura, E. A., Howard, A. W., & Marcy, G. W. 2013, *PNAS*, **110**, 19273
- Plavchan, P., Barclay, T., Gagne, J., et al. 2020, *Natur*, **583**, E31
- Plavchan, P., & Bilinski, C. 2013, *ApJ*, **769**, 86
- Plavchan, P., Latham, D., Gaudi, S., et al. 2015, arXiv:1503.01770
- Plavchan, P. P., Anglada-Escude, G., White, R., et al. 2013, *Proc. SPIE*, **8864**, 88641J
- Pollacco, D. L., Skillen, I., Cameron, A. C., et al. 2006, *PASP*, **118**, 1407
- Rasio, F. A., Tout, C. A., Lubow, S. H., & Livio, M. 1996, *ApJ*, **470**, 1187
- Reefe, M., Luque, R., Gaidos, E., et al. 2021, *AJ*, **85**, 269
- Rein, H., & Liu, S. F. 2012, *A&A*, **537**, A128
- Rein, H., & Spiegel, D. S. 2015, *MNRAS*, **446**, 1424
- Reiners, A., Bean, J. L., Huber, K. F., et al. 2010, *ApJ*, **710**, 432

- Ricker, G. R., Winn, J. N., Vanderspek, R., et al. 2015, *JATIS*, **1**, 014003
- Robertson, P., Mahadevan, S., Endl, M., & Roy, A. 2014, *Sci*, **345**, 440
- Robertson, P., Roy, A., & Mahadevan, S. 2015, *ApJL*, **805**, L22
- Martinez, R. R., Gaudi, B. S., Rodriguez, J. E., et al. 2020, *AJ*, **160**, 111
- Rogers, L. A. 2015, *ApJ*, **801**, 41
- Rogers, L. A., & Seager, S. 2010, *ApJ*, **712**, 974
- Rowe, J. F., Bryson, S. T., Marcy, G. W., et al. 2014, *ApJ*, **784**, 45
- Scargle, J. D. 1982, *ApJ*, **263**, 835
- Scholz, R.-D., Meusinger, H., & Jahrei, H. 2005, *A&A*, **442**, 211
- Seager, S., Kuchner, M., Hier-Majumder, C. A., & Militzer, B. 2007, *ApJ*, **669**, 1279
- Sha, L., Huang, C. X., Shporer, A., et al. 2021, *AJ*, **161**, 82
- Skrutskie, M. F., Cutri, R. M., Stiening, R., et al. 2006, *AJ*, **131**, 1163
- Smith, J. C., Stumpe, M. C., Van Cleve, J. E., et al. 2012, *PASP*, **124**, 1000
- Stassun, K. G., Collins, K. A., & Gaudi, B. S. 2017, *AJ*, **153**, 136
- Stassun, K. G., Corsaro, E., Pepper, J. A., & Gaudi, B. S. 2018, *AJ*, **155**, 22
- Stassun, K. G., Oelkers, R. J., Paegert, M., et al. 2019, *AJ*, **158**, 138
- Stassun, K. G., & Torres, G. 2016, *AJ*, **152**, 180
- Stassun, K. G., & Torres, G. 2021, *ApJL*, **907**, L33
- Stevenson, K. B., Harrington, J., Fortney, J. J., et al. 2012, *ApJ*, **754**, 136
- Stumpe, M. C., Smith, J. C., Catanzarite, J. H., et al. 2014, *PASP*, **126**, 100
- Stumpe, M. C., Smith, J. C., Van Cleve, J. E., et al. 2012, *PASP*, **124**, 985
- Surez Mascareo, A., Damasso, M., Lodieu, N., et al. 2021, *NatAs*, **6**, 232
- Sun, L., Ioannidis, P., Gu, S., et al. 2019, *A&A*, **624**, A15
- Szab, G. M., Gandolfi, D., Brandeker, A., et al. 2021, *A&A*, **654**, A159
- Tejada Arevalo, R., Tamayo, D., & Cranmer, M. 2022, *ApJ*, **932**, L12
- Teske, J., Wang, S. X., Wolfgang, A., et al. 2021, *ApJS*, **256**, 33
- Tokovinin, A. 2018, *PASP*, **130**, 035002
- Torres, G., Andersen, J., & Gimenez, A. 2010, *A&ARv*, **18**, 67
- Tuomi, M., Jones, H. R. A., Barnes, J. R., Anglada-Escude, G., & Jenkins, J. S. 2014, *MNRAS*, **441**, 1545
- Twicken, J. D., Catanzarite, J. H., Clarke, B. D., et al. 2018, *PASP*, **130**, 064502
- van Leeuwen, F. 2007, *A&A*, **474**, 653
- Vanderburg, A., Plavchan, P., Johnson, J. A., et al. 2016, *MNRAS*, **459**, 3565
- Vanderburg, A., Huang, C. X., Rodriguez, J. E., et al. 2019, *ApJL*, **881**, L19
- Virtanen, P., Gommers, R., Oliphant, T. E., et al. 2020, *NatMe*, **17**, 261
- Vogt, S., Allen, S., Bigelow, B., et al. 1994, *Proc. SPIE*, **2198**, 362
- Walkowicz, L. M., & Basri, G. S. 2013, *MNRAS*, **436**, 1883
- Ward, W. R. 1997, *Icar*, **126**, 261
- Weiss, L. M., & Marcy, G. W. 2014, *ApJL*, **783**, L6
- Weiss, L. M., & Petigura, E. A. 2020, *ApJL*, **893**, L1
- Weiss, L. M., Marcy, G. W., Petigura, E. A., et al. 2018, *AJ*, **155**, 48
- Wheatley, P. J., West, R. G., Goad, M. R., et al. 2018, *MNRAS*, **475**, 4476
- Wise, A., Dodson-Robinson, S., Bevenour, K., & Provini, A. 2018, *AJ*, **156**, 180
- Wittrock, J. M., Dreizler, S., Reefe, M. A., et al. 2022, *AJ*, **164**, 27
- Wolfgang, A., Rogers, L. A., & Ford, E. B. 2016, *ApJ*, **825**, 19
- Wright, E. L., Eisenhardt, P. R. M., Mainzer, A. K., et al. 2010, *AJ*, **140**, 1868
- Zechmeister, M., & Kurster, M. 2009, *A&A*, **496**, 577
- Zechmeister, M., Reiners, A., Amado, P. J., et al. 2020, *SERVAL: SpEctrum Radial Velocity AnaLyser, Astrophysics Source Code Library*, ascl:2006.011
- Zeng, L., Jacobsen, S. B., Sasselov, D. D., et al. 2019, *PNAS*, **116**, 9723
- Zhang, M., Knutson, H. A., Wang, L., Dai, F., & Barragan, O. 2022, *AJ*, **163**, 67
- Zhu, Z., Hartman, L., Neson, R., & Gammie, C. F. 2012, *ApJ*, **746**, 110
- Zicher, N., Barragan, O., Klein, B., et al. 2022, *MNRAS*, **512**, 3060
- Ziegler, C., Tokovinin, A., Briceno, C., et al. 2020, *AJ*, **159**, 19
- Zink, J. K., Hardegree-Ullman, K. K., Christiansen, J. L., et al. 2020, *AJ*, **159**, 154

